Superconducting proximity effect in graphene

Sopic, Sandra

UNIVERSITÉ DE GENÈVE
Département de Physique
de la Matière Quantique

FACULTÉ DES SCIENCES
Professeur A. Morpurgo

Superconducting proximity effect in graphene

THÈSE

présentée à la Faculté des Sciences de l'Université de Genève
pour obtenir le grade de docteur ès Sciences, mention Physique

par

Sandra Šopić
de
Belgrade (Serbie)

Thèse n° 4827

GENÈVE
Atelier d'impression ReproMail
2015

UNIVERSITÉ
DE GENÈVE

FACULTÉ DES SCIENCES

Doctorat ès sciences
Mention physique

Thèse de *Madame Sandra ŠOPIC*

intitulée :

" Superconducting Proximity Effect in Graphene"

La Faculté des sciences, sur le préavis de Monsieur A. MORPURGO, professeur ordinaire et directeur de thèse (Département de physique de la matière quantique), Monsieur Ch. RENNER, professeur ordinaire (Département de physique de la matière quantique), et Monsieur S. KUBATKIN, (Chalmers University of Technology, Departement of Microtechnology and Nanoscience, Gothenburg, Sweden), autorise l'impression de la présente thèse, sans exprimer d'opinion sur les propositions qui y sont énoncées.

Genève, le 25 septembre 2015

Thèse - 4827 -

Le Doyen

N.B. - La thèse doit porter la déclaration précédente et remplir les conditions énumérées dans les "Informations relatives aux thèses de doctorat à l'Université de Genève".

To my family

Résumé

Durant la décennie écoulée, la recherche dans le domaine de la matière condensée a été marquée par la découverte du premier matériau bidimensionnel – le graphène. L'importance scientifique du graphène a été aussitôt reconnue, comme l'atteste l'attribution du prix Nobel à Konstantin Novoselov et Andre Geim, les scientifiques qui ont su les premiers extraire le graphène d'un morceau de graphite. Les propriétés uniques du graphène révèlent des phénomènes inhabituels en physique quantique, stimulant ainsi la recherche pour découvrir d'autres matériaux bidimensionnels tels que le nitrure de bore hexagonal (hBN), les dichalcogenides de métaux de transition, ou encore les phosphorines parmi d'autres. Il y a deux ans, des hétérostructures artificielles ont été assemblées comme des briques de Lego à partir de monocouches de différents cristaux, liées par la force de Van der Waals, ce qui ouvre la voie pour fabriquer de nouveaux matériaux avec des propriétés sur mesure. Ce domaine est en plein développement, comme le montrent les progrès considérables accomplis en un temps très court à partir du simple graphène, et restera grâce à l'apport des autres matériaux bidimensionnels l'un des principaux sujets de recherche en matière condensée dans les années à venir.

Bien que le graphène possède nombre de propriétés remarquables, la supraconductivité n'en fait pas spontanément partie. Il y a cependant un immense intérêt fondamental et pratique à induire la supraconductivité dans le graphène. L'une des premières expériences effectuée sur des dispositifs basés sur le graphène a déjà montré que ce matériau, s'il est mis en contact étroit avec deux électrodes supraconductrices, permet à un supercourant de s'écouler, porté aussi bien par des électrons que par des trous. Des travaux théoriques indiquent qu'en plus de ce supercourant induit, d'autres effets de proximité devraient se produire dans le graphène. A cela s'ajoute que le transport électrique peut être contrôlé par une tension de grille dans le graphène, ce qui en fait une plateforme idéale pour étudier des régimes de conduction et des phénomènes encore inexplorés dans le contexte des effets de proximité en relation avec la supraconductivité.

Dans la première partie de cette thèse, j'ai étudié les effets de proxim-

ité dans le graphène par des mesures de transport dans un interféromètre d'Andreev. Je me suis concentrée sur la réentrance des oscillations de conductance d'Andreev, en utilisant la possibilité de modifier dans une large gamme la densité de porteurs au moyen d'une tension de grille pour faire varier la conductance des dispositifs dans l'état normal, ainsi que l'énergie de Thouless. J'ai ainsi pu tester une loi d'échelle qui donne l'amplitude des oscillations en fonction de l'énergie, loi que la théorie prédit en l'absence d'interactions. Plus précisément, le but est de savoir si une propriété définie comme le produit de l'amplitude des oscillations par la résistance dans l'état normal est une fonction universelle de la tension normalisée par l'énergie de Thouless, ceci indépendamment de la tension de grille. Il s'avère que cette loi est très bien satisfaite lorsque la tension de grille est suffisamment élevée. En revanche, à mesure que le niveau de Fermi est abaissé en direction du point de neutralité, la loi d'échelle est de moins en moins bien satisfaite, et finalement plus du tout adéquate. L'interprétation qui est donnée de cette observation est que la longueur de cohérence de phase des électrons est diminuée près du point de neutralité, ce qui empêche la propagation des corrélations supraconductrices loin de l'interface supraconducteur/graphène. Ainsi, l'effet de proximité est limité par les fluctuations thermiques lorsque la tension de grille est grande, mais c'est la décohérence quantique qui le contrôle près du point de neutralité.

Dans la second partie, je présente une étude spectroscopique de la manière dont les états électroniques contribuent différemment en fonction de leur énergie au courant Josephson dans une jonction SNS (supraconducteur/métal normal/supraconducteur). Les états qui sont responsables du transport sans dissipation sont essentiellement confinés aux énergies plus petites que le gap supraconducteur Δ et sont connus sous le nom d'états liés d'Andreev. Cependant, l'existence de résonances qui conduisent un supercourant à des énergies $E > \Delta$ a été prédite déjà dans le premier article théorique d'Andreev. Contrairement aux états liés, les résonances d'Andreev ainsi que leur contribution au supercourant restent inobservés. Nos expériences reposent sur des jonctions Josephson à plusieurs contacts, dans lesquelles la contribution des différents états au courant supraconducteur est déterminée en changeant la distribution des électrons dans la jonction. Par le passé, les dispositifs étaient fabriqués avec des métaux conventionnels, ce qui limitait l'étude du supercourant à des énergies $E \ll \Delta$. L'usage du graphène comme conducteur permet d'étendre cette étude au régime $E > \Delta$. Aux énergies plus faibles que le gap, la modification de la distribution électronique diminue progressivement la contribution des états liés. Quand celle-ci est complètement supprimée, mes mesures on montré qu'un supercourant significatif continue de s'écouler à travers la jonction. Ce courant est dû aux résonances dont les énergies se trouvent dans le continuum. Mes résultats démontrent donc l'importance des

résonances d'Andreev dans le transport supraconducteur.

Pour conclure, mes résultats confirment pleinement que l'usage du graphène au lieu de métaux plus conventionnels dominés par la diffusion ouvre de nouvelles perspectives dans l'étude des effets de proximité liés à la supraconductivité. Certains de ces effets, comme l'influence de la décohérence sur l'effet de proximité et la contribution des résonances d'Andreev au supercourant de Josephson, étaient restés inexplorés jusqu'ici.

Contents

Chapter 1

Introduction

1.1 Superconducting proximity effect

The term superconducting proximity effect denotes physical phenomena occurring in a systems which consist of a superconducting material electrically connected to a non-superconducting one. In a sense, a normal conductor (N) attached through a highly transparent interface to a superconductor (S) acquires several properties typical of the superconducting state. It exhibits magnetic screening and its density of states at the Fermi energy is suppressed. Moreover, when a normal conductor is placed between two superconducting electrodes, a current can flow without any applied bias. At the same time, the presence of a normal conductor also "acts back" on a superconductor and affects its properties. For instance, it leads to the suppression of the critical temperature and the critical current. Microscopically, twenty years ago, it was understood that proximity effect is essentially an interplay between phase coherent propagation inside a normal conductor and a process that enables transport across a N/S interface known as Andreev reflection [1]. Phase coherent transport and Andreev reflection will be discussed in detail in theory chapter.

The role of phase coherence in proximity effect was initially unknown. The appreciation of the relevance of phase coherence came after the development of lithographic processes that enabled experimental realization of mesoscopic structures and of cryogenic systems allowing low-temperature transport measurements. With these technological advances phenomena related to phase coherence such as weak (anti) localization, universal conductance fluctuations and Aharonov-Bohm effect became experimentally visible. This provided conceptual understanding of phase coherent transport in mesoscopic structures. Characteristics length and energy scales associated with the phase

coherent transport in a normal conductor, such as the microscopic phase coherence length, the Thouless length and the corresponding energy (Thouless energy) [2], turned out to be also relevant for understanding the proximity effect.

In the field of proximity effect, theoretical and experimental investigations revealed interesting phenomena occurring in systems with diffusive normal conductor connected to one or more superconducting electrodes through highly transparent interfaces. We mention only the ones that are subjects of the research carried out in this thesis, the so-called reentrance effect where the resistance of a N/S junction exhibits a counterintuitive behavior as a function of temperature or applied bias, and Andreev interferometry, consisting in conductance oscillations induced by the phase of the superconducting order parameter, occurring in devices known as Andreev interferometers. Beside these phenomena, a supercurrent can be induced inside a normal region of S/N/S junctions due to the occurrence of Andreev reflection on both interfaces. This phenomena was first theoretically described by Kulik [3] who related the appearance of supercurrent to the formation of supercurrent-carrying states in a normal region, referred to as Andreev bound states at energies below the superconducting gap and Andreev resonances above the gap. Reentrance effect, Andreev interferometry and transport through a S/N/S junctions will be discussed in the next chapter.

1.2 Graphene

Since its discovery eleven years ago, graphene has resulted in considerable scientific breakthroughs, especially in the field of condensed matter physics [4]. One of its greatest impact is that is has led to the discovery of many other two-dimensional materials. Molybdenum disulfide MoS_2 [5, 6], a member of a broader family of materials called transition metal dichalcogenides, and phosphorene [7], known also as black phosphorus, are among those which are particularly interesting for electronic devices. In recent years, stacking different two-dimensional materials became possible which gives the opportunity to engineer new materials with desired properties through the creation of so-called Van der Waals heterostructures [8]. With increasing number of available 2D crystals the choice of possible Van der Waals heterostructures is practically unlimited. The use of graphene as a building block for these heterostructures is just one of the examples demonstrating that even "long" after its discovery, graphene is still widely present in the fundamental research.

The reason why graphene is an attractive material to study in condensed matter physics comes from its unusual electronic properties. Contrary to conventional materials where electron motion is described by Schrödinger equation, low-energy electrons in graphene are described by Dirac equation

[9, 10] (relativistic version of Schrödinger equation). In the low-energy limit, the energy dispersion in graphene is linear and electrons are considered to be Dirac fermions as they are massless [9] and move with a constant Fermi velocity ($v_F \approx c/300$ m/s^2). Since the crystal lattice of graphene consists of two inequivalent sublattices, the electron wave function has two components, i.e. it has a spinor character commonly referred to as pseudospin (the prefix "pseudo" indicates that the two components of the wave function do not arise from the true spin of the electrons). The direction of momentum of an electron is linked to the pseudospin, which make electrons in graphene chiral. These interesting properties lead to unusual manifestations of mesoscopic phenomena such as an anomalous quantum Hall effect [11, 12] and a minimum conductivity at the charge neutrality point [4], as we will discuss in detail later. In our experiments, where we use graphene as a diffusive normal conductor, the Dirac nature of electrons is not particularly relevant, as it does not majorly affect the superconducting proximity effect. However, we do exploit Dirac properties of graphene in order to characterize our devices. Electronic properties of graphene will be further discussed in theory chapter.

From the proximity effect point of view, there are several aspects of graphene that are interesting for our purposes. A common problem with conventional two-dimensional electron gases is the realization of "clean" interfaces with a superconductor. This critical, but very essential, device-fabrication issue can be easily avoided by using graphene which makes a good electrical contact to a superconducting materials even when exposed to air. Other important advantages are that graphene enables bipolar transport, i.e. both electrons and holes in graphene can carry current, and that the charge carrier density can be readily tuned over a large range by means of electrostatical gating. Moreover, graphene crystal has very low density of structural defects due to the strong covalent bonds between carbon atoms, which contribute to the high mobility of charge carriers. For instance, the charge carrier mobility in graphene exfoliated on SiO_2 substrates is typically $\mu \sim 10^4$ cm^2/Vs at 250 mK [9]. Due to high quality of this material, the phase coherence length of electrons in graphene on SiO_2 at 250 mK is typically in the range $2 - 5$ μm [13] making it a good choice for nano-electronic devices which are aimed for studying phase coherent transport and superconducting proximity effect.

1.3 Motivation

Despite the fact that graphene has many remarkable properties –superconductivity is not one of them. However, there is a great fundamental and practical interest in inducing superconductivity in graphene. The first experiment demonstrating supercurrent in graphene-based devices also showed that supercurrent can be carried by either electrons in the conduction band or holes

in the valence band, depending on the gate voltage [14], as shown in Fig 1.1.

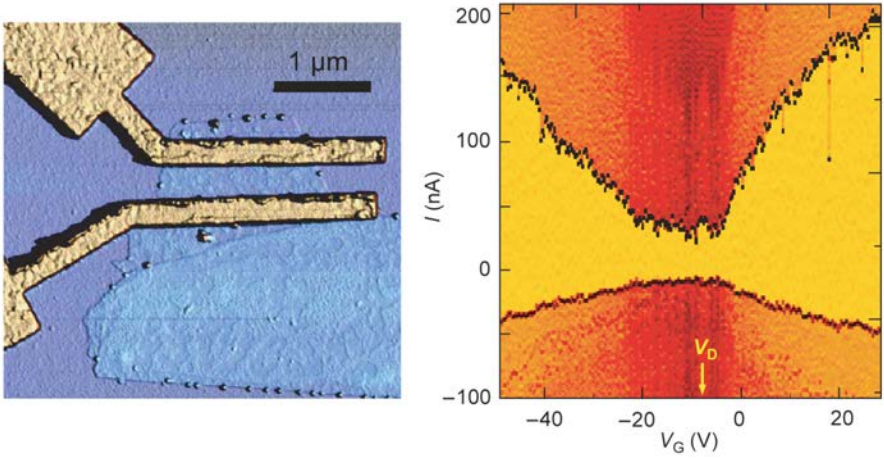

Figure 1.1: (Left panel) Atomic force microscope image of a single-layer graphene device between two superconducting electrodes. (Right panel) Bipolar supercurrent and finite supercurrent at the Dirac point are illustrated with a color plot of $dV/dI(V_G, I)$. Yellow represents zero (the supercurrent region); dV/dI increases as the color evolves to orange to dark red. The arrow at V_D indicates the position of the so-called Dirac point. Figure adapted from [14].

Apart from induced supercurrent in graphene contacted by two closely spaced superconducting electrodes, theoretical investigations indicate that proximity effect phenomena such as reentrance effect and Andreev interferometry –the ones we introduced in the first section– should occur in graphene-based systems as well [15]. Together with these indications our work was also motivated by the question if the possibility to gate-tune the normal transport in graphene can lead to new findings in the field of superconducting proximity effect.

Part of this thesis presents a study of transport in S/N/S junctions with graphene as a diffusive normal conductor to probe the nature of the states responsible for the flow of supercurrent. Our study relies on a method originally suggested by van Wees et. al [16], who theoretically explored how the modulation of occupation of Andreev bound states affects supercurrent in the ballistic regime (the same was done later for a diffusive SNS junction by Volkov [17]). Experimentally, the control of supercurrent through the occupation of supercurrent-carrying states was first implemented and demonstrated by Morpurgo et al. [18], where the control of supercurrent was achieved using a diffusive S/N/S junction connected through its central part to the so-called "control line", i.e. a normal wire whose ends were attached to additional

reservoirs. This control line served to heat the electrons in the S/N/S junction by passing current which effectively increased electron temperature and, consequently, led to the suppression of the critical current of the junction. A similar experiment was performed later by Baselmans et al. [19], who found a way to revert supercurrent by generating a specific non-equilibrium distribution in S/N/S junctions through the application of a control voltage bias (as previously demonstrated in experiments by Pothier et al. [20]). Figure 1.2 shows layout of the device used in this experiment and the dependence of the supercurrent on the control voltage exhibiting suppression and reversal of direction.

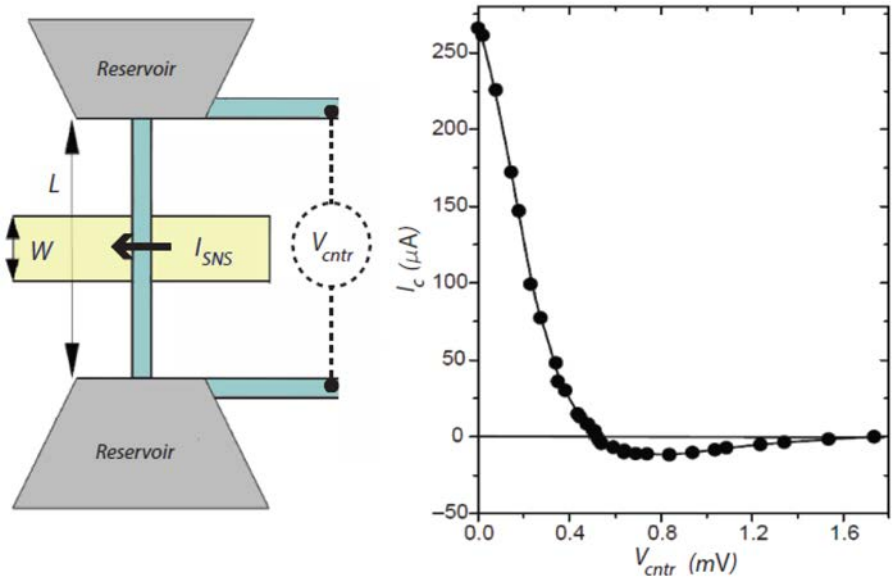

Figure 1.2: (Left panel) Schematics of the multi-terminal S/N/S junctions used in the work of Baselmans et al. [19]. (Right panel) Critical current of the S/N/S junction as a function of the control voltage exhibiting reversal of a sign. Figures adapted from [19].

1.4 Outline

In the previous sections we have introduced the general context and main motivation for our study of proximity effect using a new platform –graphene. Here we discuss in more details the content of the individual chapters of thesis.

In chapter 2, we discuss the fundamental concepts which are essential for understanding of electron transport in graphene/superconductor devices. Section §2.1 discusses the electronic properties of graphene mostly focusing on the unusual electron transport in the low-energy regime. Important concepts related to phase coherent transport, namely, ensemble-average and sample-specific quantum interference effects, are explained in section §2.2. After briefly introducing superconductivity (section §2.3), we describe in more details the process that enables electron transport across N/S interfaces –Andreev reflection (section §2.4). Subsequently, we describe the manifestations of proximity effect in dissipative transport relevant for this thesis in section §2.5. This chapter finishes with a discussion of superconducting and dissipative transport in S/N/S junctions.

Chapter 3 focuses on the fabrication of nano-electronic devices that were used to carry out the transport measurements reported in this thesis. In section §3.1, we describe the experimental realization of our samples and explain in more details some of the fabrication steps such as electron beam lithography and metal deposition. In the following section we discuss graphene deposition and characterization. Graphene flakes in our devices are produced through mechanical exfoliation and their thickness is defined with the help of an optical microscope, which provides a simple and non-invasive method based on optical contrast. Since our devices are used to study superconducting proximity effect, we also discuss in detail the quality of the superconducting film (section §3.4) and of the graphene/superconductor interface (section §3.5), which are essential for our work.

Chapter 4 describes an experiment that we performed to investigate how the tuning of microscopic decoherence affects superconducting proximity effect. To this end, we carried out transport measurements through graphene Andreev interferometers exhibiting the reentrance effect. Our results show that at high gate voltage the energy dependence of the Andreev conductance oscillations exhibits a scaling behavior in agreement with theoretical expectations. This agreement breaks down close to the charge neutrality point as electron dephasing limits the propagation of superconducting correlations away from the superconductor/graphene interface. Our work shows that graphene provides a useful experimental platform to address the interplay between electron decoherence and superconductivity, and to observe unexplored regimes in proximity effect.

In chapter 5, we study how electronic states at different energy contribute to the supercurrent in superconductor-graphene-superconductor Josephson junctions. Our experiment relies on supercurrent spectroscopy method used in the work of Baselmans et al. [19]. Our analysis shows that the evolution of the critical current of our junction is consistent with a "two-step" distribution, which implies that our results provide spectroscopic information about the

supercurrent carrying density of states. We find that when the contribution to the supercurrent of Andreev bound states is entirely suppressed there is a finite critical current still present in the junction. This remaining supercurrent is carried by Andreev resonances at energies above the gap, whose role in S/N/S Josephson junctions was predicted long ago by Kulik [3] but it has not been confirmed until now.

1.5 Bibliography

[1] A. F. Andreev. The thermal conductivity of the intermediate state in superconductors. *JETP*, 46:1823, 1964.

[2] D. J. Thouless. Maximum metallic resistance in thin wires. *Phys. Rev. Lett.*, 39:1167–1169, 1977.

[3] I. O. Kulik. Macroscopic quantization and the proximity effect in s-n-s junctions. *JETP*, 30:1745, 1970.

[4] A. K. Geim and K. S. Novoselov. The rise of graphene. *Nat Mater*, 6(3):183–191, 2007.

[5] B. Radisavljevic, A. Radenovic, J. Brivio, V. Giacometti and A. Kis. Single-layer MoS2 transistors. *Nat Nano*, 6(3):147–150, 2011.

[6] Q. H. Wang, K. Kalantar-Zadeh, A. Kis, J. N. Coleman and M. S. Strano. Electronics and optoelectronics of two-dimensional transition metal dichalcogenides. *Nat Nano*, 7:699–712, 2012.

[7] L. Li, Y. Yu, G. J. Ye, Q. Ge, X. Ou, H. Wu, D. Feng, X. H. Chen and Y. Zhang. Black phosphorus field-effect transistors. *Nat Nano*, 9:372–377, 2014.

[8] A. K. Geim and I. V. Grigorieva. Van der Waals heterostructures. *Nature*, 499:419–425, 2013.

[9] K. S. Novoselov, A. K. Geim, S. V. Morozov, D. Jiang, Y. Zhang, S. V. Dubonos, I. V. Grigorieva and A. A. Firsov. Electric field effect in atomically thin carbon films. *Science*, 306(5696):666–669, 2004.

[10] A. H. Castro Neto, F. Guinea, N. M. R. Peres, K. S. Novoselov and A. K. Geim. The electronic properties of graphene. *Rev. Mod. Phys.*, 81:109–162, 2009.

[11] Y. Zhang, Y.-W. Tan, H. L. Stormer and P. Kim. Experimental observation of the quantum Hall effect and Berry's phase in graphene. *Nature*, 438(7065):201–204, 2005.

[12] K. S. Novoselov, E. McCann, S. V. Morozov, V. I. Fal'ko, M. I. Katsnelson, U. Zeitler, D. Jiang, F. Schedin, and A. K. Geim. Unconventional quantum Hall effect and Berry's phase of 2π in bilayer graphene. *Nat Phys*, 2(3):177–180, 2006.

[13] F. Miao et al. Phase-coherent transport in graphene quantum billiards. *Science*,317:1530–1533, 2007.

[14] H. B. Heersche, P. Jarillo-Herrero, J. B. Oostinga, L. M. K. Vandersypen and A. F. Morpurgo. Bipolar supercurrent in graphene. *Nature*, 446(7131):56–59, 2007.

[15] A. Ossipov et al. Reentrance effect in a graphene n-p-n junction coupled to a superconductor. *Phys. Rev. B*, 75:241401, 2007.

[16] B. J. van Wees, K.-M. H. Lenssen, and C. J. P. M. Harmans. Transmission formalism for supercurrent flow in multiprobe superconductor-semiconductor-superconductor devices. *Phys. Rev. B*, 44:470–473, Jul 1991.

[17] A. F. Volkov. New phenomena in Josephson *SINIS* junctions. *Phys. Rev. Lett.*, 74:4730–4733, 1995.

[18] A. F. Morpurgo, T. M. Klapwijk, and B. J. van Wees. Hot electron tunable supercurrent. *Appl. Phys. Lett.*, 72(8):966–968, 1998.

[19] J. J. A. Baselmans, A. F. Morpurgo, B. J. van Wees, and T. M. Klapwijk. Reversing the direction of the supercurrent in a controllable Josephson junction. *Nature*, 397(6714):43–45, January 1999.

[20] H. Pothier, S. Guéron, Norman O. Birge, D. Esteve, and M. H. Devoret. Energy distribution function of quasiparticles in mesoscopic wires. *Phys. Rev. Lett.*, 79:3490–3493, Nov 1997.

Chapter 2

Theoretical concepts

The aim of this chapter is to introduce the theoretical concepts needed to understand electron transport in graphene-superconductor devices. The first section §2.1 shows a derivation of the electron band structure in a single-layer graphene using the tight-binding model. It also discusses how these results can be approximated in the low-energy limit [1, 2], which is important since transport in graphene is usually probed in a small range around zero energy. Moreover, it focuses on the relevant aspects of low-energy transport when an electric field or a magnetic field are applied. Phase coherent transport and quantum interference phenomena are explained in §2.2. In §2.3 we present important concepts related to superconductivity and in the following section (§2.4) we give the description of Andreev reflection (the process mediating transport at normal conductor/superconductor interfaces), so that all the necessary elements to understand the basic aspects of the superconducting proximity effect are provided. In §2.5 two manifestations of the superconducting proximity effect in the dissipative transport properties, relevant for this work, are explained in detail. This chapter ends with a section discussing the supercurrent flowing through a normal conductor placed between two superconducting electrodes.

2.1 Electronic properties of graphene

Single layer graphene consists of carbon atoms forming a two-dimensional honeycomb structure. In total, there are six electrons in a carbon atom. Two of them occupy the $1s^2$ orbital and are strongly attached to the nucleus. The remaining four valence electrons occupy 2s and 2p orbitals. They are responsible for the interaction between the neighboring atoms in graphene.

In graphene, the $2p_x$ and $2p_y$ orbitals hybridize with the 2s orbital re-

sulting in three sp^2 orbitals that lie in the graphene plane, at $120°$ angles. The sp^2 orbitals of the neighboring atoms overlap and build strong covalent bonds, known as σ bonds which give graphene its extraordinary mechanical properties. The hybridization process leaves one $2p_z$ orbital per every carbon atom, oriented perpendicular to the graphene layer. Hybridization of the $2p_z$ orbitals of neighboring atoms give rise to the so-called π bands. Electrons in these π bands are weakly attached to the carbon atoms and are effectively free to move around (i.e., they are delocalized). These are the conduction electrons that contribute to transport in graphene. Their properties are well described by a simple tight-binding model.

2.1.1 Tight binding model and band structure

The graphene crystal lattice consists of two inequivalent triangular sublattices, denoted as A-sublattice and B-sublattice, shown in Fig. 2.1. Two atoms, one atom from the A-sublattice and the other from the B-sublattice, form the basis of the graphene Bravais lattice. The primitive lattice vectors of the Bravais lattice are shown in Fig. 2.1a and are defined by

$$\mathbf{a}_1 = \frac{a}{2}(1, \sqrt{3}) \qquad \text{and} \qquad \mathbf{a}_2 = \frac{a}{2}(1, -\sqrt{3}), \tag{2.1}$$

where $a = 2.46$ Å. The interatomic distance (i.e., the distance between a A and a B atom in the same unit cell) is $a/\sqrt{3} = 1.42$ Å. The A and B sites are independent as it can be seen from the fact that the lattice vector $\mathbf{R} = n\mathbf{a}_1 + m\mathbf{a}_2$ (n and m are integers), cannot connect their atomic positions. In real space, every carbon atom in graphene is bonded to three atoms from the opposite sublattice, which are its nearest neighbors, separated by vectors

$$\boldsymbol{\delta}_1 = (0, \frac{a}{\sqrt{3}}), \qquad \boldsymbol{\delta}_2 = (\frac{a}{2}, -\frac{a}{2\sqrt{3}}) \quad \text{and} \quad \boldsymbol{\delta}_3 = (-\frac{a}{2}, -\frac{a}{2\sqrt{3}}). \tag{2.2}$$

The reciprocal vectors satisfy the conditions $\mathbf{a}_i\mathbf{b}_j = 2\pi\boldsymbol{\delta}_{i,j}$ and are equal to

$$\mathbf{b}_1 = \frac{2\pi}{a}(1, \sqrt{3}) \quad \text{and} \quad \mathbf{b}_2 = \frac{2\pi}{a}(1, -\sqrt{3}). \tag{2.3}$$

The resulting reciprocal lattice is also hexagonal. Figure 2.1b shows the first Brillouin zone and the high symmetry points in momentum space

$$\mathbf{\Gamma}(0,0), \qquad \mathbf{M}(\frac{2\pi}{3a}, 0), \qquad \mathbf{K}_+(\frac{2\pi}{3a}, \frac{2\pi}{3\sqrt{3}a}) \quad \text{and} \quad \mathbf{K}_-(\frac{2\pi}{3a}, -\frac{2\pi}{3\sqrt{3}a}). \tag{2.4}$$

The corners of the first Brillouin zone can be subdivided into two groups labeled as $\mathbf{K}_+$ and $\mathbf{K}_-$. Within each group there are three equivalent corners

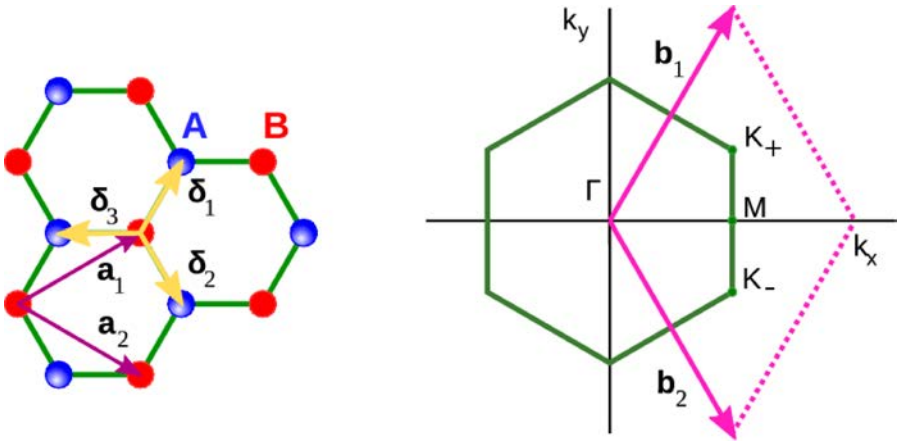

Figure 2.1: (Left panel) The honeycomb lattice of graphene with two carbon atoms per unit cell, one belonging to the A (colored blue) and the other to the B sublattice (colored red). The primitive vectors of the Bravais lattice are $\mathbf{a}_1$ and $\mathbf{a}_2$. The nearest neighbor vectors from the B site to the A sites are $\boldsymbol{\delta}_l$ ($l = 1, 2, 3$). (Right panel) The first Brillouin zone also has hexagonal shape with the reciprocal lattice vectors $\mathbf{b}_1$ and $\mathbf{b}_2$. $\mathbf{\Gamma}, \mathbf{M}$, $\mathbf{K}_+$ and $\mathbf{K}_-$ represent the high symmetry points in momentum space.

that are connected by vectors of the reciprocal lattice. These points are important in the description of the low-energy transport properties of graphene and are commonly referred to as Dirac points.

The dispersion relation of the π and π^* bands in graphene are found by solving the Schrödinger equation

$$\hat{H}|\Psi\rangle = E_{\mathbf{k}}|\Psi\rangle, \tag{2.5}$$

where $\hat{H}$ is the Hamiltonian obtained from the tight-binding model, $|\Psi\rangle$ an eigenstate and $E_{\mathbf{k}}$ the corresponding eigenenergy. Because of the lattice periodicity the wave function $|\Psi\rangle$ satisfies the Bloch condition

$$\Psi(\mathbf{r} + \mathbf{R}) = e^{i\mathbf{k}\mathbf{R}}\Psi(\mathbf{r}), \tag{2.6}$$

with a wavevector $\mathbf{k}$. Since the unit cell of the graphene crystal lattice accommodates two atoms (two $2p_z$ orbital per unit cell), a generic Bloch wave function can be written as

$$\Psi(\mathbf{k}, \mathbf{r}) = \frac{1}{\sqrt{N}}\Big[c_A \sum_{\mathbf{R}_A}^{N} e^{i\mathbf{k}\mathbf{R}_A}\varphi_A(\mathbf{r} - \mathbf{R}_A) + c_B \sum_{\mathbf{R}_B}^{N} e^{i\mathbf{k}\mathbf{R}_B}\varphi_B(\mathbf{r} - \mathbf{R}_B)\Big], \tag{2.7}$$

with N being the total number of unit cells in the crystal, c_A and c_B the amplitudes of Ψ on A and B sublattices, $\mathbf{R}_A$ and $\mathbf{R}_B$ are the lattice vectors

on A and B sublattices, φ_A and φ_B are the wave functions of the p_z orbitals centered on the A and B sublattices, respectively.

From the tight-binding system the eigenstates and corresponding eigenenergies on both sublattices can be obtained by projecting on the states $|\varphi_A\rangle$ and $|\varphi_B\rangle$

$$\langle\varphi_A|\hat{H}|\Psi\rangle = E_{\mathbf{k}}\langle\varphi_A|\Psi\rangle, \tag{2.8}$$

$$\langle\varphi_B|\hat{H}|\Psi\rangle = E_{\mathbf{k}}\langle\varphi_B|\Psi\rangle. \tag{2.9}$$

If only the nearest neighbor hopping is considered, and with the position of the B atoms relative to the A site, $\mathbf{R}_A - \mathbf{R}_{B,l}$ denoted by $\boldsymbol{\delta}_l$, $l = 1, 2, 3$ (1.2), Eqs. (2.8) and (2.9) can be rewritten as

$$\begin{aligned} c_A\langle\varphi_A|\hat{H}|\varphi_A\rangle + c_B\langle\varphi_A|\hat{H}|\varphi_B\rangle(e^{i\mathbf{k}\boldsymbol{\delta}_1} + e^{i\mathbf{k}\boldsymbol{\delta}_2} + e^{i\mathbf{k}\boldsymbol{\delta}_3}) = \\ E_{\mathbf{k}}\Big[c_A\langle\varphi_A|\varphi_A\rangle + c_B\langle\varphi_A|\varphi_B\rangle(e^{i\mathbf{k}\boldsymbol{\delta}_1} + e^{i\mathbf{k}\boldsymbol{\delta}_2} + e^{i\mathbf{k}\boldsymbol{\delta}_3})\Big], \end{aligned} \tag{2.10}$$

$$\begin{aligned} c_A\langle\varphi_B|\hat{H}|\varphi_A\rangle(e^{-i\mathbf{k}\boldsymbol{\delta}_1} + e^{-i\mathbf{k}\boldsymbol{\delta}_2} + e^{-i\mathbf{k}\boldsymbol{\delta}_3}) + c_B\langle\varphi_B|\hat{H}|\varphi_B\rangle = \\ E_{\mathbf{k}}\Big[c_A\langle\varphi_B|\varphi_A\rangle(e^{-i\mathbf{k}\boldsymbol{\delta}_1} + e^{-i\mathbf{k}\boldsymbol{\delta}_2} + e^{-i\mathbf{k}\boldsymbol{\delta}_3}) + c_B\langle\varphi_B|\varphi_B\rangle\Big]. \end{aligned} \tag{2.11}$$

The term $\langle\varphi_A|\hat{H}|\varphi_A\rangle$ can be replaced with the energy of the $2p_z$ orbital, ϵ_{2p}. Since the carbon atom on the A site is chemically the same as the carbon atom on B site the value of $\langle\varphi_B|\hat{H}|\varphi_B\rangle$ is also equal to ϵ_{2p}. In addition, the terms $\langle\varphi_A(\mathbf{R}_A)|\hat{H}|\varphi_B(\boldsymbol{\delta}_l)\rangle$, which describe hopping from an A site to the nearest B sites, have the same value for all neighboring pairs and are set equal to $-t$. Electron hopping from a B atom to a A atoms is also given by $-t$. The overlap between two $2p_z$ orbitals on the same atom is considered to be $\langle\varphi_A|\varphi_A\rangle = 1$, and the same applies for B atomic sites, the orbitals of adjacent atoms are considered as orthogonal $\langle\varphi_A(\mathbf{R}_A)|\varphi_B(\boldsymbol{\delta}_l)\rangle = 0$ for all three neighboring atoms. The equations above then become

$$c_A\epsilon_{2p} - tc_B(e^{i\mathbf{k}\boldsymbol{\delta}_1} + e^{i\mathbf{k}\boldsymbol{\delta}_2} + e^{i\mathbf{k}\boldsymbol{\delta}_3}) = c_A E_{\mathbf{k}}, \tag{2.12}$$

$$-tc_A(e^{-i\mathbf{k}\boldsymbol{\delta}_1} + e^{-i\mathbf{k}\boldsymbol{\delta}_2} + e^{-i\mathbf{k}\boldsymbol{\delta}_3}) + c_B\epsilon_{2p} = c_B E_{\mathbf{k}}. \tag{2.13}$$

Without loss of generality we can set $\epsilon_{2p} = 0$, and we denote with $f(\mathbf{k}) = (e^{i\mathbf{k}\boldsymbol{\delta}_1} + e^{i\mathbf{k}\boldsymbol{\delta}_2} + e^{i\mathbf{k}\boldsymbol{\delta}_3})$ the coupling between A and B sublattices. The eigenenergies are then found by solving the equation

$$\det\begin{pmatrix} -E & -tf(\mathbf{k}) \\ -tf^*(\mathbf{k}) & -E \end{pmatrix} = 0, \tag{2.14}$$

which gives the following dispersion relation

$$E_\pm = \pm t\sqrt{1 + 4\cos\frac{3ak_x}{2}\cos\frac{\sqrt{3}ak_y}{2} + 4\cos^2\frac{\sqrt{3}ak_y}{2}}. \tag{2.15}$$

The + and - sign correspond to the conduction and valence bands, respectively. These two bands touch at the corners of the first Brillouin zone ($\mathbf{K}_+$ and $\mathbf{K}_-$ points), so that there is no band gap separating valence and conduction bands (see Fig. 2.2). As there are two free electrons in each unit cell, the valence band is completely filled while the conduction band is completely empty. The Fermi level is positioned at $E = 0$, and crosses the dispersion relation exactly at $\mathbf{K}_+$ and $\mathbf{K}_-$ points.

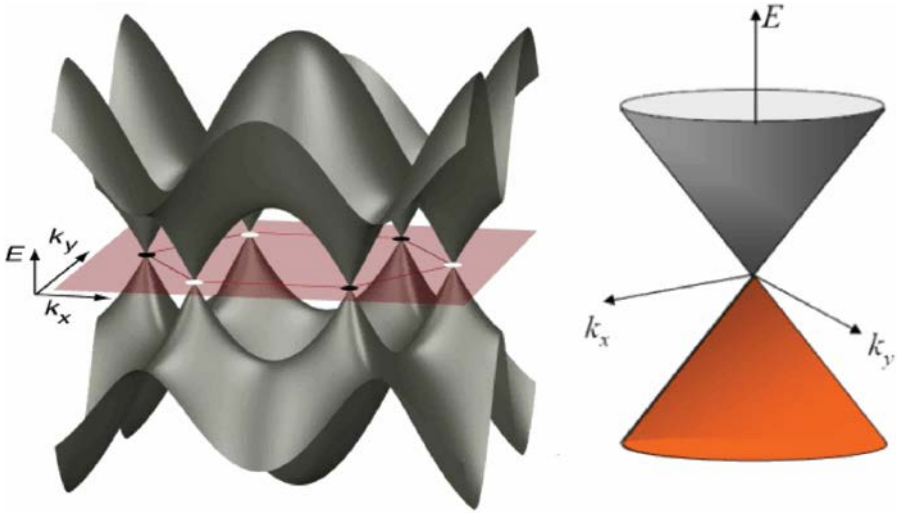

Figure 2.2: (Left panel) The energy dispersion of graphene calculated from the tight binding model. The conduction band and valence band touch at the $\mathbf{K}_+$ and $\mathbf{K}_-$ points, often referred to as Dirac points. (Right panel) Enlarging the energy dispersion around the Dirac points shows a conical shape of the conduction and valence band. Figure adapted from [3].

2.1.2 Dirac equation at low energies

The electronic structure of single layer graphene exhibits crossings of the conduction and valence bands at the corners of the Brillouin zone, namely at the $\mathbf{K}_+$ and $\mathbf{K}_-$ points. The position of these two inequivalent points in momentum space is given by $\mathbf{K}_\epsilon = \epsilon(\frac{4\pi}{3a}, 0)$ where $\epsilon = \pm$.

From the Hamiltonian obtained with the tight-binding model it is possible to conclude that at $\mathbf{K}_\epsilon$ points the coupling between the A and B sublattices disappears. The coupling is described by the hopping quantity $-tf(\mathbf{k})$. When the wavevector is exactly equal to $\mathbf{K}_\epsilon$ the function $f(\mathbf{k} = \mathbf{K}_\epsilon)$ is equal to

$$f(\mathbf{K}_\epsilon) = e^{i\mathbf{K}_\epsilon \boldsymbol{\delta}_1} + e^{i\mathbf{K}_\epsilon \boldsymbol{\delta}_2} + e^{i\mathbf{K}_\epsilon \boldsymbol{\delta}_3} = 0. \tag{2.16}$$

This perfect cancellation of the coupling with the three nearest neighbors does not occur once the wave vector is not exactly at the $\mathbf{K}_\epsilon$ points. If the wave vector is slightly different from $\mathbf{K}_\epsilon$ but still in the low-energy limit the momentum measured relative to $\mathbf{K}_\epsilon$ can be taken as

$$\mathbf{p} = \hbar\mathbf{k} - \hbar\mathbf{K}_\epsilon. \tag{2.17}$$

The function $f(\mathbf{k})$ in the vicinity of $\mathbf{K}_\epsilon$ and in the linear-momentum approximation becomes

$$f(\mathbf{k}) \approx -\frac{\sqrt{3}a}{2\hbar}(\epsilon p_x - i p_y). \tag{2.18}$$

As the $\mathbf{K}_\epsilon$ points are independent their electronic states are calculated separately using the effective long-wavelength Hamiltonians (with $\epsilon = \pm$)

$$\hat{H} = v \begin{pmatrix} 0 & \epsilon p_x - i p_y \\ \epsilon p_x + i p_y & 0 \end{pmatrix}, \tag{2.19}$$

where v is the Fermi velocity given by $-\sqrt{3}at/2\hbar = 10^6$ m/s.
At low energy the effective Hamiltonian can then be written in terms of Pauli matrices as

$$\hat{H} = v(\epsilon\sigma_x p_x + \sigma_y p_y), \tag{2.20}$$

with $\sigma = (\sigma_x, \sigma_y, \sigma_z)$.
The Schrödinger equation with this effective Hamiltonian for electrons at low-energies is equivalent to the Dirac equation and results in a linear dispersion

$$E_\pm = \pm vp, \tag{2.21}$$

where the $+$ sign refers to the conduction band and the $-$ to the valence band. The dispersion relation Eq. (2.22) gives rise to a conical shape of the electronic bands around the $\mathbf{K}_\epsilon$ points. As a consequence, the low-energy electrons in graphene are considered to be Dirac fermions because they are massless and move with constant velocity.
The resulting energy eigenfunctions have two-components

$$\Psi_\pm = \frac{1}{\sqrt{2}} \begin{pmatrix} 1 \\ \pm\epsilon e^{i\epsilon\varphi} \end{pmatrix} e^{i\mathbf{pr}/\hbar}, \tag{2.22}$$

with φ being a polar angle defined as $\varphi = \arctan(p_x/p_y)$. The two components of the wave function correspond to the relative amplitudes of the Bloch functions on the A and B sublattices. This wave function has the form of a spinor, and is commonly referred to as pseudospinor (where the term "pseudo" is used to differentiate it from the real spin of the electron, which is also present).

The pseudospin can be illustrated in the following way. Let us imagine that an electron in graphene sits only on the A atomic sites. This corresponds to pseudospin "up" state, and is illustrated in Fig 2.3a. If, on the other hand, the electron is located only on B sites, this would correspond to a pseudospin "down" state (Fig 2.3b). In graphene, a generic electron wave function is a linear combination of pseudospin "up" and pseudospin "down" states, as shown on Fig. 2.3c.

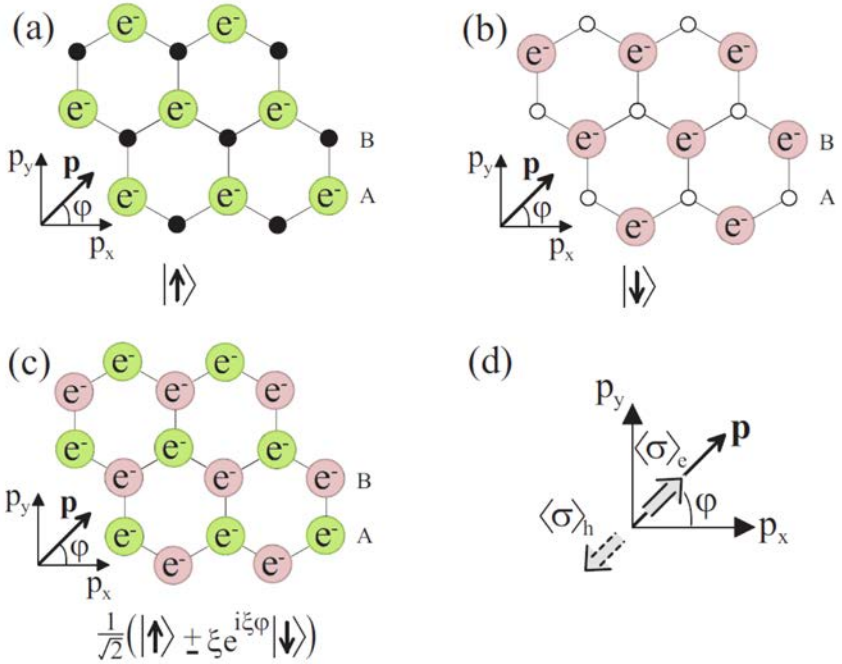

Figure 2.3: Illustration of pseudospin and chirality in graphene. a) Pseudospin "up" is associated to the situation when an electron wave function is located only on A atomic sites. b) Pseudospin "down" can be viewed as when the electron wave function is located only on B sites. c) In graphene, an electron wave function is shared between A and B sites, so that the pseudospin component of the wave function is linear combination of "up" and "down" states. d) Near the $\mathbf{K}_+$ point, the pseudospin of electron (hole) states in the conduction (valence) band is parallel (anti-parallel) to the momentum. The pseudospin directions are reversed near the $\mathbf{K}_-$ point. Figure adapted from [4].

An important property of graphene electrons is that they are also chiral which means that the direction of the pseudospin is linked to the direction of the momentum $\mathbf{p}$. For the $\mathbf{K}_+$ valley, the pseudospin is parallel to $\mathbf{p}$ in the

conduction band and anti-parallel to $\mathbf{p}$ in the valence band, see Fig. 2.3d. In the $\mathbf{K}_-$ valley the opposite happens. When the momentum of the particle rotates in-plane by an angle of 2π, the chiral wave function undergoes a π phase change which is exactly the same value of the phase acquired by a particle with spin 1/2 upon 2π rotation in the presence of magnetic field. This π phase shift is known as Berry's phase.

2.1.3 Consequences relevant for thesis

The discovery of graphene in 2004 by Manchester group [5], which marked the start of the exploration of a whole new class of two-dimensional materials, initiated an intense research on its physical properties. In particular, considerable attention has been devoted to the electronic properties of this system. Already the first experiments done on graphene-based field-effect transistor [5] showed that graphene supports both electron and hole transport. They also demonstrated that when subjected to strong magnetic fields, the relativistic nature of charge carriers in graphene leads to an unusual quantization sequence of the Hall resistance. This section gives an overview of the low-energy transport properties of graphene in the presence of an electric field and a magnetic field.

Electric field effect on graphene transport

Graphene devices are commonly made using graphene exfoliated from graphite crystals and deposited onto a degenerately doped Si wafer (acting like a gate electrode) covered with a SiO_2 layer. When a voltage is applied to the gate electrode a charge is accumulated in graphene. The concentration of electrostatically induced charge carriers can be obtained thinking of the system as a parallel plate capacitor

$$n = \frac{C_g V_g}{e}, \tag{2.23}$$

where C_g is the capacitence per unit area of the gate electrode, V_g is the applied gate voltage and e is a single electron charge. C_g is defined as a ratio of a relative dielectric constant $\epsilon_r = 3.9\epsilon_o$ of the SiO_2 oxide and the oxide thickness d_{ox} ($C_g = \epsilon_r/d_{ox}$).

The accumulation of charge shifts the Fermi level in graphene. An important consequence of the absence of a gap is that the Fermi level can be shifted continuously from the valence band to the conduction band, as illustrated in Fig. 2.4. For negative gate voltages, the Fermi level is located inside the valence band and transport occurs due to holes. In case of positive gate voltage, the Fermi level is in the conduction band, so that electrons are mediating

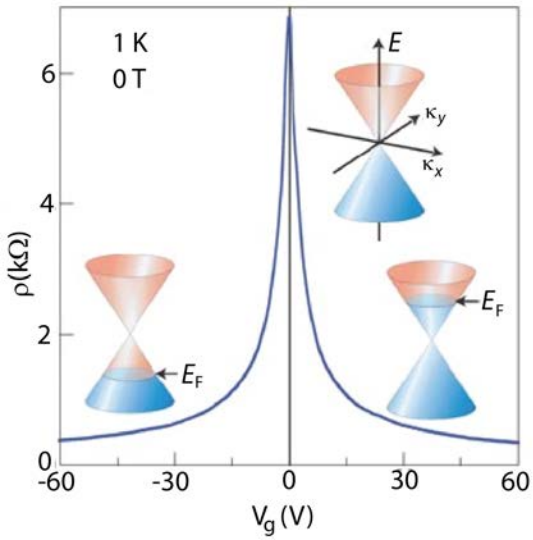

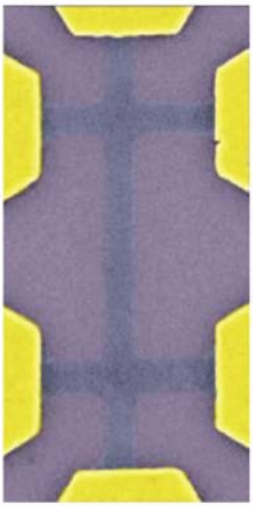

Figure 2.4: (Left panel) Resistivity of graphene as a function of gate voltage illustrating the occurrence of ambipolar field effect in graphene (adapted from ref. [6]). Under the influence of the gate bias, the Fermi level can be set in the valence or conduction band (the insets indicate the position of E_F for different V_g values in the low-energy spectrum). When the Fermi level is at the Dirac point, the resistivity exhibits a maximum. (Right panel) Example of a typical device used to probe field effect in graphene; with graphene etched in Hall-bar geometry, see dark purple region, and normal electrodes in yellow (adapted from ref. [7]).

transport.

In practice experiments show that when the Fermi level is sufficiently close to the charge neutrality point the conductivity becomes independent of carrier density. This phenomenon is known to arise due to the formation of "charge puddles", corresponding to electron and hole doped regions created by random potential fluctuations [2]. The appearance of the "charge puddles" prevents exploring the transport in the vicinity of Dirac point [8].

Quantum Hall effect in graphene

When a two-dimensional electron gas (2DEG) of sufficiently high quality is subjected to a perpendicular magnetic field, propagating electrons experience the Lorenz force and move in circular orbits. Quantum mechanically, electrons following these circular orbits can occupy only discrete energies known as Landau levels. When probed in transport measurements these discrete en-

ergy levels give rise to oscillations of the longitudinal resistivity, known as Shubnikov-de Haas oscillations, and to a quantized Hall resistivity (the quantum Hall effect).

In conventional conductors with a quadratic dispersion relation the energies of Landau levels are given by $E_N = \hbar\omega_c(N + 1/2)$ where N is an integer number that refers to N-th Landau level and ω_c is cyclotron frequency defined as $\omega_c = eB/m$. The energy gaps between successive Landau levels are independent on N and are equal to $\Delta E = \hbar\omega_c$. The lowest Landau level occurs at $E_0 = \hbar\omega_c/2$ and at zero energy there are no available states. The density of states of the 2DEG is a sequence of peaks, corresponding to delta functions broadened in energy by disorder. Between two Landau levels the density of states becomes vanishingly small. The density of states of each level is magnetic field dependent and given by $n = g_s g_v eB/h$, where g_s is the spin and g_v the valley degeneracy.

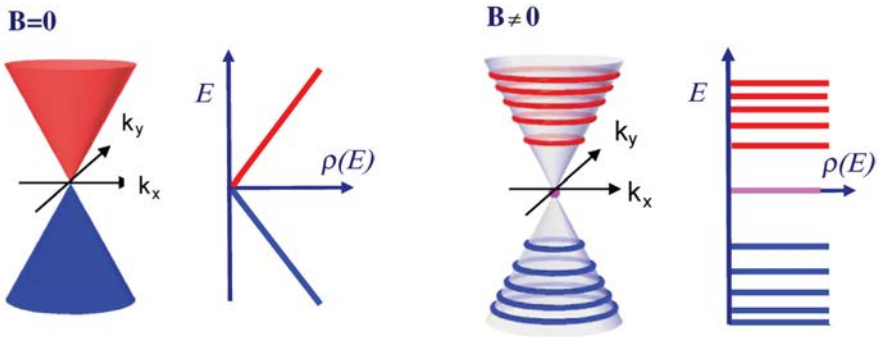

Figure 2.5: (Left panel) In the absence of magnetic field, the low-energy dispersion relation has conical shape and the corresponding density of states is linear in energy. (Right panel) In the case of strong magnetic field, the low-energy dispersion exhibits a discrete series of unevenly spaced Landau levels. The density of states becomes a sequence of peaks centered around the energies of the Landau levels. Figure adapted from [9].

A change in magnetic field shifts the positions of the Landau levels, and accordingly the peaks in the density of states. As a consequence, the longitudinal resistance, measured in a Hall device configuration, oscillates with magnetic field. When the Fermi level is located inside a Landau level, the longitudinal resistance exhibits a maximum, and when E_F is inside the gap the longitudinal resistance has a minimum, and eventually vanishes. The reason for this vanishing resistance is that at high magnetic fields the contribution of the edge states to transport becomes important. Edge states carrying current in only one direction are localized at one physical edge of the device, and states carrying current in other direction are localized on the opposite edge.

Since states propagating in different directions are spatially separated electrons move along the edges without any possibility to back-scatter. The Hall resistance then is quantized according to

$$R_{xy} = \frac{h}{\nu e^2}, \tag{2.24}$$

where $\nu = n/n_B$ is the filling factor and n_B is the degeneracy of a Landau level.

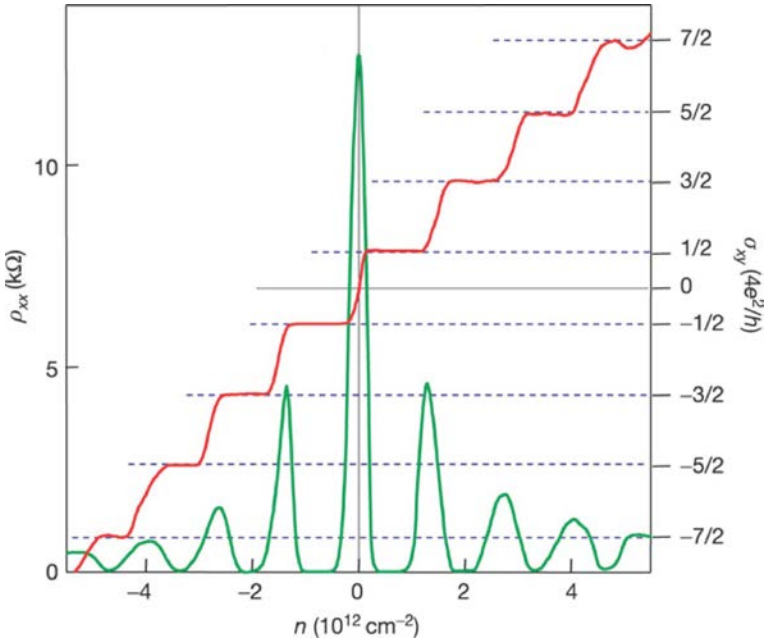

Figure 2.6: Quantum Hall effect in single layer graphene as a function of carrier concentration n. The longitudinal resistivity ρ_{xx} exhibits a peak at $n = 0$ in high magnetic fields due to a Landau level which is present at exactly zero energy. The electronic states for this level come from both conduction and valence band. The Hall conductivity σ_{xy} exhibits plateaus (red line) at the values indicated by the dashed lines σ_{xy} plateaus. Figure adapted from [7].

In graphene, the Hall resistance quantization occurs with a different sequence as compared to conventional conductors. This characteristic quantization is a direct consequence of the chiral nature of the electrons in graphene. Due to graphene's unconventional π Berry's phase the Landau levels can be found at energies given by $E_N = \pm v_F\sqrt{2e\hbar BN}$. The energy separation between two consecutive Landau levels is in the case of graphene dependent on

N as illustrated in Fig. 2.5. Moreover, for $N = 0$ there exist a Landau level exactly at zero energy, shared equally between electron and hole states, see Fig. 2.5. Because of this, the Hall resistance is quantized with the filling factor $\nu = 4(N + 1/2)$ where 4 accounts for the fourfold spin and valley degeneracy [7, 10, 11, 12]

$$R_{xy} = \frac{1}{4(N + 1/2)} \frac{h}{e^2}. \tag{2.25}$$

Figure 2.6 demonstrates the Hall conductance plateaus and oscillations of the longitudinal resistance in a single layer graphene. Because of this specific quantization sequence of the Hall resistance, quantum Hall measurements are regularly used to identify graphene.

2.2 Phase coherent electron transport

Two characteristic length scales are important to describe electron transport in mesoscopic systems at low temperatures, as sketched on Fig. 2.7. The mean free path (l_m) represents the average distance that electron travels through a conductor without undergoing scattering processes. If the dimensions of a conductor are shorter than the mean free path, no scattering occurs during the electron propagation and motion is said to be ballistic. In the opposite case (l_m much shorter than the dimensions of the conductor), electrons scatter many times during their propagation, each time changing direction of motion. In this regime, the electron motion is diffusive. The other important length scale is the phase coherence (L_ϕ) that describes up to what length electron propagates without loosing phase information. When L_ϕ is sufficiently long, quantum phenomena due to the wave character of electrons can become visible experimentally. Examples are so-called weak localization correction to the conductivity and universal conductance fluctuations.

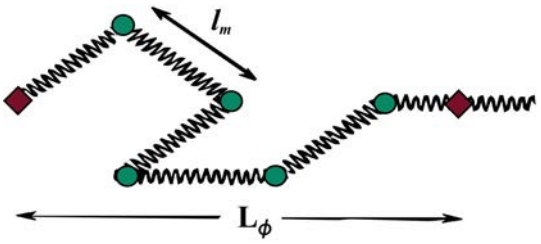

Figure 2.7: Illustration of an electron propagation in a conductor where the mean-free path l_m is much shorter then a phase coherence length L_ϕ. Wiggled lines represent electron motion, green circles elastic collisions and red squares inelastic collisions. Adapted from [13].

The coherence length depends on the nature of the impurity scatterers. Elastic scattering does not change the electron energy and normally phase coherence is preserved. In contrast inelastic scattering processes destroy phase coherence. The most important inelastic processes that lead to shortening of L_ϕ are electron-electron interaction and electron-phonon interactions. Lowering the temperature below $1K$ decreases the rate of the inelastic processes so that L_ϕ increases and the quantum interference effects become more pronounced [14, 15].

To explain the physics associated to the effects of electronic interference on transport we adopt a semiclassical approach, in which electron motion is described in terms of partial waves or trajectories, with an associated quantum amplitude of probability. In a diffusive conductor there are many possible trajectories connecting two different points in space. To calculate the probability of an electron to move from $\mathbf{r}_1$ to $\mathbf{r}_2$ during a certain time t, $P(\mathbf{r}_1, \mathbf{r}_2, t)$, it is necessary to take into account all trajectories. This probability is given by the absolute value squared of the sum of all individual probability amplitudes A_i associated to different trajectories as [16, 17]

$$P(\mathbf{r}_1, \mathbf{r}_2, t) = \Big| \sum_i A_i \Big|^2, \tag{2.26}$$

which can be rewritten as

$$P(\mathbf{r}_1, \mathbf{r}_2, t) = \sum_j \big|A_j\big|^2 + \sum_{j,j' \neq k} A_j A_k e^{i(\phi_j - \phi_k)}, \tag{2.27}$$

where ϕ_j and ϕ_k are phases corresponding to trajectories j and k. The first term, the sum of the modulus square of the probability amplitudes of individual trajectories, represents the classical diffusion probability. The second term results from quantum interference of different trajectories. If the effect of interference is neglected and the second term is omitted, one finds the classical result (i.e. sum over probabilities)

$$P_c(\mathbf{r}_1, \mathbf{r}_2, t) = \sum_j \big|A_j\big|^2. \tag{2.28}$$

2.2.1 Ensemble-averaged and sample-specific quantum interference effects

There are two different types of quantum interference effect that are experimentally relevant, and that lead to so-called ensemble-averaged (EA) and sample-specific (SS) phenomena. EA phenomena, such as weak localization and weak antilocalization, are defined by the average properties of the sample while the SS phenomena are determined by the sample details, such as

the precise impurity configuration. In experiments, these two quantum interference effects occur at the same time.

In this section we discuss weak localization as a typical example of EA phenomena and universal conductance fluctuations (UCF) as a typical example of SS phenomena. Additionally, we explain the ensemble-averaged procedures that are commonly used to distinguish these two effects. Later in this chapter, these concepts will be useful in the discussion of the proximity effect which is essentially a quantum interference effect.

Weak localization

At low temperatures, the probability for inelastic scattering processes to occur in a conductor is suppressed. Once no inelastic scattering events occur, the resistance is entirely due to elastic collisions with impurities and upon further lowering of the temperature it is expected not to change according to a semi-classical theory of transport. Contrary to this expectation, experiments reveal that often at low temperature the resistance starts to increase. This increase of the resistance occurs due to a quantum interference phenomenon called weak localization.

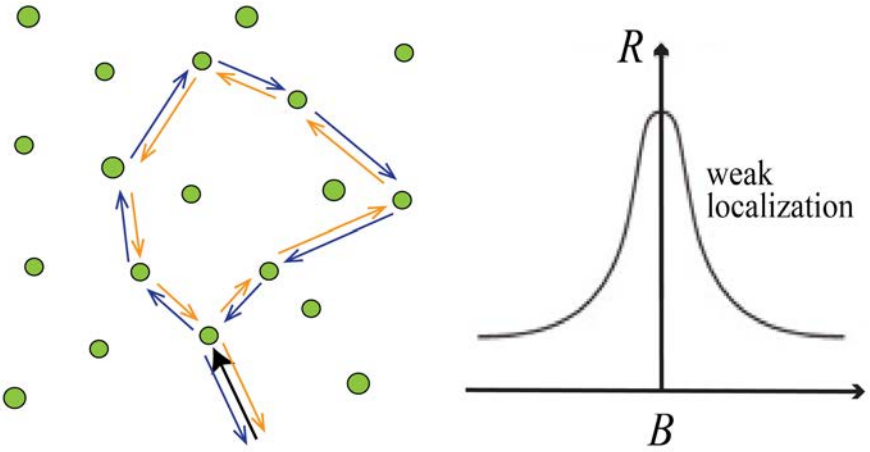

Figure 2.8: (Left panel) Mechanism of weak localization. The black arrow represents an incident electron wave. The time-reversed trajectories (orange and blue lines) have identical probability amplitudes and interfere constructively at the point of departure giving rise to weak localization effect. (Right panel) Weak localization is suppressed when a perpendicular magnetic field is applied.

In general, there is a large number of different trajectories that contribute to the quantum interference term in Eq. (2.28). As different trajectories are

uncorrelated, i.e. have uncorrelated phases, the contribution to the quantum interference term averages out. However, in the presence of time reversal symmetry (TRS), trajectories in which an electron comes back to its starting point give a non vanishing contribution to interference. In fact these trajectories can be traversed in a "clockwise" and in a "counterclockwise" sense, with exactly the same amplitude (because of TRS), as illustrated in Fig. 2.8. Upon summing these amplitudes and squaring, interference results in an enhanced probability for electrons to come back to the position where they started from. If all time-reversed trajectories are grouped together the probability of backscattering can be written as

$$P_b(\mathbf{r}_1, \mathbf{r}_1, t) = \sum_j A_j^2 + \sum_{j,j'} A_j A_{j'} e^{i(\phi_j - \phi_{j'})} + \sum_{j,j' \neq k} A_j A_k e^{i(\phi_j - \phi_k)}, \quad (2.29)$$

where A_j and $A_{j'}$ are the amplitudes of the time-reversed trajectories. Since A_j and $A_{j'}$ and phases associated to these trajectories (ϕ_j and $\phi_{j'}$) are the same, the second term is equal to the first one (i.e. the classical contribution). On the contrary, the interference term including all the trajectories that are not time-reversed averages out. As a result, the total probability for backscattering is doubled as compared to the classical result

$$P_b = 2 \sum_j A_j^2 = 2P_c. \quad (2.30)$$

This enhanced backscattering represents a tendency of electrons towards localization and leads to an increase of resistivity. This fact was used to coin the term a "weak localization".

Weak localization can be suppressed by removing time reversal symmetry between counterpropagating trajectories around the loop. This is typically done by applying a magnetic field so that the probability amplitudes of clockwise (A_j) and counterclockwise ($A_{j'}$) propagation acquire different phase shifts given by the following equations

$$\Delta\phi_j = k_F L - \frac{e}{\hbar} \int_{r_1}^{r_2} \mathbf{A} d\mathbf{r}_j, \quad (2.31)$$

$$\Delta\phi_{j'} = k_F L + \frac{e}{\hbar} \int_{r_1}^{r_2} \mathbf{A} d\mathbf{r}_j. \quad (2.32)$$

In Eq. 2.32 $d\mathbf{r}_{j'}$ is expressed in terms of $d\mathbf{r}_j$ since $d\mathbf{r}_{j'} = -d\mathbf{r}_j$. The first terms in these equations account for a standard dynamical phases whereas the second terms correspond to Aharonov-Bohm phases originating from the vector potential $\mathbf{A}$ associated to the applied magnetic field. The phase difference developed between these trajectories indicates breaking of time reversal

symmetry whenever magnetic field is non-zero

$$\Delta\phi_{j'} - \Delta\phi_j = \frac{2e}{\hbar}\int_{r_1}^{r_2} \mathbf{A}d\mathbf{r}_j = \frac{2e}{\hbar}\int_S (\nabla \times \mathbf{A})d\mathbf{S} = \frac{2e}{\hbar}\Phi, \tag{2.33}$$

where Φ is the magnetic flux enclosed by the trajectory. Since different counterpropagating trajectories, in general, enclose different areas, the phases accumulated in a magnetic field are random so that the interference term giving rise to weak localization averages out (see right panel in Fig. 2.8). At magnetic fields higher then $\sim \hbar/(2eL_\phi^2)$ weak localization is completely suppressed [17].

The evolution of weak localization in magnetic field is commonly used to determine the average coherence length of electrons and microscopic mechanisms inducing scattering of a charge carriers and affecting transport properties of samples.

Universal Conductance fluctuations

In diffusive systems, conductance fluctuations appear due to the "random" quantum interference of waves elastically scattered from impurities. The effect is due to the last term in Eq. 2.29, which disappears upon averaging, but that in devices of size comparable to L_ϕ gives a finite "random" contribution of magnitude $\sim e^2/h$. The contribution is random in the sense that it fluctuates upon changing microscopic details of device (i.e the position of an individual impurity). Even though these conductance fluctuations are random they are highly reproducible and can be easily distinguished from the experimental noise. In experiments, the conductance fluctuations are observed by varying the Fermi energy or magnetic field, as shown on Fig. 2.9. Their most important feature is that at zero temperature the fluctuation amplitude is found to be always of the same order $\delta G \propto e^2/h$ (as long as L_ϕ is larger than the sample size) regardless of sample details or degree of disorder provided that the transport through sample is diffusive [18, 19]. Considering this fact, Lee and Stone suggested Universal Conductance Fluctuations (UCF) as a name for this effect.

At sufficiently low temperatures, when the phase coherence is long and thermal averaging can be neglected, the expression for conductance fluctuation according to theory [20, 17] reads

$$\delta G \equiv \sqrt{Var(G)} = \frac{g_s g_v}{2}\beta^{-1/2} C \frac{e^2}{h}, \tag{2.34}$$

where C is a constant defined by the geometry of the sample (in case of long and narrow sample $C \approx 0.73$; in case of short and wide sample it is $C = \sqrt{W/L}$), g_s and g_v are respectively spin and valley degeneracy and β

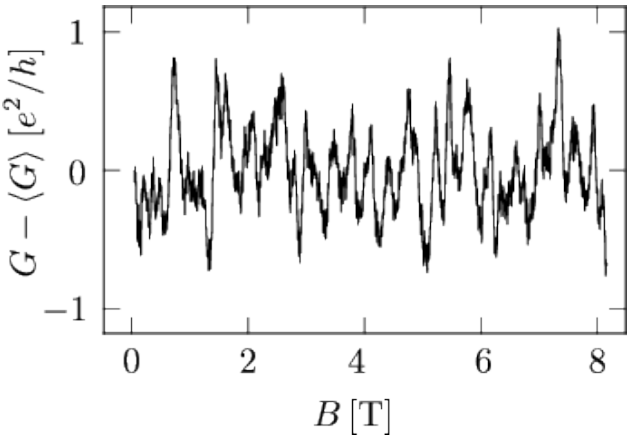

Figure 2.9: Conductance fluctuations as a function of perpendicular magnetic field of a gold wire at $T = 0.01$K. The conductance fluctuation pattern is random due to the random impurity potential fluctuations but it is highly reproducible. The root-mean-square of the conductance fluctuations is close to the e^2/h. Adapted from Ref. [13].

is equal to 1 in the absence of magnetic field and 2 when the time-reversal symmetry is broken by magnetic field.

The universality of the conduction fluctuation amplitude is due to the correlations among different trajectories through a disordered system. In order to have statistically independent trajectories the difference in energy between them should be larger than a certain correlation energy. This correlation energy was found by Thouless to be given by [21]

$$E_c \approx \frac{\hbar}{\tau_F} \approx \frac{\hbar D}{L^2}, \tag{2.35}$$

where τ_F is the time needed to traverse the sample of length L and $D = v_F^2 \tau_F$ is diffusion constant. E_c is normally referred to as "Thouless energy".

2.2.2 Ensemble-averaging procedure

As mentioned before, ensemble-average and sample-specific interference effects are present simultaneously in diffusive systems. If the device investigated has dimensions comparable to L_ϕ, the magnitude of SS and EA effects is comparable. As one is often interested in isolating the EA contribution only, a strategy needs to be developed to suppress SS effects. Experimentally the sample-specific component can be suppressed in much of the same way as it happens in sufficiently large samples by disorder averaging, i.e. systems consisting of large number of statistically independent pieces. In such large

systems, SS effects are suppressed as they are effectively averaged over many different microscopic realization of disorder. For small devices with dimensions comparable to L_ϕ, the "obvious" way is to prepare many microscopically different samples with the same ensemble properties. However, with the existing sample fabrication techniques this way of ensemble-averaging is not possible in practice. Instead it is possible to use a single sample to mimic the behavior of many samples that differ only in their impurity configuration. In fact for what concerns SS effects, a change in impurity configuration can be induced by a small modulation of external parameters such as carrier density or magnetic field [22, 23].

In order to obtain conditions corresponding to uncorrelated systems (i.e., to different microscopic impurity configurations) out of one sample, it is sufficient to induce a modification of Fermi energy ΔE_F or of magnetic field ΔB larger then the correlation energy E_c or correlation magnetic field B_c. The idea is that a change in E_F results in a random change of dynamical phase acquired by the electrons upon their propagation, which is conceptually equivalent to having a different microscopic configuration of impurities. The same is true when considering the effect of changing Aharonov-Bohm phases due to a small change in magnetic field. The correlation energy E_c for a diffusive system is equal to the Thouless energy. If the shift of the Fermi energy is smaller than the correlation energy, $\Delta E_F < E_c$, the impurity configuration effectively remains unchanged and there is no significant change in the interference pattern, i.e. the conductance fluctuations remain the same. In the opposite case, a shift in Fermi energy by more than E_c causes a complete change in the effective impurity configuration of the sample and results in a different conductance fluctuations pattern. In this case, the sample at E_F and at $E_F + \Delta E_F$ (as long as $\Delta E_F > E_c$) behave as two microscopically different but macroscopically identical systems. By averaging over N uncorrelated systems the root mean square amplitude of the conductance fluctuations decays as

$$\delta G \approx \frac{1}{\sqrt{N}}. \tag{2.36}$$

Similar arguments can be made for changes in magnetic field larger then B_c. In the process, care needs to be taken to ensure that E_c and B_c are small, so that changing E_F and B many times by E_c and B_c does not alter the ensemble properties of the system.

At finite temperature, $k_B T$ (k_B is Boltzmann constant) defines the energy range around the Fermi level in which electronic states contribute to transport. If $k_B T$ is smaller than E_c all trajectories traversing the sample are correlated and no averaging occurs. When $k_B T > E_c$ there are $N = k_B T / E_c$ uncorrelated sets of trajectories that give statistically independent contributions to the conductance fluctuations. The amplitude of the conductance fluc-

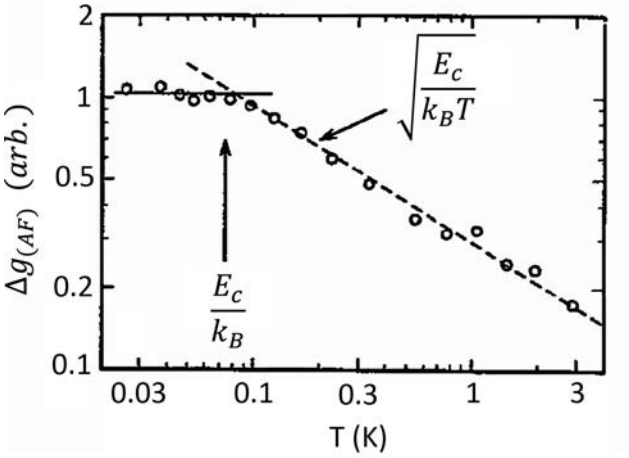

Figure 2.10: Temperature averaging showing how the root-mean-square of the sample specific fluctuations decreases with an increase of temperature according to $1/\sqrt{T}$. The dashed line represent the theoretical curve. Adapted from Ref. [13].

tuation averaged over N independent contributions decrease with $N^{-1/2}$ and in terms of temperature this implies

$$\delta G \approx \frac{1}{\sqrt{T}}, \tag{2.37}$$

as illustrated in Fig. 2.10 (under the assumption that in the entire temperature range the device dimension remains larger then L_ϕ).

2.3 Superconductivity

Superconductivity is a phenomenon that manifests itself through the absence of resistivity and exclusion of magnetic field in some metals below a certain critical temperature [24], see Fig. 2.11. The absence of resistivity was discovered by H. Kamerlingh Onnes in Leiden in 1911, shortly after he liquefied 4He for the first time, while measuring the resistivity of mercury as a function of temperature. The second fundamental property of superconducting materials -expulsion of magnetic flux- was discovered by W. Meissner and R. Ochsenfeld in 1933 and it is know as the Meissner effect. An indirect attractive interaction between two electrons was suggested by Frohlich [25] to be the mechanism which leads to superconductivity. In 1956 it was shown by Cooper that two electrons close to the Fermi surface, with opposite spin and momentum, can form a bound state under the influence of lattice vibrations

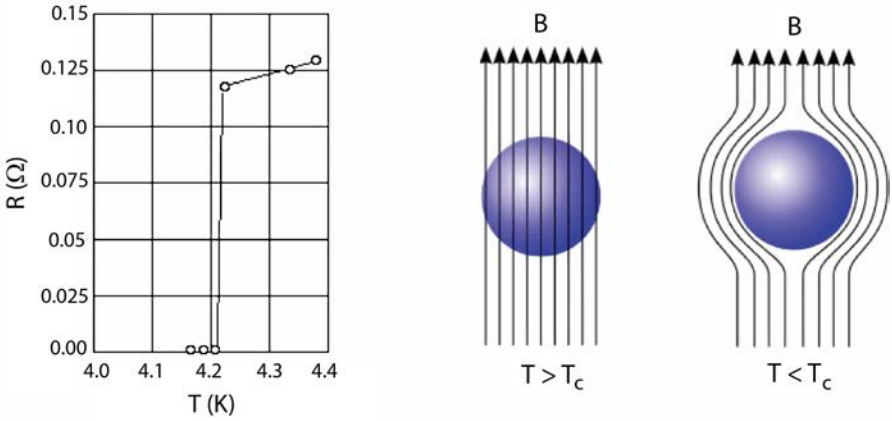

Figure 2.11: (Left panel) Resistance of mercury as a function of temperature exhibits a superconducting transition at $T_c = 4.2$K. (Right panel) Illustration of Meissner effect. When a metal is in the superconducting state ($T < T_c$) and if a magnetic field is not too strong, the metal expels the magnetic field completely.

[26]. Based on this attraction principle, Bardeen, Cooper and Schrieffer formulated the microscopic theory of superconductivity, known as BCS theory [27]. Here we present the very basic aspects of the superconductivity that are important for this thesis.

The properties of a superconductor can be described in terms of Cooper pairs that form the ground state of a superfluid condensate, described by a "macroscopic" wave function (or order parameter) $\psi(\mathbf{r}) = |\psi(\mathbf{r})| \exp(i\varphi(\mathbf{r}))$. Unpaired states represent quasi-particle excitations which are hole-like for $|\mathbf{k}| < k_F$, and electron-like for $|\mathbf{k}| > k_F$ (see Fig. 2.12a). The formation of the superconducting state gives rise to the opening of an energy gap Δ so that there are no available states in the energy window from $-\Delta$ to Δ (Fig. 2.12b).

The dynamics of electron-like and hole-like quasiparticle states are described by the Bogoliubov-de Gennes (BdG) equations [28] in conceptually the same way as the electron motion in a normal conductor is described by the Schrödinger equation. A useful aspect of the BdG equations is that they are well-suited for the description of systems with a spatially varying gap. This includes normal/superconducting junctions since a normal conductor can be simply described by setting $\Delta = 0$. The Bogoliubov-de Gennes equations have the form

$$\begin{pmatrix} H - E_F & \Delta(\mathbf{r}) \\ \Delta(\mathbf{r})^* & -(H^* - E_F) \end{pmatrix} \begin{pmatrix} \psi_e(\mathbf{r}) \\ \psi_h(\mathbf{r}) \end{pmatrix} = E \begin{pmatrix} \psi_e(\mathbf{r}) \\ \psi_h(\mathbf{r}) \end{pmatrix}, \qquad (2.38)$$

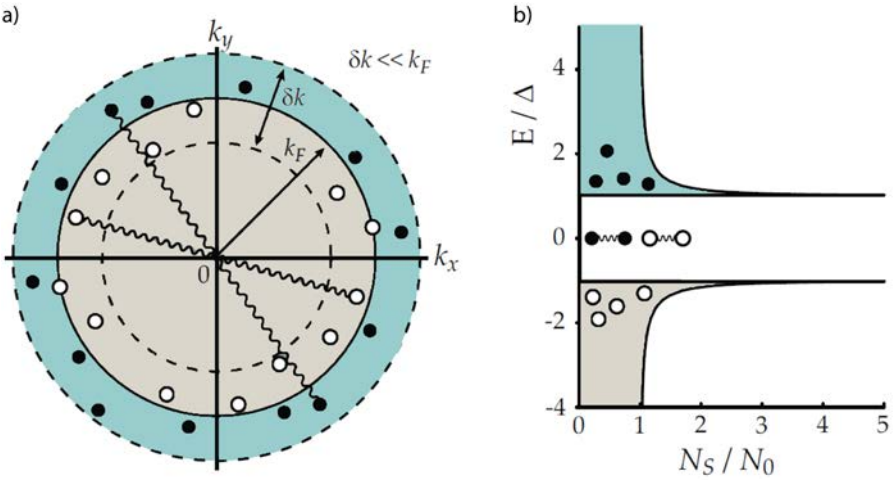

Figure 2.12: a) Cooper pairing in k-space. The light/dark shaded areas represent empty/occupied states, the black/white dots represent electron/hole excitations and wiggled lines represent the Cooper pairs. b) Quasi-particle spectrum for a BCS superconductor. The density of states N_S is normalized to the normal state density of states N_0 and the energy E to the gap Δ.

where H is the single particle Hamiltonian which contains the kinetic energy and all other single particle potentials, $\Delta(\mathbf{r})$ is the position dependent superconducting gap, E_F is the Fermi energy and E is the energy of the particle relative to E_F. The wave functions have two components corresponding to the electron part (top component) and hole part (bottom component) of the elementary excitations of the superconductor. From the BdG equations it is obvious that the coupling between electron-like and hole-like excitations, which is a phenomenon peculiar of superconductivity, occur when $\Delta(\mathbf{r})$ is finite. The solutions of the BdG equations in a uniform superconductor are plane waves. Their dispersion relation is shown in Fig. 2.13.

2.4 Andreev reflection

Although Cooper pairs are created only inside superconductors, they can enter a normal conductor in good electrical contact with a superconducting material, and affect its properties. This phenomenon is referred to as superconducting proximity effect. At energies below the superconducting gap transport of unpaired electrons is forbidden inside a superconductor. A normal current carried by individual electrons in a normal conductor therefore cannot enter a superconductor and need to be converted into a "Cooper pair"

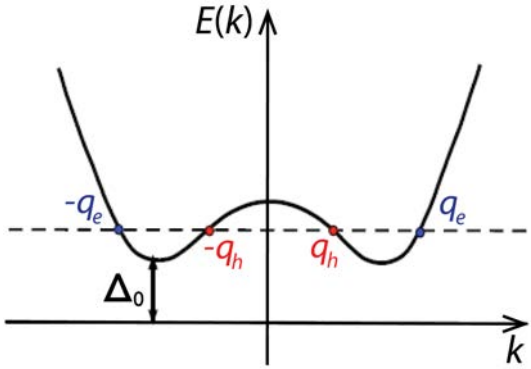

Figure 2.13: Dispersion relation for electron and hole quasi-particle excitations in the superconductor are found by solving the Bogoliubov-de Gennes equations.

current. The process that is responsible for this conversion and that allows charge transfer at the N/S interface is known as Andreev reflection [29].

An electron in a normal conductor, with energy lower than the superconducting gap Δ ($E < \Delta$), approaching the NS interface from the N side cannot enter S as there are no available states. Instead of being reflected in a conventional manner, the incoming electron couples with a second electron in N and is transferred across the N/S interface as a Cooper pair. As a result of this process a $2e$ charge joins the superconducting condensate as a Cooper pair while a missing electron in N gives origin to a hole reflected back from the interface. The wave function of the Andreev reflected hole acquires the phase of the condensate and traces back the path of the incident electron. This microscopic mechanism illustrated in Fig. 2.14 converts the dissipative current in N into a dissipationless current in S.

The reversed situation, when a supercurrent is converted into a normal electron current, can occur too. A hole reaches the N/S interface and, upon Andreev reflection, "splits" a Cooper pair in S. One of the electrons in the pair fills the hole. The other electron occupies an excited state in the conduction band above the Fermi energy with opposite momentum and spin as compared to the incoming hole. The net result of this process is that a charge $-2e$ is transferred from N to S.

2.4.1 Properties of Andreev reflection

Andreev reflection possesses several important properties (retro-reflection, phase coherence, and phase conjugation of electron and hole waves) that are needed to understand the work presented in this thesis. These properties

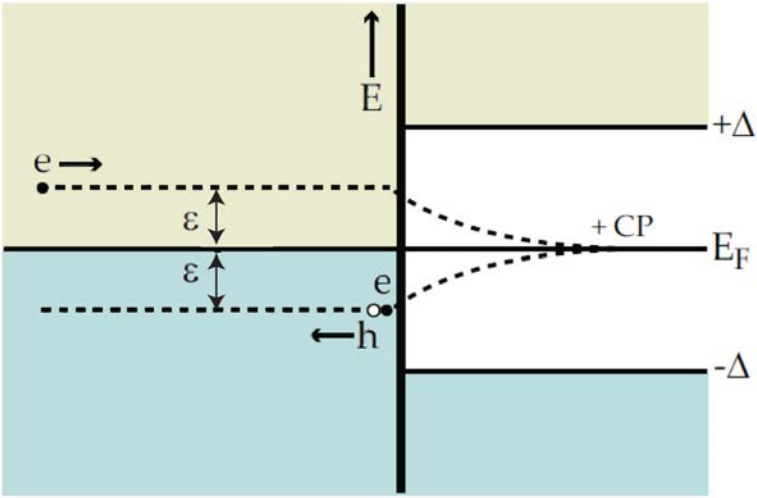

Figure 2.14: Schematic illustration of Andreev reflection. An incoming electron at energy ϵ creates an Andreev reflected hole at energy $-\epsilon$ in the normal conductor. At the same time, the incoming electron together with another electron at energy smaller than E_F are converted into a Cooper pair and enter the superconductor.

are explained here below.

Upon Andreev reflection, an incident electron at the Fermi energy with wavevector k_{e1} forms a Cooper pair with another electron in the normal conductor which has opposite momentum $k_{e2} = -k_{e1}$, because the momentum of Cooper pair is zero. The resulting reflected hole created in this process propagates inside N with a wavevector that is the same as that of the initial electron, since $k_h = -k_{e2} = k_{e1}$. The Andreev reflected hole, therefore, moves away from the NS interface by perfectly tracing back the path of the incoming electron. This property is called retro-reflection.

Andreev reflection is a phase coherent process and there is a well-defined relation between the phase of the wave function of the reflected hole and that of the incoming electron. Specifically the phase of the reflected hole wave function is shifted with respect to that of the incoming electron wave function by the phase of the superconducting order parameter and by an energy dependent term, according to the relation

$$\phi_h = \phi_e + \phi_S - \arccos\left(\frac{E}{\Delta}\right). \tag{2.39}$$

Similarly for an Andreev reflected hole, the phase of the back-reflected elec-

tron wave function is:

$$\phi_e = \phi_h + \phi_S + \arccos\left(\frac{E}{\Delta}\right). \tag{2.40}$$

Clearly, when considering the motion of electrons and holes in a normal conductor connected to a superconductor, also the phase of the wave function accumulated during their propagation (i.e. the dynamical phase) needs to be considered.

At the Fermi energy, when propagating along a path l, the wave function of the incoming electron acquires a dynamical phase given by $\theta_e = \int_l \mathbf{k}_e d\mathbf{l}$. The wave function of the retro-reflected hole, which traces back the path of the electron, acquires a phase $\theta_h = \int_l \mathbf{k}_h d\mathbf{l}$. The total dynamical phase gained in this process is then

$$\theta_{tot} = \int_l \mathbf{k}_e d\mathbf{l} + \int_l \mathbf{k}_h d\mathbf{l} + \theta_{AR}. \tag{2.41}$$

Since both particles follow the same path the wave vectors $\mathbf{k}_e$ and $\mathbf{k}_h$ have the same magnitude but opposite signs. Consequently, the dynamical phases exactly cancel out and the only phase contribution that remains is the one acquired upon Andreev reflection at the N/S interface

$$\theta_{tot} = \theta_{AR}. \tag{2.42}$$

At finite energy a difference in momentum is present between the initial electron and the reflected hole. As a result, the propagation through the diffusive normal conductor increases a dynamical phase. When the dynamical phase becomes of the order of π the electron and hole wave functions are not correlated anymore which is a key mechanism in the disappearance of superconducting proximity effect.

2.4.2 Effect of interface transparency on Andreev reflection

The quality of the NS interface has a significant influence on Andreev reflection. In real systems, the interface between N and S is never perfectly clean and any imperfection induces scattering. The effect of the interface transparency on Andreev reflection and transport in N/S systems has been discussed first by Bonder, Tinkham and Klapwijk (BTK) [30]. They were the first to solve the BdG equations for an N/S system with an arbitrary interface transparency considering all elastic processes involved in transport (normal reflection, Andreev reflection, transmission and branch-crossing transmission) in order to determine the current-voltage characteristics.

In the BTK model, the interface transparency is determined by the interface barrier strength, which is described by a parameter Z (proportional to

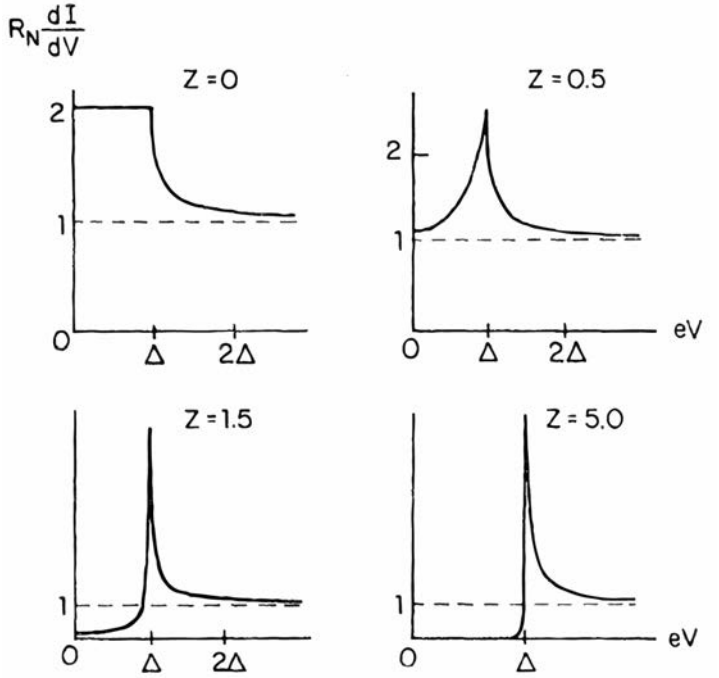

Figure 2.15: dI-dV characteristics of a N/S system as a function of voltage for different interface barrier strengths Z at zero temperature. In the absence of a barrier the dI-dV is twice the normal state value ($eV < \Delta$). In the case of a non-ideal interface, due to normal reflection, the probability for Andreev reflection is reduced (i.e. the charge transfer through the interface at $eV < \Delta$ is suppressed). For $Z = 50$ the transport is significantly suppressed and the dI-dV curve resembles the one of a tunnel junction. Adapted from [30].

the height of a delta barrier potential at the interface). The transmission probability of the N/S junction in the normal state is $T = (1 + Z^2)^{-1}$. The current flowing from the normal conductor to the superconductor when a bias V is applied is then given by:

$$I_{NS} = \alpha \int_{-\infty}^{\infty} [f_0(E - eV) - f_0(E)][1 + A(E) - B(E)]dE, \qquad (2.43)$$

where A and B are the energy-dependent probabilities for Andreev and ordinary reflection, $f_0(E)$ and $f_0(E-eV)$ are Fermi-Dirac distribution functions in S and N reservoirs, respectively. This equation shows that Andreev reflection enhances the current, since $A(E) > 0$.

From Eq. (2.43) it also follows that the differential conductance of the NS junction is proportional to $[1 + A(E) - B(E)]$. This relation allows to understand the evolution of the interface behavior as a function of Z (or equivalently) of transmission probability (shown in Fig. 2.15). In the absence of a barrier ($Z = 0$), the transmission probability is one and $A(E) = 1$ for $E < \Delta$: the injected electron can be only Andreev reflected as a hole and ordinary reflection vanishes $B = 0$. Accordingly, Andreev reflection doubles the charge transfer in the NS junction as compared to a normal system ($[1 + A(E) - B(E)] = 2$ for $E < \Delta$). For non-ideal interfaces ($Z > 0$) there is a probability that electrons are Andreev reflected but due to the presence of the barrier at the interface, electrons can now undergo normal reflection. In the subgap regime, since an electron is either Andreev reflected or reflected normally it must be $A + B = 1$, and so an increase of ordinary reflection leads to a decrease of Andreev reflection. When $Z \gg 1$ the transparency becomes very low and almost no transport occurs at $E < \Delta$. The dI-dV curve becomes the one of a tunnel junction.

2.5 Manifestation of Proximity effect in dissipative transport

The superconducting proximity effect occurs when a normal conductor is in a good electrical contact with a superconducting material and it is essentially a consequence of phase coherent propagation inside the normal conductor and Andreev reflection at the N/S boundary. This section gives a description of two aspects of proximity effect in dissipative transport -the so-called re-entrance effect and Andreev interferometry- that are relevant for this thesis.

2.5.1 Re-entrance effect

A counter-intuitive manifestation of the proximity effect is seen in the energy dependence of the conductance of a diffusive normal conductor connected to a superconductor through a highly transmissive interface. The temperature or voltage dependence of the conductance of such a NS system shows a non-monotonic behavior with a maximum appearing when k_BT or eV are of the order of the Thouless energy of the normal conductor. In the case when no interactions are present in the normal conductor, the conductance at zero temperature or voltage bias surprisingly has the same value as the one measured as when superconductor is in the normal state (i.e. at $T = 0$ and $V = 0$, $G = G_N$). This is the so-called re-entrance effect [31, 32, 33].

The re-entrance of the conductance as a function of energy can be qualitatively understood in terms of quantum interference of Andreev reflected

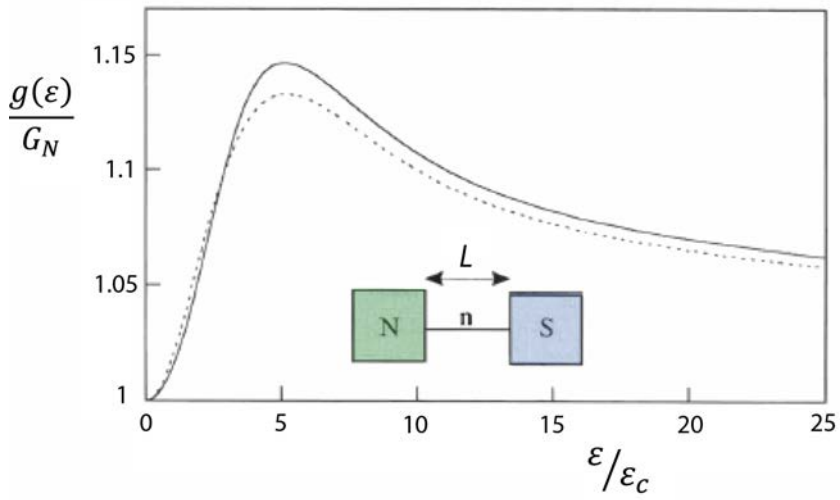

Figure 2.16: Illustration of re-entrance effect. Energy dependence of the spectral conductance of N/S junction is calculated using the full non-linear Usadel equation (full line) and in the linear approximation (dotted line) assuming the perfect interface transparency, infinite gap and infinite phase-breaking length. Figure adapted from [34].

holes. At $E = 0$, an incident electron approaching the NS interface is converted into a hole whose wave function acquires a phase $\pi/2$ ($\arccos(0) = \pi/2$) upon Andreev reflection. The Andreev reflected hole can be redirected towards superconductor, due to disorder, and it undergoes one more Andreev reflection. The wave function of the resulting electron then has its phase shifted by π relative to the phase of the incoming electron. The electron cannot interfere with the hole, however, it can interact once more with the superconducting condensate and be re-emitted as a hole which can then interfere with the partial wave associated to the first Andreev reflected hole. The amplitude associated to the path including 3 Andreev reflections has now opposite sign as compared to that including only one Andreev reflection. In general, if the motion in the normal metal is sufficiently diffusive, the hole can be Andreev reflected many times and paths with a different number of Andreev reflection processes have comparable amplitude. The sign of this amplitude however alternates. Since at $E = 0$ the dynamical phase exactly cancel due to phase conjugation, the total amplitude of probability for Andreev reflection is the sum of many terms equal in magnitude, but with alternating sign. The net result is a vanishing probability for Andreev reflection.

At low non-zero energies $E < E_{Th}$, the dynamical phases do not cancel

perfectly. As a result no perfect cancellation of the Andreev reflection amplitude occurs. When the energy is comparable to E_{Th}, the phase difference between trajectories of different number of Andreev refections is of the order of π, under which conditions the dynamical phase has maximum effect and a finite probability of Andreev reflection is observed. As the energy is increased well above E_{Th} the dynamical phase become so large that it randomizes all effects of interference between the different trajectories. In this case the total probability of Andreev reflection is again suppressed (which is why at high energy the resistance corresponds to the normal state value). Albeit only at a qualitative level, the physical picture outlined here correctly describes the re-entrance effect of the conductor in N/S diffusive systems with transparent interfaces.

2.5.2 Andreev interferometry

Another phenomenon that arises from the influence of the superconducting phase on a normal conductor transport is Andreev interferometry [35, 36, 37, 38]. This is the result of two partial electronic waves undergoing Andreev reflections at two N/S interfaces with different phase of the superconducting order parameter, and interfering to determine the total probability of Andreev reflection. This particular manifestation of the proximity effect can be observed in devices called Andreev interferometers, which consist of a phase coherent conductor connected to a superconducting loop with two N/S interfaces connected in parallel. The schematic illustration of such an Andreev interferometer is shown in Fig. 2.17.

The application of magnetic field through the superconducting loop creates a phase difference of the condensate at the opposite ends of the loop, so that partial electron waves undergoing Andreev reflection at opposite N/S boundaries acquire different phases. The interference of these partial electron waves that carry the macroscopic phases from the opposite loop ends cause the conductance, and all other transport properties of N, to depend on the phase difference $\phi = \phi_{s1} - \phi_{s2}$ (where ϕ_{s1} and ϕ_{s2} are the macroscopic phases of electrode S1 and S2, respectively, see Fig. 2.18) in a periodic way.

In practice, the phase difference can be tuned by changing the magnetic flux through a superconducting loop that connects the two superconducting electrodes. The relation between the phase difference and the flux is given by

$$\phi_{s1} - \phi_{s2} = 2\pi \frac{\Phi}{\Phi_0}, \tag{2.44}$$

with $\Phi_0 = h/2e$ the superconducting flux quantum. As a result in the experiments one observes oscillations of the transport properties as a function of a magnetic field used to generate the magnetic flux. The period of the

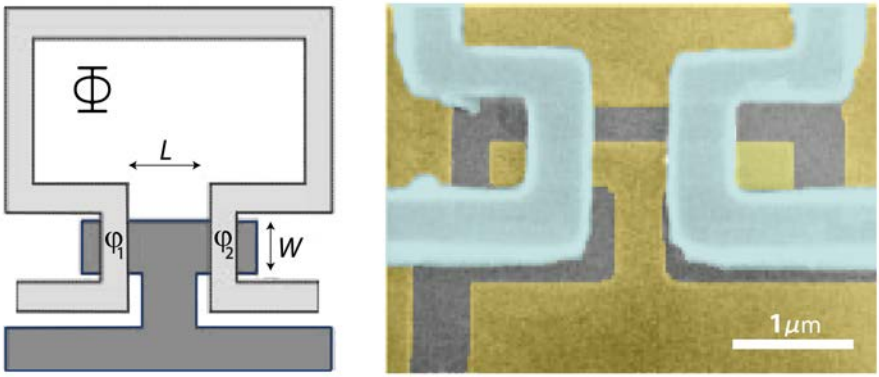

Figure 2.17: (Left panel) Schematic illustration of a T-shaped Andreev interferometer containing a superconducting loop and a T-shaped normal conductor. (Right panel) Scanning electron microscopy image of the device. The light-blue colored region represents the superconducting loop and the yellowish part is the normal conductor. Figure adapted from [39].

oscillations is

$$\Delta B = \frac{\Phi_0}{S}, \tag{2.45}$$

(with S area enclosed by the superconducting loop).

Andreev oscillations are determined by quantum interference which means that both ensemble-averaged and sample-specific effects contribute to the phenomenon. The ensemble-averaged component of conductance oscillations dominates at small magnetic fields and small energies (since it is phase conjugation that is responsible for the EA part of the effect). The EA contribution is suppressed by breaking time reversal symmetry (when magnetic flux threading the N conductor exceeds one flux quantum). Therefore, at high magnetic fields the EA component vanishes and only conductance oscillations due to the SS effect remain.

2.6 Transport in S/N/S structures

Here we discuss the transport phenomena occurring in SNS junctions, where Andreev reflection at both NS interfaces gives rise to a very rich physical behavior. In particular, we will discuss the existence of supercurrent flowing at zero bias, and its relation to so-called Andreev bound states [40, 41]. We will also briefly discuss dissipative transport in SNS structures.

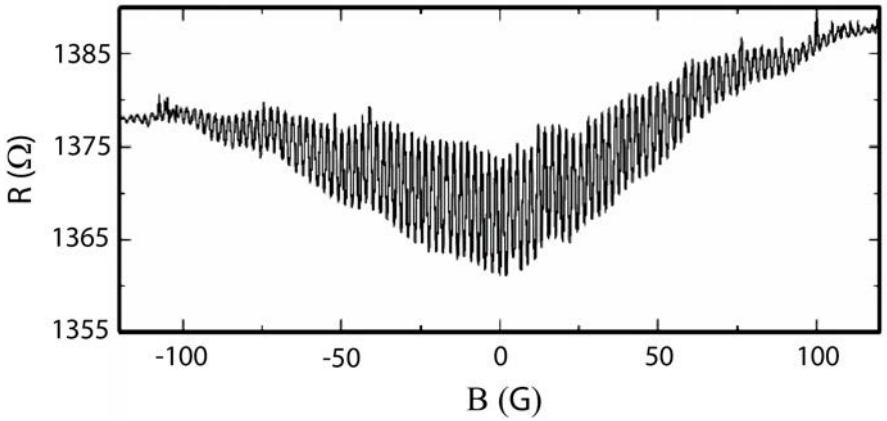

Figure 2.18: Resistance of the Andreev interferometer in Fig. 2.17 as a function of magnetic field. The resistance exhibits oscillations with a period defined by the geometry of device. Figure adapted from [39].

2.6.1 Non-dissipative transport

Andreev Bound States

Let us consider a 1D ballistic normal conductor attached to two superconducting reservoirs through ideal NS interfaces, as shown in Fig. 2.19. An electron in N with energy smaller than the superconducting gap $E < \Delta$ approaching the right superconductor is Andreev reflected as a hole with the same energy. The reflected hole retraces the path of the original electron and reaches the interface with the left superconductor where it is converted back into an electron upon Andreev reflection. The electron can then repeat the process, which results into an electron-hole periodic motion. At a quantum mechanical level, this semi-classical description implies that discrete levels inside normal conductor are formed, due to the spatial confinement of the electron-hole wave function caused by the superconducting gap. These states are called Andreev bound states. A remarkable property of Andreev bound states is that even though they are spatially localized they carry a net current. Indeed, the result of each electron-hole cycle is to transfer a Cooper pair from one superconductor to the other.

When the macroscopic phase difference between two superconducting condensates is zero, the time-reversed processes of the process just discussed above occurs at exactly the same energy. This time-reversed process consists in a hole (instead of an electron) incident on the right superconductor which is Andreev reflected into an electron at one N/S boundary, propagating back

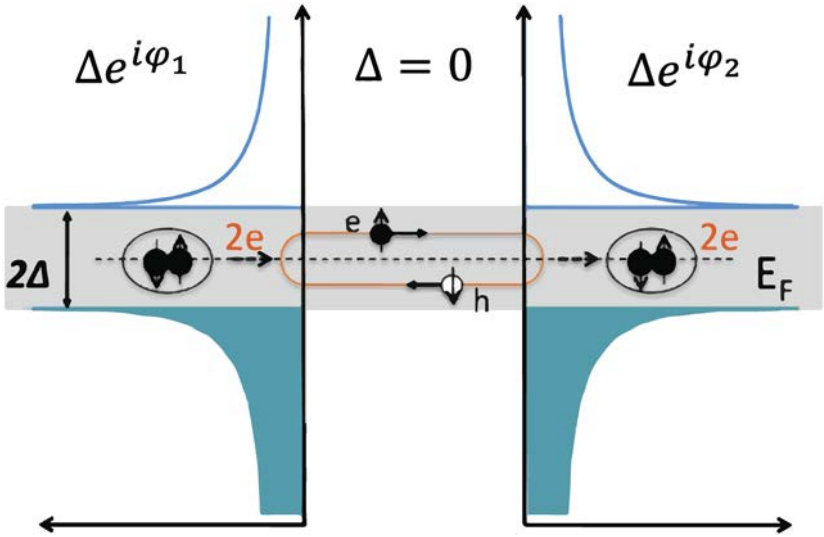

Figure 2.19: Schematic illustration of Andreev bound states. An incoming electron with energy $\epsilon < \Delta$ arrives at right N/S interface where it is Andreev reflected into a hole with energy ϵ. The reflected hole retraces the path of the incoming electron and reaches the left N/S interface where it is converted back into an electron. The resulting electron can then repeat the process. The periodic electron-hole motion leads to formation of Andreev bound states.

to the opposite boundary where it again generates a hole. As a result two time-reversed Andreev bound states are present at the same energy, and carry equal current in opposite directions. Under these conditions, therefore, the total current through a SNS junction vanishes. If a finite phase difference between the superconductors is present the two Andreev bound states are formed at different energies, and their occupation (determined in equilibrium by the Fermi-Dirac distribution function) is different. As a consequence also the contribution of the two states to the current is different (since this contribution is proportional to the occupation probability). A finite current can then flow at zero bias. This is the Josephson supercurrent.

Description of transport in SNS systems

To describe the electronic structure of a SNS junction we consider a spatially

dependent superconducting pair potential given by

$$\Delta(x) = \begin{cases} \Delta e^{i\phi_1}, & x < 0 \\ 0, & 0 < x < L \\ \Delta e^{i\phi_2}, & x > L \end{cases} \tag{2.46}$$

where ϕ_1 and ϕ_2 are the phases of the order parameter in the left ($x < 0$) and right ($x > L$) superconductor. Structures with a spatially dependent superconducting gap can be described using the Bogoliubov de Gennes (BdG) equations 2.38, with the normal-state single-particle Hamiltonian reads

$$H(x) = \frac{1}{2m}\Big(-i\hbar\frac{\partial}{\partial x}\Big)^2. \tag{2.47}$$

For a uniform superconductor (i.e., with gap Δ that is independent of position) the BdG equations give the spectrum of the elementary excitations shown in Fig. 2.13

$$E = \sqrt{\Big(\frac{\hbar^2 k^2}{2m} - E_F\Big)^2 + \Delta\Delta^*}, \tag{2.48}$$

and the corresponding electron-hole eigenfunctions. By setting $\Delta = 0$, the same BdG equations give eigenenergies and eigenfunctions of the excitations in the normal metal (that have either electron or hole character). The spectrum of energy states in the SNS junction can be obtained by writing the most generic wave function in the two superconducting electrodes and in the normal metal, and by imposing continuity of the wave functions and their derivatives at the two N/S interfaces. For energies smaller than the superconducting gap one then finds the equation [40, 41, 42]

$$2\arccos\Big(\frac{E}{\Delta}\Big) + \frac{L}{\xi_0}\frac{E}{\Delta} \pm \phi = 2\pi n, \tag{2.49}$$

whose solutions give the possible energy levels of electron-hole states confined in the SNS junction. In Eq. (2.48) $\xi_0 = \hbar v_F/2\Delta$ is the BCS coherence length, $\phi = \phi_1 - \phi_2$, and n an integer. The first and the last terms on the lefthand side of Eq. 2.49 are the phase shifts acquired by the evanescent electron/hole waves penetrating into the superconductor upon Andreev reflection, while the second term, $LE/\xi_0\Delta$, is the phase shift acquired from the free particle propagation through the normal region. The appearance of ϕ in equation [2.49] implies that the energies of the states depend on the phase difference of the superconducting condensates.

If the length of the SNS junction is short, the dynamical phase $LE/\xi_0\Delta$ is negligible and there exists only one solution below the gap, see Fig. 2.20. The energy of the Andreev bound state is determined only by the phase acquired due to the Andreev reflection and is given by

$$E(\phi) = \Delta\cos(\phi), \qquad -\pi < \phi < \pi. \tag{2.50}$$

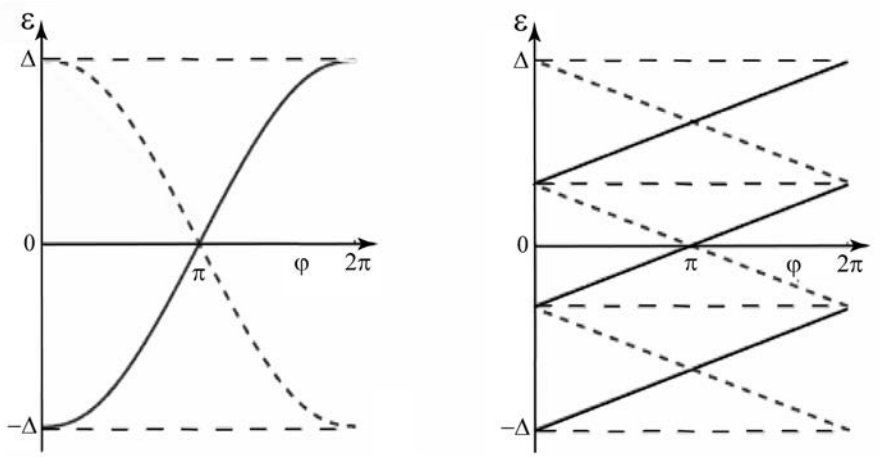

Figure 2.20: Dispersion relation of the Andreev bound states as a function of the superconducting phase difference ϕ for a short (left panel) and long (right panel) one dimensional ballistic junction. In the case of the short SNS junction there is only one state below the superconducting gap.

In the long junction limit, the dynamical phase dominates. When the junction length increases the number of bound states increases as well, leading to a smaller energy separation between neighboring levels. For $E \ll \Delta$ the expression for the energies of bound states reads

$$E_n^{\pm}(\phi) = \frac{\hbar v_F}{L}\Big[(n+\frac{1}{2}) \pm \phi\Big], \qquad -\pi < \phi < \pi, \tag{2.51}$$

where $\pm$ corresponds to bound states carrying a current in opposite directions. The Andreev bound states come in pairs since for every value of n there is the $+$ state denoting the state with right moving electron (left moving hole) and the $-$ state for left moving electron (right moving hole). When $\phi = 0$ the states $+$ and $-$ are degenerate, and when ϕ is non-zero time reversal symmetry is broken and the degeneracy is lifted.

Supercurrent in SNS systems

One of the most striking properties of Andreev bound states is that, even though they are spatially confined, they are able to carry the current in the absence of any bias. Here we discuss how this happens. At zero superconducting phase difference, for every state that carries current in one direction there is another degenerate state that carries the same current in the oppo-

site direction, so that the two contributions cancel exactly and the net current through the junction is zero. With a non-vanishing phase difference, time reversal symmetry is broken and the degeneracy between states carrying current in opposite directions is removed. The occupation probability of these bound states is then slightly different which result in a finite supercurrent flow. As the energy of the bound state depend on the superconducting phase difference the total supercurrent carried by these states at $T = 0K$ is given by

$$I_n^{\pm} = -\frac{2e}{\hbar} \sum_n \frac{dE_n^{\pm}}{d\phi}. \tag{2.52}$$

If there are states above the superconducting gap these states can also give a significant contribution to supercurrent. Hence, to calculate the total supercurrent it is necessary to consider all the supercurrent-carrying states. The solutions inside the continuum, referred to as Andreev resonances, are obtained from the same condition as the energies of Andreev bound states Eq. (2.48). Andreev resonances are also called "leaky Andreev levels", since electrons and holes moving with $E > \Delta$ can enter the superconducting condensate, which leads to a broadening of the energy levels as compared to the states with $E < \Delta$ [43]. The total supercurrent is expressed as the sum [40, 43]

$$I(\phi) = I_d(\phi) + I_c(\phi), \tag{2.53}$$

of contributions coming form the discrete levels (I_d) and that of the continuum levels (I_c). The contribution from the discrete levels can be written as

$$I_d(\phi) = \sum_n I_n^+(\phi) f(E_n^+(\phi)) + I_n^-(\phi) f(E_n^-(\phi)), \tag{2.54}$$

where I_n^+ is the supercurrent carried by states in the positive direction, $f(E_n^+)$ its occupation probability and, I_n^- and $f(E_n^-)$ the corresponding quantities for the states carrying current in the opposite direction. In the same spirit, the current carried by the continuum can be written as

$$I_c(\phi) = \Big(\int_{-\infty}^{-\Delta} + \int_{\Delta}^{\infty} \Big) I(E, \phi) f(E) \mathrm{d}E, \tag{2.55}$$

where $I(E, \phi)$ is the supercurrent-carrying density of states at $E > \Delta$.
By extending properly the definition of the supercurrent density of states and using properties of $f(E)$, the equations above can be written in the form

$$I_s(\phi) = \int_{-\infty}^{\infty} \big[1 - 2f(E)\big] I(E, \phi) \mathrm{d}E, \tag{2.56}$$

with the spectral current $I(E, \phi)$ that includes also the contribution of the discrete states.

The dependence of the supercurrent on the occupation probability of the states, $1 - 2f(E)$, provides a way to control supercurrent [42, 44, 45, 46]. It was predicted by Wilhelm et al. [47] that with suitable shape of $f(E)$ the supercurrent can be completely suppressed and even reversed. Experimentally, the reversal of the supercurrent direction was demonstrated by Baselmans et al. [48] which proved the importance of $f(E)$ in the normal metal to achieve control of the supercurrent.

2.6.2 Dissipative transport

The previous section focused on the origin of supercurrent in a SNS junction. When a finite bias is applied across such a structure, transport is dissipative and new processes need to be considered. Specifically, in this regime electrons and holes traveling inside the normal metal experience multiple Andreev reflections at the N/S interfaces.

In the presence of a voltage bias, transport in SNS junctions occurs also via Andreev reflection with a difference that upon each reflection on one of the N/S interfaces, electrons (holes) gain an energy corresponding to the bias eV. If the voltage bias is larger then 2Δ, an electron coming from the left superconductor can directly enter the right superconducting electrode, as sketched in Fig. 2.21a. Figure 2.21b illustrates electron transport through S/N/S junction when the bias is in a range $2\Delta \geq eV \geq \Delta$. An incoming electron undergoes one Andreev reflection at right N/S interface upon which a Cooper pair joins the right superconductor. Biasing the junction within an even lower range $\Delta \geq eV \geq 2\Delta/3$ leads to total transfer of three electrons, i.e. an incoming electron enters the right superconductor together with another electron as a Cooper pair; the Andreev reflected hole reaches the left interface and gets converted back into an electron with energy high enough to overcome the gap of the right superconductor (see Fig. 2.21c). Further decreasing the bias, with for instance $2\Delta/3 \geq eV \geq \Delta/4$, leads to transfer of four electrons, as shown in Fig. 2.21d. Taking this into consideration one sees that the number of Andreev reflections and number of transferred charge across SNS structure can be controlled by applied voltage bias. The number of Andreev reflections can be determined by formula

$$n = \frac{2\Delta}{eV}. \tag{2.57}$$

This multiple coherent Andreev reflections give rise to highly nonlinear IV curve of the SNS structures which exhibits subgap features at $V = 2\Delta/ne$. This subgap features correspond to a local minimas in the voltage dependence of differential resistance [30, 49]. These features are very informative since they allow the superconducting gap and transparency of normal

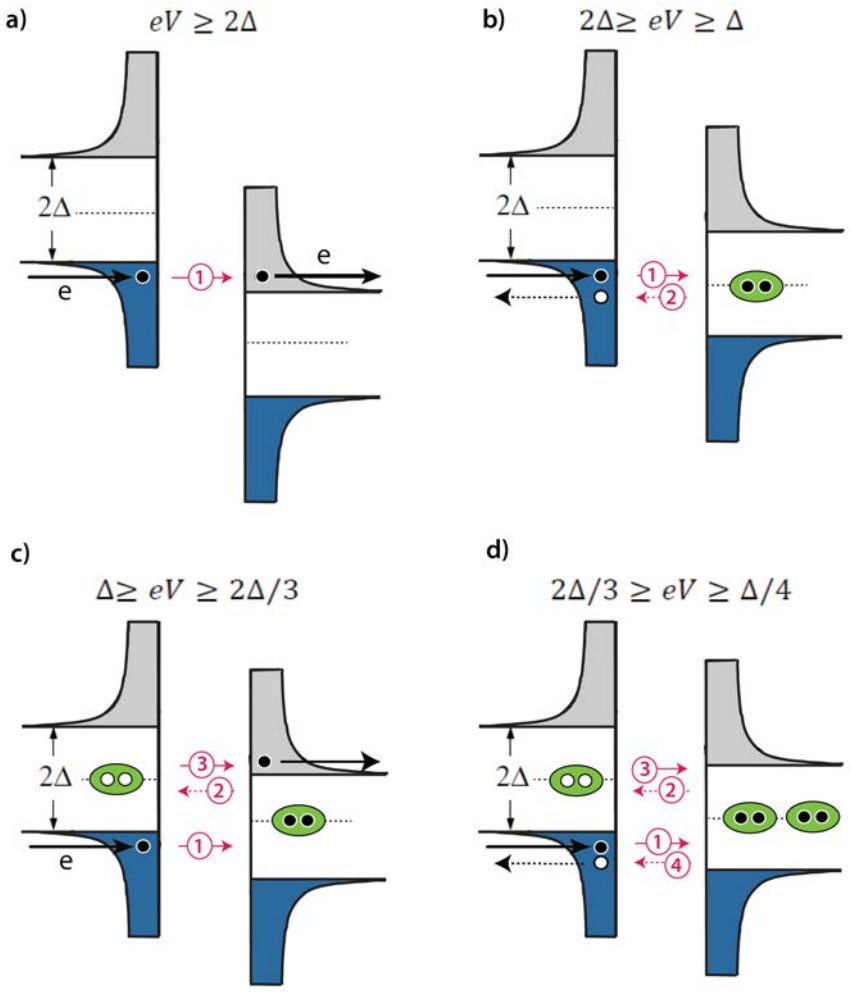

Figure 2.21: Illustration of multiple Andreev reflections in a S/N/S structure. Black/white dot represents an electron/hole, the full/dotted pink line represents the trajectory of an electron/hole. a) An electron with energy $eV > 2\Delta$ enters directly into a right superconductor. b) When the applied bias is $2\Delta \geq eV \geq \Delta$, electrons experience one Andreev reflections upon which they gain energy eV and are converted into holes that reach empty states inside the left superconductor. c) Two Andreev reflections occur when a voltage bias is $\Delta \geq eV \geq 2\Delta/3$. d) Transfer of two Cooper pairs for $2\Delta/3 \geq eV \geq \Delta/4$.

metal/superconductor interface to be determined, we will discuss this in more details in section §3.5.

2.7 Bibliography

[1] P. R. Wallace. The band theory of graphite. *Phys. Rev.*, 71:622–634, 1947.

[2] A. H. Castro Neto et al. The electronic properties of graphene. *Rev. Mod. Phys.*, 81:109–162, 2009.

[3] C. W. J. Beenakker. *Colloquium* : Andreev reflection and Klein tunneling in graphene. *Rev. Mod. Phys.*, 80:1337–1354, 2008.

[4] E. McCann. Electronic properties of monolayer and bilayer graphene. *Arxiv e-prints*, page 237, 2012.

[5] K. S. Novoselovet al. Electric field effect in atomically thin carbon films. *Science*, 306(5696):666–669, 2004.

[6] A. K. Geim and K. S. Novoselov. The rise of graphene. *Nat Mater*, 6(3):183–191, 2007.

[7] K. S. Novoselov et al. Two-dimensional gas of massless Dirac fermions in graphene. *Nature*, 438(7065):197–200, 2005.

[8] J. Martin et al. Observation of electron-hole puddles in graphene using a scanning single-electron transistor. *Nat Phys*, 4(2):144–148, 2008.

[9] Eva Y Andrei et al. Electronic properties of graphene: a perspective from scanning tunneling microscopy and magnetotransport. *Reports on Progress in Physics*, 75(5):056501, 2012.

[10] Y. Zhang et al. Experimental observation of the quantum Hall effect and Berry's phase in graphene. *Nature*, 438(7065):201–204, 2005.

[11] K. S. Novoselov et al. Unconventional quantum Hall effect and Berry's phase of 2π in bilayer graphene. *Nat Phys*, 2(3):177–180, 2006.

[12] Z. Jiang et al. Quantum hall states near the charge-neutral Dirac point in graphene. *Phys. Rev. Lett.*, 99:106802, 2007.

[13] S Washburn and R A Webb. Quantum transport in small disordered samples from the diffusive to the ballistic regime. *Reports on Progress in Physics*, 55(8):1311, 1992.

[14] P. M. Echternach et al. Nyquist phase relaxation in one-dimensional metal films. *Phys. Rev. B*, 48:11516–11519, 1993.

[15] P. Mohanty et al. Intrinsic decoherence in mesoscopic systems. *Phys. Rev. Lett.*, 78:3366–3369, 1997.

[16] Supriyo Datta. *Electronic Transport in Mesoscopic Systems*. Cambridge University Press, 1995.

[17] C. W. J. Beenakker and H. van Houten. Quantum Transport in Semiconductor Nanostructures. *eprint arXiv:cond-mat/0412664*, 2004.

[18] B. L. Al'tshuler and D. E. Khmel'nitskiĭ. Fluctuation properties of small conductors. *ZhETF Pisma Redaktsiiu*, 42:291, 1985.

[19] P. A. Lee and A. Douglas Stone. Universal conductance fluctuations in metals. *Phys. Rev. Lett.*, 55:1622–1625, 1985.

[20] P. A. Lee. Universal conductance fluctuations in disordered metals. *Physica A Statistical Mechanics and its Applications*, 140:169–174, 1986.

[21] D. J. Thouless. Maximum metallic resistance in thin wires. *Phys. Rev. Lett.*, 39:1167–1169, 1977.

[22] A. Douglas Stone. Magnetoresistance fluctuations in mesoscopic wires and rings. *Phys. Rev. Lett.*, 54:2692–2695, 1985.

[23] Philip F. Bagwell and Terry P. Orlando. Landauer's conductance formula and its generalization to finite voltages. *Phys. Rev. B*, 40:1456–1464, 1989.

[24] Michael Tinkham. *Introduction to superconductivity*. Dover Publications, New York,USA, 2004.

[25] H. Fröhlich. Theory of the superconducting state. i. the ground state at the absolute zero of temperature. *Phys. Rev.*, 79:845–856, 1950.

[26] Leon N. Cooper. Bound electron pairs in a degenerate Fermi gas. *Phys. Rev.*, 104:1189–1190, 1956.

[27] J. Bardeen, L. N. Cooper, and J. R. Schrieffer. Theory of superconductivity. *Phys. Rev.*, 108:1175–1204, 1957.

[28] P. G. De Gennes. *Superconductivity Of Metals And Alloys*. Addison-Wesley Publishing Company, 1992.

[29] A. F. Andreev. The thermal conductivity of the intermediate state in superconductors. *JETP*, 46:1823, 1964.

[30] G. E. Blonder, M. Tinkham, and T. M. Klapwijk. Transition from metallic to tunneling regimes in superconducting microconstrictions: Excess current, charge imbalance, and supercurrent conversion. *Phys. Rev. B*, 25:4515–4532, 1982.

[31] V. T. Petrashov et al. Phase memory effects in mesoscopic rings with superconducting "mirrors". *Phys. Rev. Lett.*, 70:347–350, 1993.

[32] V. T. Petrashov et al. Phase controlled conductance of mesoscopic structures with superconducting "mirrors". *Phys. Rev. Lett.*, 74:5268–5271, 1995.

[33] H. Courtois et al. Long-range coherence in a mesoscopic metal near a superconducting interface. *Phys. Rev. Lett.*, 76:130–133, 1996.

[34] H. Courtois et al. The spectral conductance of a proximity superconductor and the reentrance effect. *Journal of Low Temperature Physics*, 116(3-4):187–213, 1999.

[35] Hayato Nakano and Hideaki Takayanagi. Quasiparticle interferometer controlled by quantum-correlated Andreev reflection. *Phys. Rev. B*, 47:7986–7994, 1993.

[36] A. Dimoulas et al. Phase-dependent resistance in a superconductor-two-dimensional-electron-gas quasiparticle interferometer. *Phys. Rev. Lett.*, 74:602–605, 1995.

[37] A. F. Volkov and A. V. Zaitsev. Phase-coherent conductance of a superconductor-normal-metal quantum interferometer. *Phys. Rev. B*, 53:9267–9276, 1996.

[38] A. F. Morpurgo et al. Phase conjugated Andreev backscattering in two-dimensional ballistic cavities. *Phys. Rev. Lett.*, 78:2636–2639, 1997.

[39] S. G. den Hartog et al. Sample-specific conductance fluctuations modulated by the superconducting phase. *Phys. Rev. Lett.*, 76:4592–4595, 1996.

[40] I. O. Kulik. Macroscopic quantization and the proximity effect in s-n-s junctions. *JETP*, 30:1745, 1970.

[41] John Bardeen and Jared L. Johnson. Josephson current flow in pure superconducting-normal-superconducting junctions. *Phys. Rev. B*, 5:72–78, 1972.

[42] B. J. van Wees et al. Transmission formalism for supercurrent flow in multiprobe superconductor-semiconductor-superconductor devices. *Phys. Rev. B*, 44:470–473, 1991.

[43] Philip F. Bagwell. Suppression of the Josephson current through a narrow, mesoscopic, semiconductor channel by a single impurity. *Phys. Rev. B*, 46:12573–12586, 1992.

[44] A. F. Volkov. New phenomena in Josephson *SINIS* junctions. *Phys. Rev. Lett.*, 74:4730–4733, 1995.

[45] A. F. Volkov and H. Takayanagi. Long-range phase-coherent effects in the transport properties of mesoscopic superconductor–normal-metal structures. *Phys. Rev. B*, 56:11184–11194, 1997.

[46] Li-Fu Chang and Philip F. Bagwell. Control of Andreev-level occupation in a Josephson junction by a normal-metal probe. *Phys. Rev. B*, 55:12678–12690, 1997.

[47] F. K. Wilhelm et al. Mesoscopic superconducting–normal metal–superconducting transistor. *Phys. Rev. Lett.*, 81:1682–1685, 1998.

[48] J. J. A. Baselmans et al. Reversing the direction of the supercurrent in a controllable Josephson junction. *Nature*, 397(6714):43–45, 1999.

[49] M. Octavio et al. Subharmonic energy-gap structure in superconducting constrictions. *Phys. Rev. B*, 27:6739–6746, 1983.

Chapter 3

Device fabrication

This chapter describes the experimental procedures employed in the realization of devices studied in this thesis. Preparation of substrates, the very first step of device fabrication, includes writing of pre-patterned structure by means of electron beam lithography and metal deposition, as explained in section §3.1. Subsequently, graphene flakes are exfoliated from graphite crystals, transferred to the substrate and found with the help of an optical microscope. The use of an optical microscope, in addition, provides a simple and reliable way to identify the number of layers in a flakes (section §3.2). After contacting graphene with metal electrodes and defining the device geometry by etching, a sample is wire-bonded to a chip carrier in order to carry out transport measurements (section §3.3). All devices that we investigated aimed at exploring different aspects of the superconducting proximity effect which strongly depends on the quality of the superconducting film used to realize superconducting electrodes (discussed in more details in section §3.4), and the quality of the graphene/superconductor interface (discussed in section §3.5).

3.1 Substrate preparation

The process to fabricate graphene devices with superconducting electrodes starts by preparing a conventional Si/SiO_2 wafer with highly p-doped Si and 285 nm thick SiO_2 oxyde (illustrated in Fig. 3.1a), which serves as a supporting substrate and enables electrostatical gating. The substrates are pre-patterned (adding the alignment markers and bonding pads) to facilitate the search of graphene flakes and device design. This is done by using standard e-beam technology that involves writing a pattern in a resist (e-beam lithography), development of the exposed resist, deposition of metal and removal

of unexposed resist covered with metal (lift-off process).

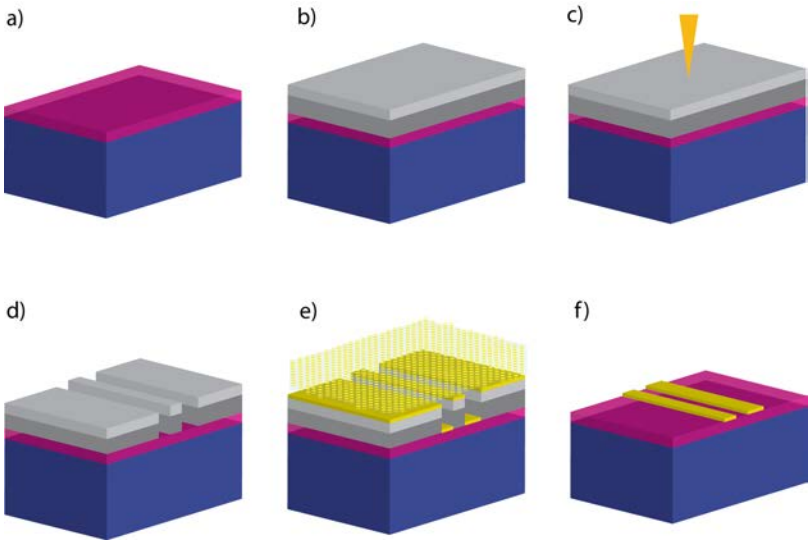

Figure 3.1: Typical steps of a sample fabrication process. a) Highly doped Si substrate with a 285nm thick SiO_2 oxide layer. b) The substrate coated with a bi-layer e-beam resist. c) The desired structure is "written" with a highly focused electron beam (e-beam lithography). d) By dissolving the e-beam exposed areas the desired mask is obtained (development). e) Metal is evaporated. f) The remaining resist covered with metal is removed (lift-off).

The advantage of using an e-beam lithography over UV-lithography is a higher resolution, i.e. e-beam lithography readily allows the realization of very fine structures which is essential for our work since the dimensions of our devices are often of the order of few hundred nanometers. E-beam lithography is performed on the substrate covered with a uniform layer of resist that is sensitive to an electron beam. The e-beam resist most commonly used is a high resolution positive resist called polymethylmethacylat (PMMA). PMMA can have different sensitivity to an electron beam depending on its molecular weight, which makes it very convenient for the realization of a mask for metal deposition. More specifically, creating a bi-layer resist (see Fig. 3.1b) with a bottom layer more sensitive than a top layer enables, upon development, the formation of undercuts. The undercuts facilitate the removal of unexposed regions of resist which are covered with metal in the subsequent so-called lift-off process. To write a desired pattern the bi-layer resist is exposed to a highly focused electron beam (the settings of the e-beam are carefully pre-determined by doing a dose tests), as sketched in Fig. 3.1c. The electron beam breaks

the polymer chains which become soluble in a chemical developer [1] so that the remaining resist constitutes a mask ready for metal deposition (see Fig. 3.1d).

The pre-patterned structure is then realized by evaporating metal (Fig. 3.1e). To obtain high quality films it is required, especially for the case of the superconducting materials, to achieve high vacuum inside the chamber where the evaporation takes place ($10^{-7} - 10^{-8}$ Torr). The evaporation is done by directing an electron beam with electromagnetic lenses towards a crucible to heat a metal which then evaporates, condenses on a substrate and forms a thin film. The alignment markers and bonding pads consist of a bi-layer Ti/Au (10nm/40nm) were titanium is used to improve the adhesion of the gold film. Lift-off is performed inside warm aceton that dissolves PMMA and, as a result, leaves only metal which has the same structure as the e-beam patterned mask (see Fig. 3.1f). The samples are then cleaned in aceton, isopropanol and nitric fuming acid immediately before graphene deposition. A pre-patterned structure with bonding pads and markers is shown in Fig. 3.2.

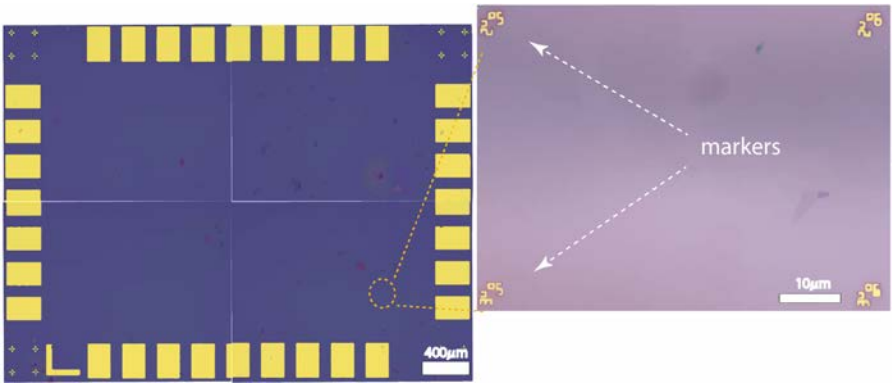

Figure 3.2: (Left panel) Optical image of a substrate with a pre-patterned structure. In the corners of the substrate one can find the crosses for alignment for e-beam lithography. (Right panel) An optical picture with higher magnification shows the markers used to located graphene flakes.

3.2 Graphene deposition and characterization

Concerning the production of graphene, new synthesis techniques and fabrication processes have been developed and improved since the original dis-

[1] The same priniciple applies to all positive resists. In a case of negative resists exposed parts become insoluble whereas the remaining region is dissolved in developer.

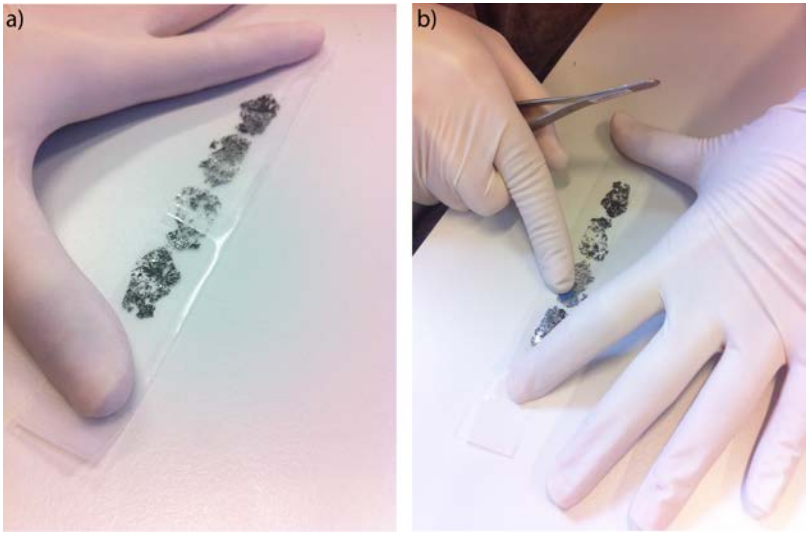

Figure 3.3: Deposition of graphene (a) Folding and unfolding of a scotch tape covered with graphite flakes (graphene exfoliation) (b) Transfer of a flakes from a tape onto a Si/SiO_2 substrate.

covery of this system [1]. Synthesis techniques, such as CVD [2, 3] or epitaxial growth on SiC substrates [4, 5, 6], are highly interesting for industrial purposes as they produce large graphene areas with quality comparable to graphene exfoliated from graphite using an adhesive tape [7, 3]. In practice, graphene devices of highest quality, i.e. the high charge carriers mobilities, are obtained for suspended graphene devices [9], where the influence of a substrate is completely removed leading to considerable suppression of disorder in graphene. Graphene devices on boron nitride [10, 11, 12] whose lattice constant almost coincides with graphene have also exceptionally high quality. Graphene devices produced following the method developed by Novoselov et al. in 2004 [1, 13], i.e. using Si/SiO_2 substrates, are of quality that is sufficient for the purposes of the research work done in this thesis.

To realize these devices we proceed as follows. A large graphite crystal is peeled several times by folding and unfolding a scotch tape to get thinner flakes (see Fig. 3.3a). After each unfolding step we search for the areas covered with thin graphene layers, and then we place the substrate on a chosen part of the tape. By gently pressing with a finger for some time, we transfer flakes from the tape to the substrate (Fig. 3.3b). The tape is slowly removed to avoid breaking of flakes adhering to the substrate. We dip the substrate into acetone and isopropanol to remove flakes that are not attached well to the surface and to dissolve the glue residues originating from the adhesive

tape. We search for the flakes with an optical microscope which allows us to determine their location relative to the alignment markers present on the substrate.

The inspected flakes differ in thickness and the thickness of thin flakes can be determined with a non-invasive optical contrast technique. This technique relies on the visibility of graphene [14] as the intensity of light reflected from graphene on a Si/SiO_2 substrate is slightly different from that of light directly reflected by the bare substrate. The contrast between the flake and the substrate depends on the thickness of the SiO_2 layer and is maximum at certain optical wavelengths. For a 285 nm thick insulating layer the highest contrast is achieved when the optical wavelength is in the green spectrum, hence, we employ a digital green filter of an optical microscope to magnify the effect [15, 16]. The contrast can be quantified by calculating the relative green shift, $RGS = (G_s - G_f)/G_s$, where G_f and G_s are the green components taken from the RGB value of a digital color picture of the flake and the nearby substrate, respectively. Figure 3.4 shows RGS values of a large number of flakes whose thicknesses correspond to a monolayer, bi-layer and tri-layer graphene.

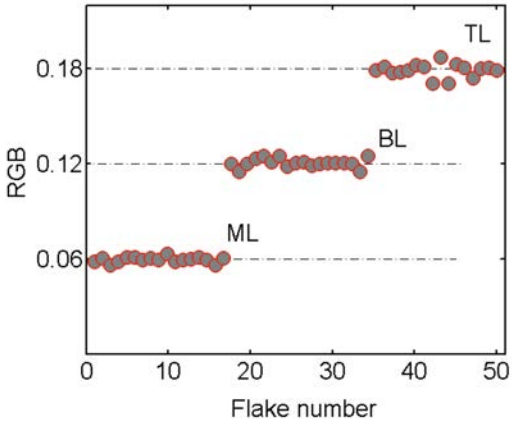

Figure 3.4: Identifying a number of layers in graphene with an optical microscope. The relative green shift for a monolayer (ML), bilayer (BL) and trilayer (TL) graphene.

Another reliable way to characterize graphene is to perform transport measurements in a high magnetic field. Single-layer graphene flakes contacted by metal electrodes exhibit a unique sequence of quantum Hall conductance steps at half-integer values of $4e^2/h$ which is a direct consequence of the linear dispersion of graphene, and is different from what one observes on bi or few-layer graphene. Figure 3.5 shows the two terminal conductance

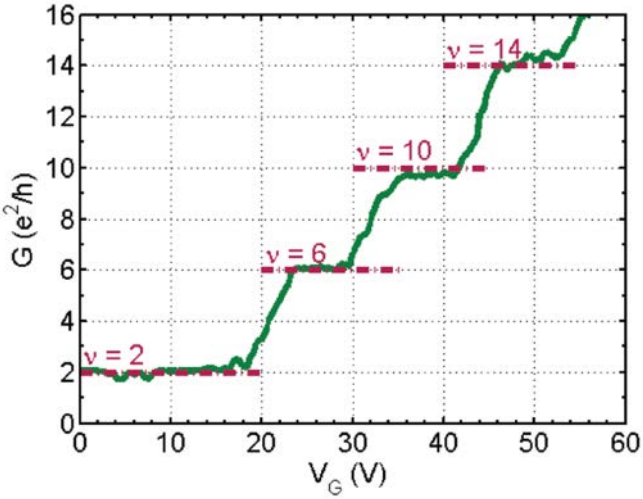

Figure 3.5: Conductance of our junction (200 nm long and 800 nm wide) measured in a two terminal configuration as a function of gate V_G, at $B = 10T$ and $T = 4.2K$, exhibiting the quantum Hall quantization steps characteristic of graphene monolayers.

of one of our junctions measured as a function of gate voltage, at $T = 4.2$ K and $B = 10$ T. Quantized conductance plateaus at 2, 6, 10, 14 e^2/h are clearly visible, which unambiguously identify graphene as monolayer.

3.3 Processing of graphene

Our research focuses on new aspects of superconducting proximity effect by using graphene as a diffusive normal conductor. Graphene, in comparison to conventional two-dimensional electron gas systems, enables a good contact to a superconductor which significantly simplifies the experimental realization of devices. Here we describe a typical fabrication procedure of our devices which starts by contacting graphene with a superconducting and normal metal electrodes, and then, defining its geometry by etching. This requires three different e-beam lithography steps, with subsequent exposure of well designed patterns. The sequence of these steps is illustrated in Fig. 3.6 on an example of specific device, the so-called multi-terminal Josephson junction, which consists of superconductor/graphene/superconductor junction where graphene region is connected to two additional normal contacts.

Figure 3.6a shows an optical image of a single-layer graphene flake selected for device fabrication. After selecting the flake, we define a superconducting structure with the first e-beam lithography step to reduce the con-

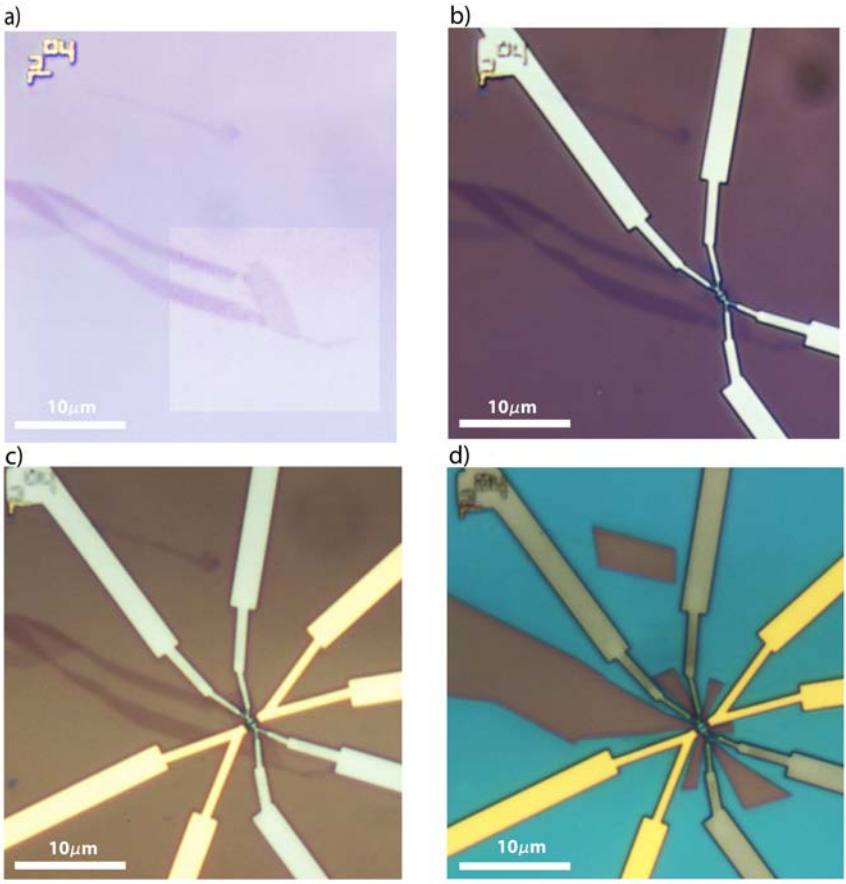

Figure 3.6: Realization of a graphene device (a) A graphene flake on a Si/SiO_2 substrate selected for device fabrication. (b) The superconducting electrodes are defined with a first e-beam lithography step, by evaporation and lift-off. c) Additional normal metal contacts are added to the device by e-beam patterning and lift-off. d) As a final step the geometry of graphene is defined by e-beam lithography and ion etching.

tamination originating from the e-beam resist. This considerably improves an electrical contact between graphene and superconducting electrodes which, for technical reasons, consist of a tri-layer Ti/V/Au $(3.5/10/3.5)$nm. An optical image of graphene with a superconducting structure is shown on Fig. 3.6b. The following lithography step is employed to realize a normal metal structure, as illustrated in Fig. 3.6c, for which we evaporate titanium and gold $(10/40)$nm. With the final e-beam lithography, we define which parts of graphene flake need to be removed, the so-called etching pattern (Fig. 3.6d).

The sample with a developed mask is then exposed to an oxygen plasma, immersed in a warm aceton to remove a remaining resist, and glued with a silver paste on a chip carrier. At this stage, the chip carrier with the sample can be mounted into a measurement setup.

The contact pads of the chip carrier enable the transport measurement to be carried out by allowing an electrical connection to be made between the sample and a measurement system. The connection to the sample is achieved by soldering aluminum wire from the contact pads of the chip-carrier to the bonding pads on the chip with an ultrasonic bonding-machine. The parameters for soldering process are carefully chosen to avoid breaking of the SiO_2 insulating layer which, as a consequence, leads to an occurrence of a leakage currents between a backgate and the device.

3.4 Superconducting thin film

For the realization of superconducting structures in our devices vanadium turned out to be a good trade-off between physical properties and technical issues related to its use. For instance, aluminum is technically simple to use with graphene, however, its main drawback is low critical temperature, and consequently, low superconducting gap. Materials with higher superconducting gaps such as niobium and lead are more suitable, in the sense, that they allow proximity-effect experiments to be performed in wider energy range. Still, since niobium films with good quality cannot be produced by evaporating with PMMA whereas lead is unstable upon thermal cycling which causes degrading of the film, we did not select them for our devices. The main reasons for choosing vanadium come from the facts that it has larger superconducting gap than aluminum and it has lower number of technical problems compared to niobium and lead. Nevertheless, some technical problems in the case of vanadium are still present. They arise from a strong strain existing in their films which considerably limits the advantage of having larger superconducting gap.

When evaporated on top of graphene, with titanium as a buffer layer, strain in vanadium tends to damage the flakes even to the point that large cracks are produced. This is illustrated by the encircled regions of the scanning electron microscope images of flakes with vanadium contacts in Fig. 3.7a and Fig. 3.7b, where it can be seen that after the evaporation of vanadium the graphene layers are teared off. In addition, these figures show lifting of the vanadium electrodes themselves (bright regions) which is another manifestation of strain. Finally, one more strain-related problem is an appearance of cracks in PMMA that, upon evaporation of metal, leads to short circuits between the electrodes (see Fig. 3.7c). The effect of strain can be sufficiently suppressed by making thiner films and structures of smaller size. Significant

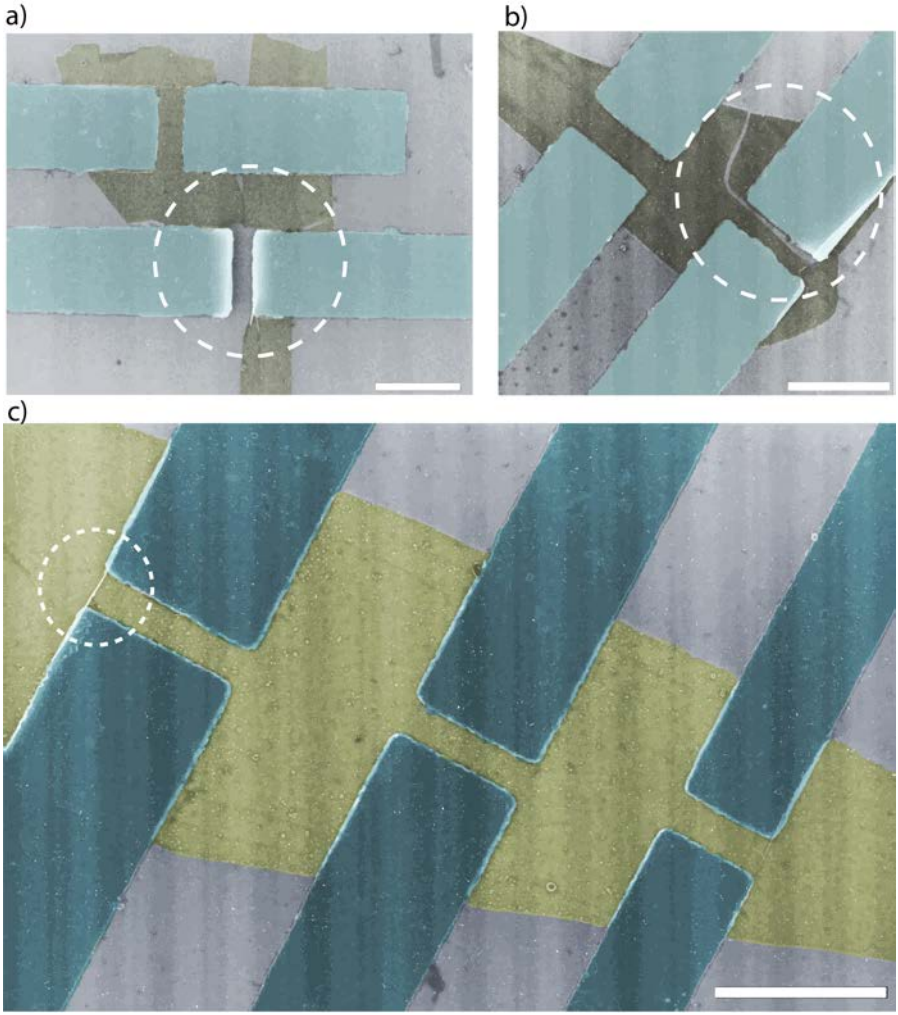

Figure 3.7: Scanning electron microscope images showing a consequences due to a strong strain in the vanadium film (scale bars correspond to 1μm). a) and b) Breaking of graphene followed by lifting of metal which is placed on top of the flake. c) Formation of cracks in an e-beam resist that are subsequently filled with metal during evaporation short circuiting the superconducting electrodes.

reduction of the thickness of the film needed to avoid breaking of graphene, however, also leads to a significant decrease of the critical temperature and, therefore, of the superconducting gap. Finally, the use of vanadium requires a very thin layer of gold to be evaporated on top, to prevent oxidation.

The critical temperature, $T_c \sim 2.5$K, and the superconducting gap, $\Delta \sim 380\mu$eV (calculated from $\Delta = 1.76 k_B T_c$), of our vanadium-based multi-layers are obtained from the temperature dependence of the resistance of 500nm wide, 10μm long and $3.5/10/3.5$ nm thick Ti/V/Au wire (see Fig. 3.8a) measured in a four-probe configuration. Figure 3.8b shows the differential resistance of a S/G/S junction as a function of voltage bias measured at -60V gate voltage and 250mK temperature. dV/dI-vs-V curve exhibits sub-gap features due to the occurrence of multiple Andreev reflections (discussed in §2.6.2) which are very informative as they allow determination of superconducting gap and graphene/superconductor interface transparency. Regarding the superconducting gap, we extract from dV/dI-vs-V curve the gap value, $\Delta \sim 300\mu$eV, which is comparable to the one obtained from the critical temperature of the superconducting wire. Information on graphene/superconductor interface transparency will be discussed in more details in next section.

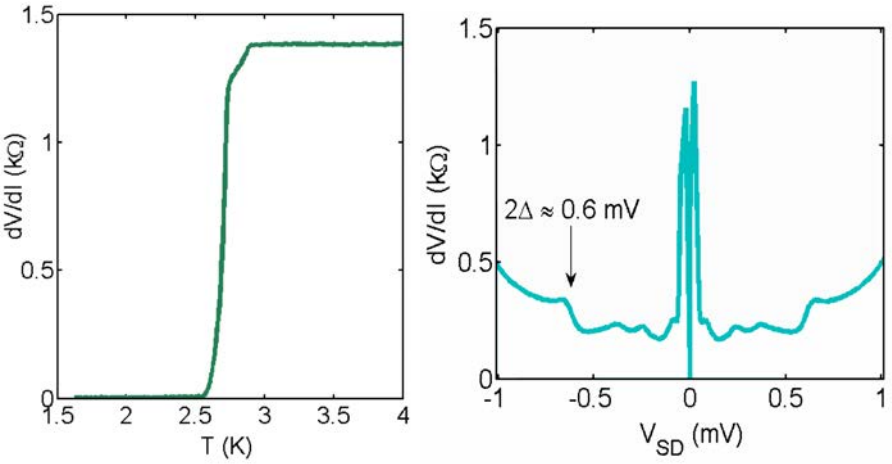

Figure 3.8: a) Temperature dependence of a differential resistance of superconducting wire exhibits a crossover to superconducting state at critical temperature $T_c \sim 2.5$K. b) Differential resistance as a function of voltage bias across a superconductor/graphene/superconductor junction, at $V_G = -60$V and $T = 250$mK, exhibiting the multiple Andreev reflection gives the value of the superconducting gap, $\Delta \sim 300\mu$eV.

3.5 Graphene/superconductor interface quality

The transparency between two materials has an important role in determining the transport properties of a device. In the case of our experiments it is essential to obtain a high transparency between graphene and the supercon-

ducting electrode in order to induce proximity effect. A clear indication of the large transmission probability of the interface between graphene and the superconducting electrodes is obtained by looking at the differential resistance of graphene-based superconducting junctions fabricated on a doped Si/SiO_2 substrate with the same technique and the same electrode composition as the devices studied in the thesis.

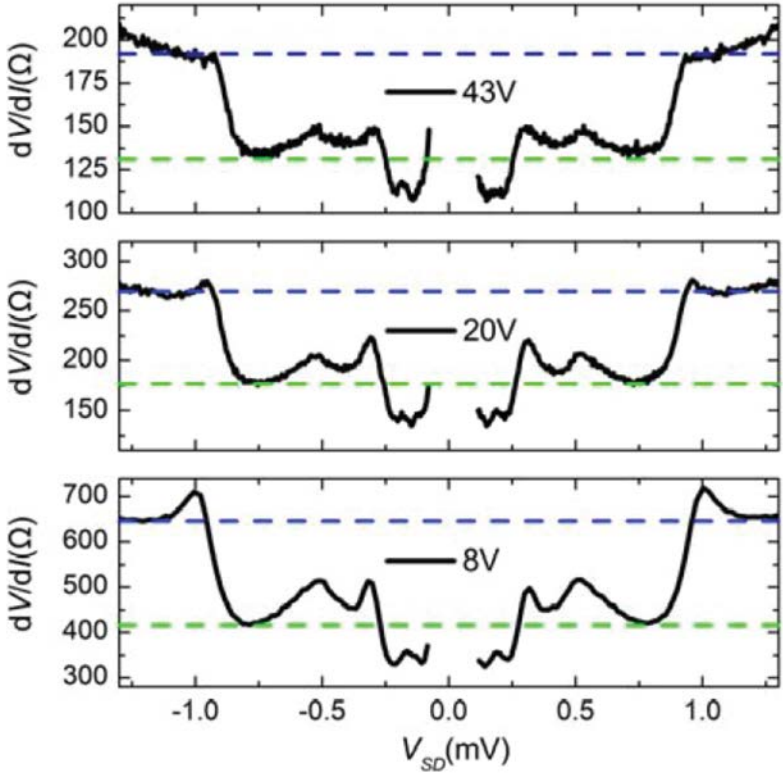

Figure 3.9: Differential resistance at $T = 250mK$ of a representative S/graphene/S test-junction, for gate voltages $V_{BG} = 43$, 20 and 8V (the Dirac peak is at $V_{BG} \sim 0V$ for this sample). Junction length and width are $L = 300nm$ and $W = 1.5\mu m$, respectively. The superconducting gap extracted from the SGS structure is $\Delta \sim 500\mu eV$ (near $V_{SD} = 0V$ the behavior of the measured differential resistance is affected by an artifact due to the supercurrent branch, which is shown in the panel below; this is why the data points are not shown in that range).

Figure 3.9 shows the differential resistance of a representative sample with junction width $W = 1.5\mu m$ and length $L = 300nm$, for different values of back-gate voltage V_{BG} (in this sample the Dirac peak was around $V_{BG} = 0V$).

The sharp and pronounced (exceeding 40%) suppression of the differential resistance for $\mid V_{SD} \mid < 2\Delta/e \sim 1mV$ indicates a very large probability for Andreev reflection and hence a large interface trasmissivity. In order to obtain a semi-quantitative estimate for the junction transmissivity, we have integrated dV/dI-vs-V in Fig. 3.9 to get dc current-voltage characteristics for the same V_{BG} as shown in Fig. 3.10. From curves in Fig. 3.10 we have estimated the excess current and compared it with the Octavio-Blonder-Tinkham-Klapwijk (OTBK) model [17]. Figure 3.11 shows the calculated dependence of the normalized excess current $eI_{exc}R_N/\Delta$ on the interface scattering parameter Z, according to the OTBK model. The values extracted from the dc current-voltage characteristics, shown in the inset to Fig. 3.10, are of the order of unity, and – remarkably – independent of V_{BG}. By comparison we extract for our S/G/S junctions $Z \sim 0.5$, and hence a junction transmissivity in the normal state $T \sim 80\%$.

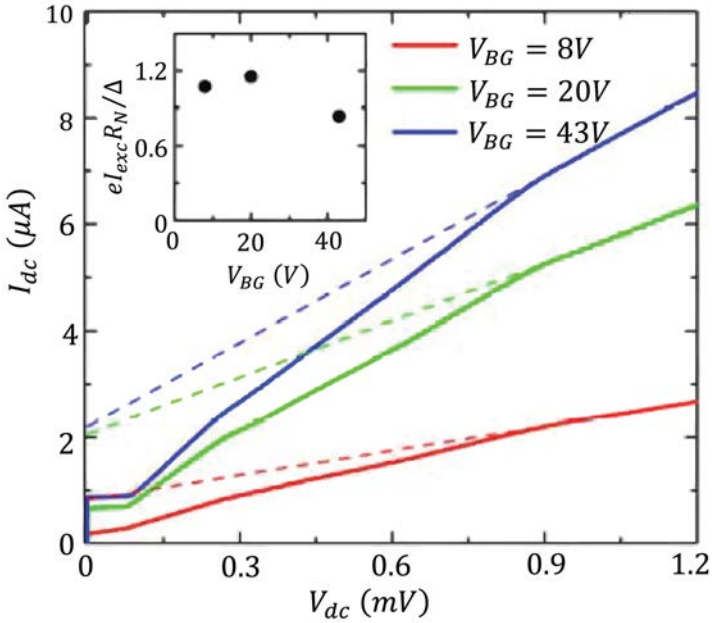

Figure 3.10: $I - V$ characteristics for the same devices and values as in Fig. 3.9, displaying large excess currents. The normalized values are shown in the inset.

The presence of a strong proximity effect in graphene is confirmed by the presence of a sizeable Josephson critical current, shown in Figure 3.12 for the same V_{BG} values as in Figure 3.10.

Several S/graphene/S samples of this tipe have been fabricated and tested,

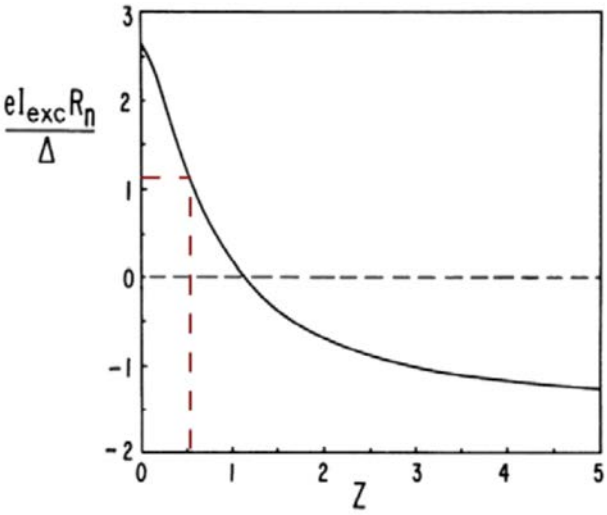

Figure 3.11: Excess current in a SNS junction according to the OTBK model (figure adapted from [17]). A normalized excess current corresponds to an interface parameter, hence to a transmission probability in the normal state.

allowing us to verify the reproducibility of the fabrication procedure.

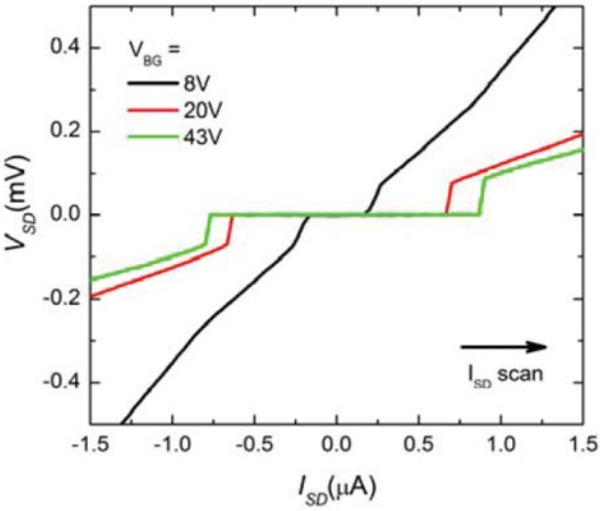

Figure 3.12: Current-voltage characteristic of the same sample, for the same V_{BG} values as in Fig. 3.9. Measurements are performed at $T = 250$ mK and $B = 0$.

3.6 Bibliography

[1] K. S. Novoselov, A. K. Geim, S. V. Morozov, D. Jiang, Y. Zhang, S. V. Dubonos, I. V. Grigorieva, and A. A. Firsov. Electric field effect in atomically thin carbon films. *Science*, 306(5696):666–669, 2004.

[2] Keun Soo Kim, Yue Zhao, Houk Jang, Sang Yoon Lee, Jong Min Kim, Kwang S. Kim, Jong-Hyun Ahn, Philip Kim, Jae-Young Choi, and Byung Hee Hong. Large-scale pattern growth of graphene films for stretchable transparent electrodes. *Nature*, 457(7230):706–710, February 2009.

[3] Nicholas Petrone, Cory R. Dean, Inanc Meric, Arend M. van der Zande, Pinshane Y. Huang, Lei Wang, David Muller, Kenneth L. Shepard, and James Hone. Chemical vapor deposition-derived graphene with electrical performance of exfoliated graphene. *Nano Letters*, 12(6):2751–2756, 2012. PMID: 22582828.

[4] Walt A. de Heer, Claire Berger, Xiaosong Wu, Phillip N. First, Edward H. Conrad, Xuebin Li, Tianbo Li, Michael Sprinkle, Joanna Hass, Marcin L. Sadowski, Marek Potemski, and Gérard Martinez. Epitaxial graphene. *Solid State Communications*, 143(1–2):92 – 100, 2007. Exploring graphene Recent research advances.

[5] A. K. Geim and K. S. Novoselov. The rise of graphene. *Nat Mater*, 6(3):183–191, March 2007.

[6] Th. Seyller, A. Bostwick, K. V. Emtsev, K. Horn, L. Ley, J. L. McChesney, T. Ohta, J. D. Riley, E. Rotenberg, and F. Speck. Epitaxial graphene: a new material. *physica status solidi (b)*, 245(7):1436–1446, 2008.

[7] Francesco Bonaccorso, Antonio Lombardo, Tawfique Hasan, Zhipei Sun, Luigi Colombo, and Andrea C. Ferrari. Production and processing of graphene and 2d crystals. *Materials Today*, 15(12):564 – 589, 2012.

[8] A. K. Geim. Graphene: Status and prospects. *Science*, 324(5934):1530–1534, 2009.

[9] D.-K. Ki and A. F. Morpurgo. High-quality multiterminal suspended graphene devices. *Nano Letters*, 13:5165-5170, 2013.

[10] C. R. Dean, A. F. Young, P. Cadden-Zimansky, L. Wang, H. Ren, K. Watanabe, T. Taniguchi, P. Kim, J. Hone, and K. L. Shepard. Multicomponent fractional quantum hall effect in graphene. *Nat Phys*, 7(9):693–696, September 2011.

[11] A. F. Young, C. R. Dean, L. Wang, H. Ren, P. Cadden-Zimansky, K. Watanabe, T. Taniguchi, J. Hone, K. L. Shepard, and P. Kim. Spin and valley quantum hall ferromagnetism in graphene. *Nat Phys*, 8(7):550–556, July 2012.

[12] L. A. Ponomarenko, R. V. Gorbachev, G. L. Yu, D. C. Elias, R. Jalil, A. A. Patel, A. Mishchenko, A. S. Mayorov, C. R. Woods, J. R. Wallbank, M. Mucha-Kruczynski, B. A. Piot, M. Potemski, I. V. Grigorieva, K. S. Novoselov, F. Guinea, V. I. Falko, and A. K. Geim. Cloning of dirac fermions in graphene superlattices. *Nature*, 497(7451):594–597, May 2013.

[13] K. S. Novoselov, A. K. Geim, S. V. Morozov, D. Jiang, M. I. Katsnelson, I. V. Grigorieva, S. V. Dubonos, and A. A. Firsov. Two-dimensional gas of massless dirac fermions in graphene. *Nature*, 438(7065):197–200, November 2005.

[14] P. Blake, E. W. Hill, A. H. Castro Neto, K. S. Novoselov, D. Jiang, R. Yang, T. J. Booth, and A. K. Geim. Making graphene visible. *Applied Physics Letters*, 91(6):–, 2007.

[15] Jeroen B. Oostinga, Hubert B. Heersche, Xinglan Liu, Alberto F. Morpurgo, and Lieven M. K. Vandersypen. Gate-induced insulating state in bilayer graphene devices. *Nat Mater*, 7(2):151–157, February 2008.

[16] M. Yamamoto M.F. Craciun, S. Russo, A. F. Morpurgo J. B. Oostinga, and S. Tarucha. Trilayer graphene is a semimetal with a gate-tunable band overlap. *Nat Nano*, 4(6):383–388, June 2009.

[17] M. Octavio, M. Tinkham, G. E. Blonder, and T. M. Klapwijk. Subharmonic energy-gap structure in superconducting constrictions. *Phys. Rev. B*, 27:6739–6746, Jun 1983.

Chapter 4

Tuning the influence of decoherence on proximity effect in a graphene Andreev interferometer

We discuss transport measurements through graphene Andreev interferometers exhibiting reentrance of the superconducting proximity effect.We observe that at high gate voltage (V_{BG}) the energy dependence of the Andreev conductance oscillations exhibits a scaling in agreement with theoretical expectations, which breaks down at low V_{BG}, when the Fermi energy approaches the charge neutrality point. The phenomenon is a manifestation of single particle dephasing that increasingly limits the propagation of superconducting correlations away from the superconductor-graphene interface. Our work addresses the interplay between microscopic decoherence and superconductivity, and shows that graphene provides a useful experimental platform to investigate unexplored regimes and phenomena in the superconducting proximity effect.

4.1 Introduction

Superconductivity originates from microscopic correlations between electron and hole excitations in the vicinity of the Fermi level of a normal metal, corresponding to the formation of Cooper pairs [1]. The characteristic length scale of these correlations—i.e., the size of a Cooper pair—is the superconducting coherence length ϵ, which in conventional metals at low temperature is usually much shorter than the phase coherence length of individual electrons L_ϕ. In this case, dephasing does not pose limits to the formation of the superconducting correlations, and superconductivity is only suppressed by thermal excitations at finite temperature. In the opposite case, when L_ϕ becomes comparable to ϵ, dephasing competes with superconductivity and, if L_ϕ becomes shorter than ϵ, it suppresses superconducting correlations. In conventional bulk superconductors this regime is realized only rarely. One example is provided by s-wave superconductors with spin impurities, where—upon increasing the impurity concentration—dephasing first results in gapless superconductivity, and eventually in the complete destruction of the superconducting state [2]. Given the relevance of the problem, it is worth finding new experimental systems where the competition between superconductivity and dephasing can be investigated under controlled conditions. To this end, induced superconductivity and proximity systems provide a significantly wider experimental flexibility [3, 4].

Here we present an experimental investigation of induced superconductivity, in nanoelectronic devices where the effective strength of dephasing can be tuned. Specifically, we investigate the superconducting proximity effect (PE) through measurements of phase-modulated transport in a diffusive Andreev interferometer [5, 6, 7] whose normal region is a T-shaped graphene ribbon. We exploit the possibility to electrostatically tune the carrier density in the ribbon over a very broad range. We find that at large densities induced superconductivity is suppressed by thermal fluctuations, as predicted by the conventional theory. As the carrier density is lowered, however, a crossover occurs to a regime in which the behavior of the PE is determined by dephasing, when L_ϕ becomes much shorter than the lateral dimension of our interferometer. Next to illustrating the competition between superconducting correlations and dephasing, our experiments show how graphene allows studying unexplored regimes of the superconducting proximity effect.

Our investigations focus on a specific manifestation of the PE, the so-called reentrance effect (RE) [8, 9, 10]. This counterintuitive phenomenon consists in the nonmonotonic energy dependence of the conductance of diffusive N/S junctions with highly transmissive interfaces. When the temperature T is lowered from just above the critical temperature T_C, the conductance first increases, and then unexpectedly decreases so that, in the ideal case, at $T = 0$

it returns to the normal-state value G_N, as if the PE was completely absent. A similar nonmonotonic trend is also observed at low temperature, when measuring the differential resistance as a function of applied bias V (i.e., decreasing V from $V > \Delta = e$ to 0; Δ is the superconducting gap), and in Andreev interferometers, when looking at the amplitude of the conductance oscillations as a function of bias or temperature. Although not yet observed experimentally, theoretical work indicates that the RE should occur also in graphene-based systems [11].

Theory treating the normal conductor in the diffusive limit relates the energy dependence of the conductance change $\delta G(E)$ to the Thouless energy $E_T = \hbar D/L^2$ (L is the length of the N region, and $E_T \ll \Delta$) and to the normal state resistance $R_N = 1/G_N$ [12, 13, 14]. The hallmark of the theory is the universal scaling of the phenomenon in terms of reduced variables, i.e., when $R_N \delta G(E)$ is plotted as a function of E/E_T [12, 13, 14]. Pioneering experiments have observed the RE in systems where the normal conductor was either a thin metal film [[15, 16],[17, 18]] or a two-dimensional electron gas (2DEG) [[19, 20, 21],[22]], and found excellent qualitative agreement of the experiments with theoretical predictions (quantitative deviations, especially in the case of 2DEGs, were attributed to device nonidealities). However, the universality of the scaling between $R_N \delta G(E)$ and E/E_T has never been verified experimentally.

4.2 Sample characterization

Compared to devices used in the past, graphene Andreev interferometers provide a key experimental advantage, as they enable a stable and reproducible electrostatic tuning over a broad range of densities. This allows us to study experimentally the dependence of the RE on the transport parameters of the normal conductor. Figure 4.1(a) shows a SEM micrograph of one of our Andreev interferometers. A single-layer graphene flake is patterned into a T-shaped ribbon, connected to a superconducting loop, to control the relative phase of the superconducting order parameter $\delta\phi = 2\pi\Phi/\Phi_0$ (Φ is the magnetic flux threading the loop and $\Phi_0 = h/2e$). The device is fabricated on graphene exfoliated onto a degenerately doped Si wafer (coated with a 285 nm thick SiO_2 layer) acting as a gate electrode. Two probes are placed on the graphene region below the T. The superconducting loop and these electrodes consist of a trilayer of Ti/V/Au (layer thicknesses are 5/17/5 nm). Measurements on S/graphene/S microjunctions fabricated with the same process which is used to realize the Andreev interferometers indicate that the S/graphene contacts have very high transparency for all values of V_{BG}. The superconducting gap extracted from the subharmonic structure of these microjunctions is $\Delta \sim 500\mu eV$, which matches the one calculated

from $\Delta = 1.76 k_B T_c \sim 530 \mu eV$ with $T_c = 3.5$ K of the film.

Experiments were performed in a filtered 3He system, down to 250 mK. The single-layer nature of the graphene flake was confirmed by two-probe quantum Hall measurements between contacts 3 and 4 [23, 24]. The resistance across the ribbon, measured at $B = 0$ as a function of V_{BG} [Fig.4.1(b)], raises by 2 orders of magnitude near the charge neutrality point. The strong suppression of the low-bias conductance near charge neutrality is typical of etched graphene nanoribbons, and is related to disorder and electron-electron interactions (EEI): scattering by edge-disorder increases the tendency of electrons toward (Anderson) localization, enhancing the effect of EEI. Indeed, in sufficiently narrow ribbons this leads to the formation of a full transport gap originating from Coulomb blockade [25, 26, 27, 28, 29, 30]. Finally, Fig. 4.1(c) shows the conductance oscillations induced by a small magnetic field that modulates the superconducting phase, originating from quantum interference of holes Andreev reflected at the two different superconducting contacts.

4.3 Transport measurements

As the device transport properties are determined by quantum interference, we need to distinguish between ensemble-averaged (EA) and sample-specific (SS) contributions in the measured quantities. The SS component of the Andreev oscillations, which consists in phase-coherent conductance fluctuations modulated by the superconducting phase [19, 20, 21], is dominant at small energies or at large magnetic fields, where the EA component is suppressed, respectively, by the RE or by the breaking of time reversal symmetry (when the magnetic flux threading the graphene T exceeds one flux quantum $h/2e$). The mean peak-to-peak amplitude of the SS oscillations, measured in the field range $200G < B < 500G$, is shown in Fig. 4.2(c) as a function of V_{BG}. In order to minimize the SS component and to isolate the EA contribution, for each quantity of interest we averaged measurements for 25 different values of V_{BG}, stepping the gate voltage just enough to cause a change in E_F larger than the correlation energy $\pi^2 E_T$ [31]. A plot of $E_T = \hbar D/L^2$ for positive V_{BG} is shown in Fig. 4.2(d). The diffusion constant D is estimated from the zero-bias conductivity, assuming a linear dispersion for graphene [32, 33] (we take $L = 1\mu m$, corresponding to the distance between the bottom of the T and the superconducting contacts; note how D decreases as the Fermi level approaches charge neutrality, consistently with the expected tendency toward localization).

Figures 4.2(a) and 4.2(d) show the results of the ensemble averaging (performed around $V_{BG} = 50$ and $60V$, respectively) for the magnetic field dependence of the linear conductance and for the bias-dependent differential

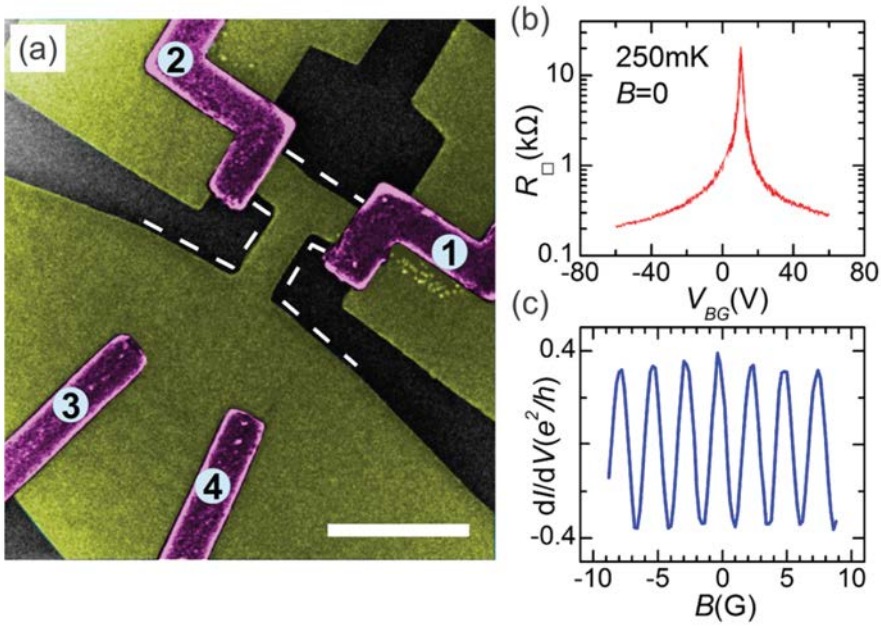

Figure 4.1: (a) False color scanning electron micrograph of one of our devices; graphene and the superconducting electrodes are colored in yellow and purple, respectively (contacts 1 and 2 are joined by $a \simeq 12\mu m^2$ superconducting loop. The scale bar corresponds to $1\mu m$). (b) Resistance per square of the T-shaped graphene ribbon (outlined by dashes) versus V_{BG}. (c) Four-probe conductance $G_{3,2|4,1}$, periodically modulated by the flux threading the loop (measured at $T = 250$ mK with an applied bias $V_{SD} = 40\mu V$).

conductance. Around $B = 0$ the amplitude of the conductance oscillations measured at $V_{SD} = 40\mu eV$ is not much affected by the averaging process, because at this bias the EA contribution is larger than the SS one. On the contrary, at higher magnetic field ($B > 15mT$), where the EA contribution is suppressed, averaging over N traces suppresses the amplitude proportionally to $N^{-1/2}$ [see Fig. 4.2(e)]. Similarly, individual $dI - dV$ curves are asymmetric and exhibit random bias dependent features, whereas the EA curve is symmetric [thick versus thin lines in Fig. 4.2(d)].

Having established the averaging procedure, we look in detail at the EA phase-modulated oscillations at large charge density ($V_{BG} = 60$ V). The low-field conductance oscillations are plotted in Fig. 4.3(a) at $T = 250$ mK, for V_{SD} between 0 and 0.55 mV. Similar measurements have been done as a function of temperature, for $V_{SD} = 0$. The V_{SD} and T dependence of the peak-to-peak amplitude of the first and second harmonic are shown in Figs. 4.3(b)

and 4.3(c). The first harmonic exhibits reentrance in the bias and in the temperature dependence, with the oscillation amplitude having a maximum at an energy (i.e., either bias or temperature) comparable to the Thouless energy [$E_T \approx 45\mu$ eV at $V_{BG} = 60$ V, see Fig. 4.2(d)]. The second harmonic, on the contrary, shows no reentrance. This is expected, because the trajectories causing conductance oscillations with twice the frequency have to Andreev reflect at both superconducting electrodes, and are therefore longer (by approximately twice the distance between the S contacts). The effective Thouless energy associated to these trajectories is therefore significantly smaller than E_T, so that the energy at which reentrance would occur for the second harmonic is smaller than the lowest temperature reached in the experiment [1].

We now analyze the evolution of the energy dependence of the oscillations as a function of V_{BG}. Figure 4.4(a) shows the bias dependence of the EA oscillation amplitude (first harmonic) for seven different values of V_{BG} between 60 and 12.5 V. Upon lowering V_{BG}, the maximum oscillation amplitude decreases, qualitatively in line with the theory, because R_N increases [see Fig. 1(c)]. The value of V_{SD} for which the maximum oscillation amplitude occurs, however, remains essentially unchanged. Within the existing theory, this finding is inconsistent with the value of the Thouless energy E_T, which changes from ~ 45 to $\sim 10\mu$ eV as V_{BG} is lowered [Fig. 4.2(d)]. For a more quantitative analysis, we look at the data in terms of normalized quantities, i.e., plotting $R_N \delta G$ versus eV_{SD}/E_T [Fig. 4.4(b)]. At large densities, for $V_{BG} = 60$, 50, and 40 V, the rescaled curves fall on top of each other, as expected. When lowering V_{BG} below 30 V, however, deviations from perfect scaling become progressively larger: the maximum relative oscillation amplitude decreases, and shifts to larger eV_{SD}/E_T ratios. Both trends observed in the range $12.5\text{V} < V_{BG} < 30$ V are in conflict with what is predicted by existing theory.

The suppression in the amplitude of the Andreev oscillations and the shift of their maximum toward higher energy can be explained by a progressive shortening of L_ϕ. A finite value of the phase-breaking length, which is taken to be infinite in the simplest theory, introduces a cutoff for the penetration of the pair amplitude in N. When L_ϕ drops below the size of the device L,

[1] Our measurements far from charge neutrality reproduce what was found in 2DEG-based interferometers [19],[20],[21], having dimensions, a diffusion constant, and carrier density comparable to those of our graphene devices at $V_{BG} = 60V$. This observation indicates that the Dirac nature of electrons does not play an important role in disordered graphene on SiO_2 (see also X. Du *et al.* in [40]). Indeed, possibly the only theoretically predicted manifestation of the Dirac nature of carriers on proximity effect in graphene is the so-called specular Andreev reflection [43], which requires extremely clean samples, to be able to gate tune the Fermi energy near the charge neutrality point on a scale of the superconducting gap ($\simeq 0.5$ meV). This regime is not relevant here, since for graphene on SiO_2 potential fluctuations are approximately two orders of magnitude larger.

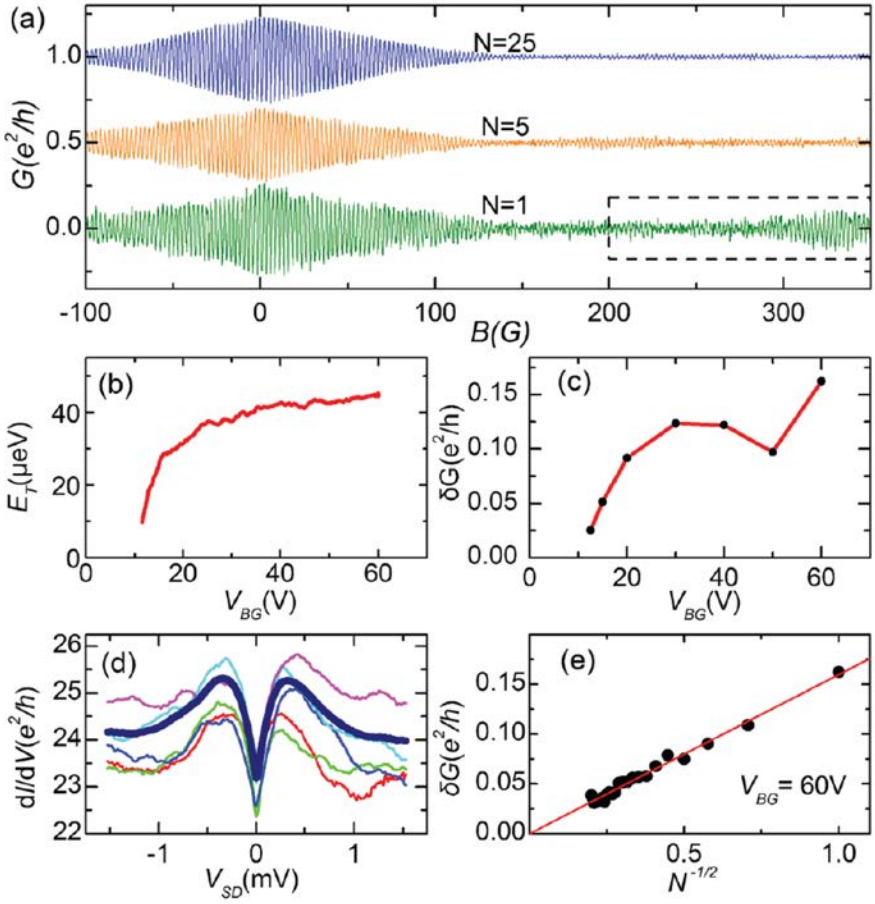

Figure 4.2: (a) Magnetoconductance (background subtracted), averaged over $N = 1, 5$, and 25 V_{BG} values around 50 V ($V_{SD} = 40\mu$V; the curves are offset for clarity). (b) Thouless energy E_T extracted from the V_{BG} dependent resistance of the device. (c) Amplitude of the large-field ($200G < B < 500G$) sample-specific conductance oscillations. (d) Ensemble-averaged (thick line) versus individual dI/dV curves (thin lines) measured around $V_{BG} = 60$ V at $T = 250$ mK. (e) Sample specific oscillation amplitude versus the number of averaged experimental curves.

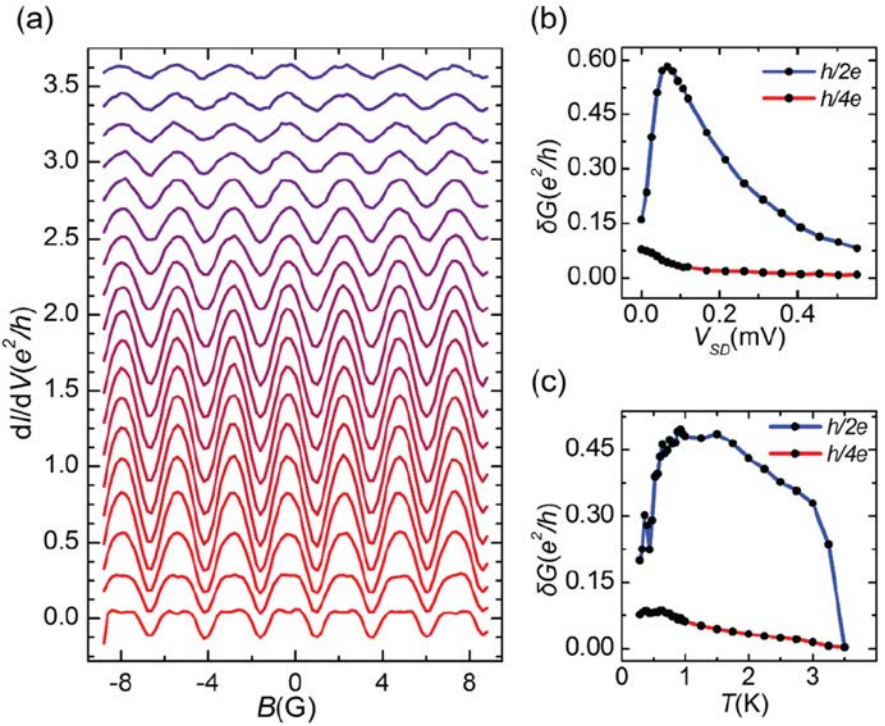

Figure 4.3: (a) EA conductance oscillations at $V_{BG} = 60$ V and $T = 250$ mK, for V_{SD} varying from 0 (bottom curve) to 0.5 mV (top; curves offset for clarity). (b) Bias dependence of the amplitude of the first and second harmonics of the oscillations shown in (a). (c) Temperature dependence of the harmonics of the zero-bias EA oscillations.

$E_\phi = \hbar D/L_\phi^2$ takes the role of E_T in determining the energy-scale of the reentrance. Having a new energy scale (next to E_T) explains the deviations from scaling on the energy axis. Dephasing obviously also explains why the amplitude of the proximity effect decreases, since trajectories with a length larger than L_ϕ cannot contribute to phase coherent effects. For a very closely related problem, namely how a reduction in L_ϕ affects the RE in the conductance of a single NS junction, a quantitative analysis has been performed by Charlat et al. [15, 16], using linearized Usadel equations in which a finite value of L_ϕ was introduced phenomenologically. The result is illustrated in the inset of Fig. 4.4(b), which shows the bias dependent linear conductance for five different values of the phase coherence length. At a qualitative level the evolution of the energy dependence reproduces the behavior of the Andreev conductance oscillations measured in our experiments for different values of V_{BG}, supporting the idea that the behavior of the Andreev oscillations at low

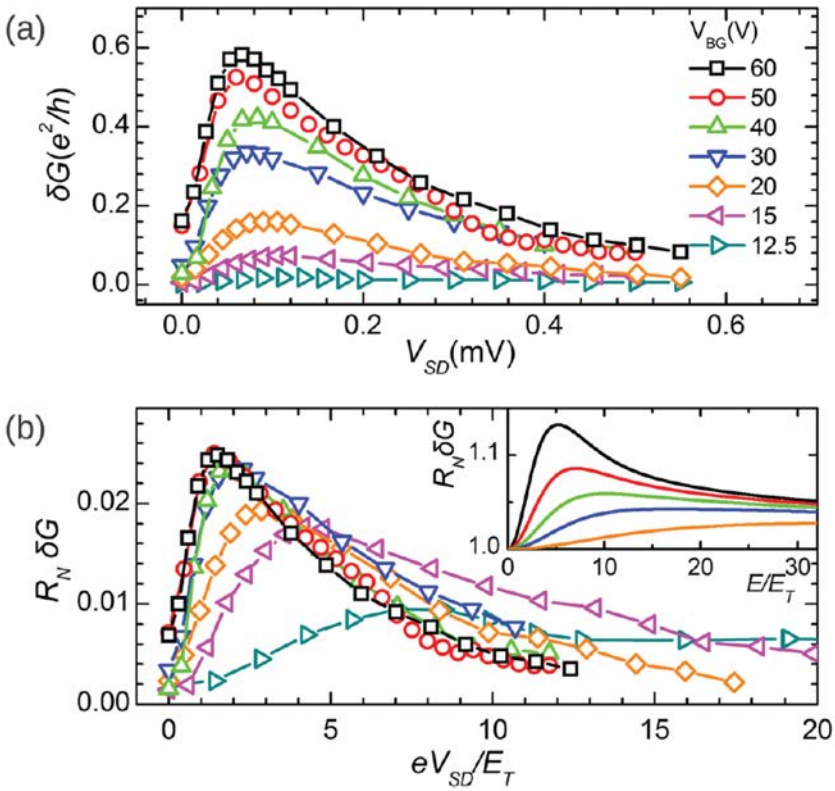

Figure 4.4: (a) Bias-dependent amplitude of the EA oscillations (first harmonic) for -10 G $< B <$ 10 G, measured at $T = 250$ mK and 12.5 V $< V_{BG} <$ 60 V. (b) Same data as in (a), plotted in dimensionless units: the curves measured for $V_{BG} = 60, 50,$ and 40 V exhibit a perfect scaling, which breaks down starting from $V_{BG} = 30$ V. Inset: calculated conductance of a diffusive NS junction for decreasing values of $L_\phi = L$ (∞, black curve, 0.6, 0.4, 0.3, 0.2, orange curve), using the linearized Usadel equations, as in Ref. [15, 16].

carrier density is governed by the shortening of L_ϕ. Our devices, therefore, allow the continuous tuning between two regimes, with induced superconductivity being suppressed by thermal fluctuations at high gate voltage, and by electron dephasing at low gate voltage, with dephasing eventually completely suppressing the superconducting correlations.

As for the origin of dephasing, definite conclusions cannot be drawn at the moment. The progressive increase of the influence of EEI as VBG approaches the charge neutrality point, is a possible explanation. Evidence for

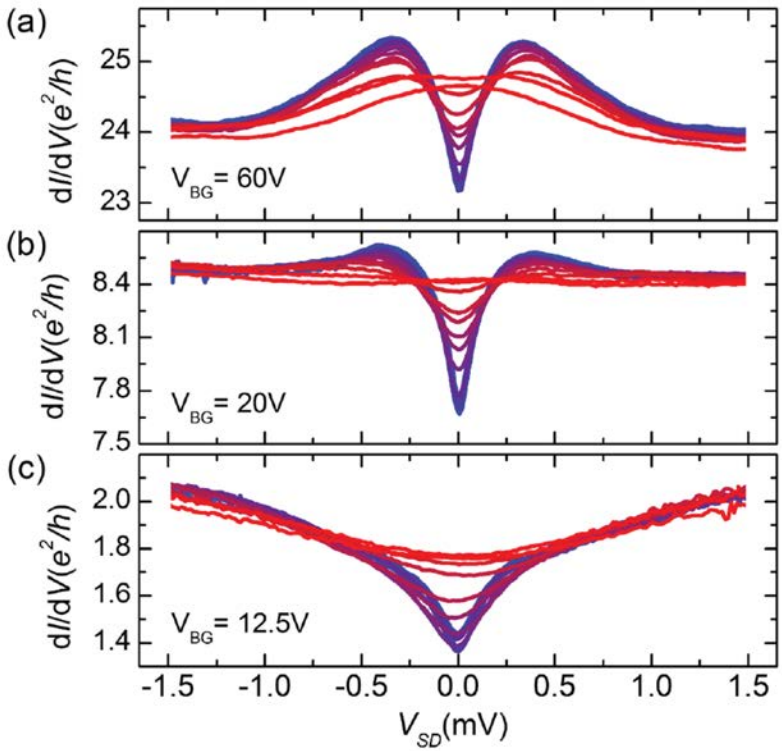

Figure 4.5: (a)–(c) Ensemble-averaged dI/dV curves between 265 mK (blue) and 3.5 K (red), for different values of V_{BG} (60, 20, and 12.5 V, respectively). With approaching charge neutrality, the conductance enhancement due to Andreev reflection visible in (a) is suppressed (b), and eventually completely disappears (c).

such a scenario is provided by the evolution as a function of V_{BG} of the bias-dependent differential conductance $dI/dV(V_{SD})$, shown in Figs. 4.5(a)-(c). At $V_{BG} = 60$ V (top panel) Andreev reflection results in a clear conductance increase. At higher temperature (3.5 K) the conductance enhancement extends to all subgap voltages while at low T a conductance dip appears at low bias (i.e., the phenomenology of the RE). Upon lowering V_{BG} to 20 V [Fig. 4.5(b)], the conductance enhancement at subgap voltage becomes significantly less pronounced; eventually, for V_{BG} sufficiently close to charge neutrality [$V_{BG} = 12.5$ V, Fig. 4.5(c)] no enhancement of $dI/dV(V_{SD})$ is observed, and only a suppression persists, which occurs on an energy scale larger than the superconducting gap. This suppression is what is typically seen in low-dimensional systems where dynamical Coulomb blockade becomes relevant [34, 35, 36, 37]. Dephasing, however, may also have a different origin.

Indeed, earlier weak-localization measurements in large graphene flakes [38] have revealed an unexpected saturation of the dephasing time τ_ϕ. at low temperatures, a behavior that is not yet understood and that appears incompatible with the sole effect of EEI. More experiments are needed, and possibly, the study of the PE may provide a useful tool to understand what limits τ_ϕ in graphene.

4.4 Conclusion

In conclusion, we have used graphene-based Andreev interferometers to investigate and control the influence of microscopic dephasing on induced superconductivity. Our results show how the possibility to gate-tune normal transport in graphene is particularly effective to investigate unexplored regimes of the superconducting proximity effect [[3, 4],[39, 40, 41]].

4.5 Bibliography

[1] P. G. de Gennes. *Superconductivity of Metals and Alloys*. Advanced Book Classics, 1999.

[2] K. Maki. In R. D. Parks, editor, *Superconductivity*, chapter 18, pages 1035–1105. Dekker, 1969.

[3] Adrien Allain, Zheng Han, and Vincent Bouchiat. Electrical control of the superconducting-to-insulating transition in graphene–metal hybrids. *Nat Mater*, 11(7):590–594, July 2012.

[4] L. Serrier-Garcia, J. C. Cuevas, T. Cren, C. Brun, V. Cherkez, F. Debontridder, D. Fokin, F. S. Bergeret, and D. Roditchev. Scanning tunneling spectroscopy study of the proximity effect in a disordered two-dimensional metal. *Phys. Rev. Lett.*, 110:157003, Apr 2013.

[5] H. Pothier, S. Guéron, D. Esteve, and M. H. Devoret. Flux-modulated Andreev current caused by electronic interference. *Phys. Rev. Lett.*, 73:2488–2491, Oct 1994.

[6] A. Dimoulas, J. P. Heida, B. J. v. Wees, T. M. Klapwijk, W. v. d. Graaf, and G. Borghs. Phase-dependent resistance in a superconductor-two-dimensional-electron-gas quasiparticle interferometer. *Phys. Rev. Lett.*, 74:602–605, Jan 1995.

[7] V. T. Petrashov, V. N. Antonov, P. Delsing, and T. Claeson. Phase controlled conductance of mesoscopic structures with superconducting "mirrors". *Phys. Rev. Lett.*, 74:5268–5271, Jun 1995.

[8] S.N. Artemenko, A.F. Volkov, and A.V. Zaitsev. On the excess current in microbridges s-c-s and s-c-n. *Solid State Communications*, 30(12):771 – 773, 1979.

[9] C. W. J. Beenakker. Quantum transport in semiconductor-superconductor microjunctions. *Phys. Rev. B*, 46:12841–12844, Nov 1992.

[10] C. J. Lambert and R. Raimondi. Phase-coherent transport in hybrid superconducting nanostructures. *J. Phys. Condens. Matter*, 10(5):901, 1998.

[11] A. Ossipov, M. Titov, and C. W. J. Beenakker. Reentrance effect in a graphene n-p-n junction coupled to a superconductor. *Phys. Rev. B*, 75:241401, Jun 2007.

[12] Yuli V. Nazarov and T. H. Stoof. Diffusive conductors as Andreev interferometers. *Phys. Rev. Lett.*, 76:823–826, Jan 1996.

[13] T. H. Stoof and Yu. V. Nazarov. Kinetic-equation approach to diffusive superconducting hybrid devices. *Phys. Rev. B*, 53:14496–14505, Jun 1996.

[14] A Volkov et al. Crossover from mesoscopic to classical proximity effects, induced by particle - hole symmetry breaking in Andreev interferometers. *J. Phys. Condens. Matter*, 8(4):L45, 1996.

[15] P. Charlat, H. Courtois, Ph. Gandit, D. Mailly, A. F. Volkov, and B. Pannetier. Reentrance of the metallic conductance in a mesoscopic proximity superconductor. *Phys. Rev. Lett.*, 77:4950–4953, Dec 1996.

[16] H. Courtois, P. Charlat, Ph. Gandit, D. Mailly, and B. Pannetier. The spectral conductance of a proximity superconductor and the reentrance effect. *Journal of Low Temperature Physics*, 116(3-4):187–213, 1999.

[17] C.-J. Chien and V. Chandrasekhar. Reentrance effect in normal-metal/superconducting hybrid loops. *Phys. Rev. B*, 60:15356–15363, Dec 1999.

[18] V.T. Petrashov, R.Sh. Shaikhaidarov, P. Delsing, and T. Claeson. Phase-sensitive reentrance into the normal state of mesoscopic sns structures. *Journal of Experimental and Theoretical Physics Letters*, 67(7):513–520, 1998.

[19] S. G. den Hartog, C. M. A. Kapteyn, B. J. van Wees, T. M. Klapwijk, and G. Borghs. Transport in multiterminal normal-superconductor devices:

Reciprocity relations, negative and nonlocal resistances, and reentrance of the proximity effect. *Phys. Rev. Lett.*, 77:4954–4957, Dec 1996.

[20] S. G. den Hartog, C. M. A. Kapteyn, B. J. van Wees, T. M. Klapwijk, W. van der Graaf, and G. Borghs. Sample-specific conductance fluctuations modulated by the superconducting phase. *Phys. Rev. Lett.*, 76:4592–4595, Jun 1996.

[21] S. G. den Hartog, B. J. van Wees, T. M. Klapwijk, Yu. V. Nazarov, and G. Borghs. Reentrant behavior in the superconducting phase-dependent resistance of a disordered two-dimensional electron gas. *Phys. Rev. B*, 56:13738–13741, Dec 1997.

[22] Etsuko Toyoda, Hideaki Takayanagi, and Hayato Nakano. Systematic gate-controlled reentrant conductance of a superconductor-semiconductor two-dimensional electron gas junction. *Phys. Rev. B*, 59:R11653–R11656, May 1999.

[23] Yuanbo Zhang, Yan-Wen Tan, Horst L. Stormer, and Philip Kim. Experimental observation of the quantum Hall effect and Berry's phase in graphene. *Nature*, 438(7065):201–204, November 2005.

[24] K. S. Novoselov, A. K. Geim, S. V. Morozov, D. Jiang, M. I. Katsnelson, I. V. Grigorieva, S. V. Dubonos, and A. A. Firsov. Two-dimensional gas of massless Dirac fermions in graphene. *Nature*, 438(7065):197–200, November 2005.

[25] Melinda Y. Han, Barbaros Özyilmaz, Yuanbo Zhang, and Philip Kim. Energy band-gap engineering of graphene nanoribbons. *Phys. Rev. Lett.*, 98:206805, May 2007.

[26] Xinglan Liu, Jeroen B. Oostinga, Alberto F. Morpurgo, and Lieven M. K. Vandersypen. Electrostatic confinement of electrons in graphene nanoribbons. *Phys. Rev. B*, 80:121407, Sep 2009.

[27] F. Molitor, A. Jacobsen, C. Stampfer, J. Güttinger, T. Ihn, and K. Ensslin. Transport gap in side-gated graphene constrictions. *Phys. Rev. B*, 79:075426, Feb 2009.

[28] Melinda Y. Han, Juliana C. Brant, and Philip Kim. Electron transport in disordered graphene nanoribbons. *Phys. Rev. Lett.*, 104:056801, Feb 2010.

[29] Jeroen B. Oostinga, Benjamin Sacépé, Monica F. Craciun, and Alberto F. Morpurgo. Magnetotransport through graphene nanoribbons. *Phys. Rev. B*, 81:193408, May 2010.

[30] Patrick Gallagher, Kathryn Todd, and David Goldhaber-Gordon. Disorder-induced gap behavior in graphene nanoribbons. *Phys. Rev. B*, 81:115409, Mar 2010.

[31] P. A. Lee and A. Douglas Stone. Universal conductance fluctuations in metals. *Phys. Rev. Lett.*, 55:1622–1625, Oct 1985.

[32] Nikolaos Tombros, Csaba Jozsa, Mihaita Popinciuc, Harry T. Jonkman, and Bart J. van Wees. Electronic spin transport and spin precession in single graphene layers at room temperature. *Nature*, 448(7153):571–574, August 2007.

[33] Saverio Russo, Jeroen B. Oostinga, Dominique Wehenkel, Hubert B. Heersche, Samira Shams Sobhani, Lieven M. K. Vandersypen, and Alberto F. Morpurgo. Observation of Aharonov-Bohm conductance oscillations in a graphene ring. *Phys. Rev. B*, 77:085413, Feb 2008.

[34] R. Egger and A. O. Gogolin. Bulk and boundary zero-bias anomaly in multiwall carbon nanotubes. *Phys. Rev. Lett.*, 87:066401, Jul 2001.

[35] A. Bachtold, M. de Jonge, K. Grove-Rasmussen, P. L. McEuen, M. Buitelaar, and C. Schönenberger. Suppression of tunneling into multiwall carbon nanotubes. *Phys. Rev. Lett.*, 87:166801, Oct 2001.

[36] A. Kanda et al. Gate-voltage dependence of zero-bias anomalies in multiwall carbon nanotubes. *Phys. Rev. Lett.*, 92:036801, Jan 2004.

[37] Y. V. Nazarov and Y. M. Blanter. *Quantum Transport*. Cambridge University Press, 2009.

[38] F. V. Tikhonenko, D. W. Horsell, R. V. Gorbachev, and A. K. Savchenko. Weak localization in graphene flakes. *Phys. Rev. Lett.*, 100:056802, Feb 2008.

[39] Hubert B. Heersche, Pablo Jarillo-Herrero, Jeroen B. Oostinga, Lieven M. K. Vandersypen, and Alberto F. Morpurgo. Bipolar supercurrent in graphene. *Nature*, 446(7131):56–59, March 2007.

[40] Xu Du, Ivan Skachko, and Eva Y. Andrei. Josephson current and multiple Andreev reflections in graphene sns junctions. *Phys. Rev. B*, 77:184507, May 2008.

[41] Travis Dirks, Taylor L. Hughes, Siddhartha Lal, Bruno Uchoa, Yung-Fu Chen, Cesar Chialvo, Paul M. Goldbart, and Nadya Mason. Transport through Andreev bound states in a graphene quantum dot. *Nat Phys*, 7(5):386–390, May 2011.

[42] K. Flensberg, J. Bindslev Hansen, and M. Octavio. Subharmonic energy-gap structure in superconducting weak links. *Phys. Rev. B*, 38:8707–8711, Nov 1988.

[43] C. W. J. Beenakker. Specular Andreev reflection in graphene. *Phys. Rev. Lett.*, 97:067007, Aug 2006.

Chapter 5

Detection of the Josephson supercurrent carried by Andreev resonances at $E > \Delta$

We report a study of how electronic states at different energy contribute to the supercurrent in superconductor-normal metal-superconductor (SNS) Josephson junctions. The experiments rely on multi-terminal devices with graphene used as normal conductor, and provide experimental control over the electronic distribution in the junction, by acting on which we progressively suppress the supercurrent. We analyze the data in terms of a one-dimensional model, and find that the evolution of the critical current that is observed experimentally is consistent with a "two-step" electronic distribution, as expected from the characterization of the transport regime of our devices. We also show that an analysis based on the same model, under the assumption that electron relaxation is sufficiently strong to generate an electronic distribution with an effective temperature, does not lead to a satisfactory agreement with the data. Within the context of this analysis, our measurements provide spectroscopic information about the supercurrent carrying density of states. We conclude that the critical current remains finite, even when the contribution to the supercurrent of Andreev bound states with energy smaller than the superconducting gap is entirely suppressed. This remaining finite critical current is due to the contribution to the supercurrent of Andreev resonances at energies above the gap, whose role in SNS Josephson junctions was first predicted long ago by Kulik.

5.1 Introduction

Our microscopic understanding of supercurrent in Josephson junctions (JJs) is based on the concept of Andreev bound states, which are formed by a coherent superposition of electron and hole waves, and "live" at energies smaller than the superconducting gap Δ [1, 2]. These states, confined by Andreev reflection in the region between the two superconducting electrodes, mediate Cooper pair transfer between them, and fully account for the properties of the supercurrent in many types of JJs [3]. In some cases, however, states at energy $E > \Delta$ cannot be neglected, because Andreev reflection [4] can occur with finite probability at E well above Δ and cause the formation of scattering resonances, which also contribute to the supercurrent flow [1, 2]. The existence and properties of these Andreev resonances were predicted theoretically by Kulik already in 1970, in his seminal analysis of supercurrent through superconductor-normal metal-superconductor (SNS) JJs, i.e., the same paper where Andreev bound states were originally described [1]. Whereas, by now, experiments have led to the observation of Andreev bound states at $E < \Delta$ [5, 6, 7, 8] and confirmed their relation to the supercurrent, no experimental study has been attempted to detect the contribution of states at $E > \Delta$ to the Josephson supercurrent of a SNS junction. Here, we use multi-terminal graphene-based SNS JJs to present experimental evidence indicating that these states do in fact give a significant contribution to the critical current.

Determining the contribution of states at different energies to the Josephson supercurrent requires a suitable form of spectroscopy. A strategy analogous to that commonly used for normal transport (measuring transport while applying a bias eV across the device) cannot work, since the supercurrent is –by definition– the current flowing at $V = 0$. Spectroscopy can be performed by monitoring the change in supercurrent induced by a known modification in the occupation probability of the electronic states at energy E [9]. In our experiments, we employ multi-terminal SNS JJs [10, 11, 12] with two additional normal contacts connected to the N region (see Fig. 5.1b); we refer to these two additional contacts as to the "control line") that enable this strategy to be implemented in practice.

To understand the idea, recall the generic expression for the supercurrent I_s in a SNS JJ, $I_s = \int_{-\infty}^{\infty} J_s(E,\phi)[1 - 2f(E)]\,\mathrm{d}E$ ($J_s(E,\phi)$ is the supercurrent carrying density of states) [13, 14, 15]. $f(E)$ is the electron distribution: in equilibrium it corresponds to the Fermi-Dirac function, but –if interaction between electrons can be neglected– the application of a "control" voltage V_{cnt} across the control line generates a two-step non-equilibrium distribution $f^*(E)$ (see Fig. 5.1b [16]. $f^*(E) = 1/2$ in an energy range of $\pm eV_{cnt}/2$ around the Fermi energy E_F, fully suppressing the contribution of these states

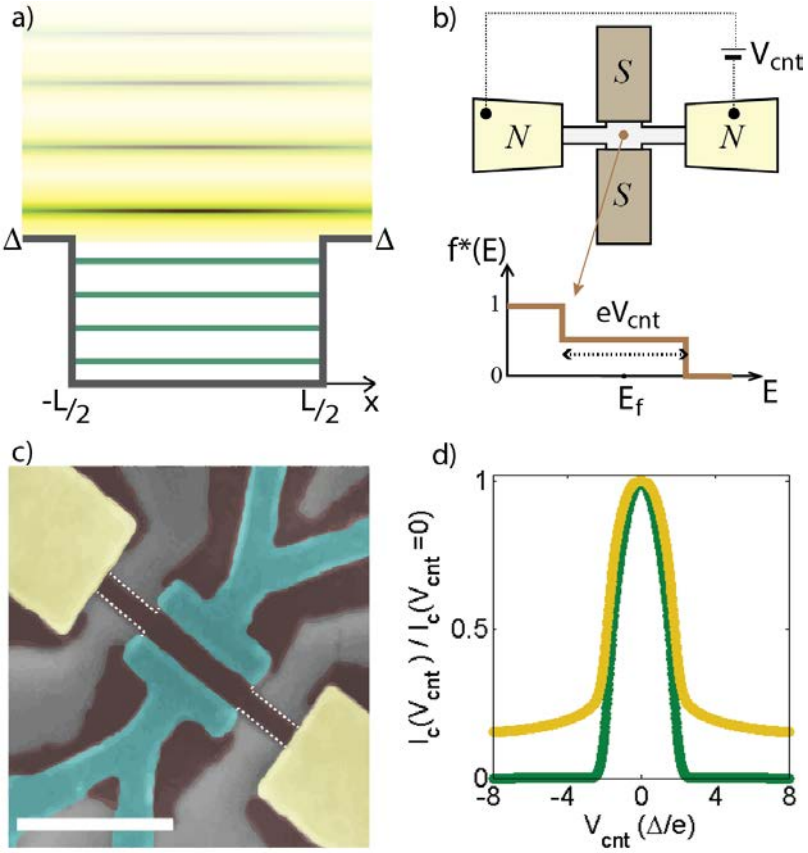

Figure 5.1: (a) States involved in the supercurrent transport of a SNS Josephson junction: discrete Andreev bound states at sub-gap energy, confined in the N region by the superconducting gap, and broadened resonances (quasi-bound states) extending in the superconducting electrodes at $E > \Delta$. (b) Schematics of the multi-terminal SNS junctions used in this work, with a sketch of the distribution function induced by a finite control voltage V_{cnt}. (c) Scanning electron micrograph of an actual device. The S electrodes are blue colored, the normal electrodes are yellow, and graphene is dark grey. The dotted line delimits the control line (the scale bar is 1 μm long). (d) Normalized I_c as a function of V_{cnt} for a $L = 300nm$ junction calculated theoretically with the one-dimensional model of Ref. [13], using the distribution function shown in panel (b) (see also discussion at the end of the paper). The green line is the result obtained by removing the contribution of states at $E > \Delta$; the yellow line includes also the contribution of states at $E > \Delta$. Note how, in the first case but not in the second, I_c is fully suppressed for $V_{cnt} > 2\Delta/e$.

to I_s [1]. To check experimentally whether states at $E > \Delta$ contribute to the supercurrent, therefore, is conceptually straightforward: it is sufficient to increase V_{cnt} past $2\Delta/e$ and measure whether a supercurrent can continue to flow. Fig. 5.1d illustrates this point, by showing the dependence of the critical current I_c as a function of V_{cnt} expected from a one-dimensional theoretical model (see Ref. [13] and discussion at the end) when states at $E > \Delta$ do, or do not, contribute to the supercurrent.

Past work on metal film devices shows that the ideas just outlined are sound. In particular, the Saclay group [16, 17, 18] analyzed in detail the conditions under which the non-equilibrium distribution function generated by applying a voltage across a metal strip (the control line, in the multi-terminal SNS devices that we consider here) corresponds to the one expected for non-interacting electrons. It was shown that the two-step function is a good approximation as long as the length of the control line is smaller than, or comparable to, the electronic phase coherence length L_ϕ [16, 17, 18]. This is so, because it is the same inelastic processes that cause electronic decoherence that also cause the two-step distribution function to relax to a Fermi-Dirac distribution with an effective temperature when $L \gg L_\phi$. In parallel work, Baselmans *et al.* [19] demonstrated the principle of supercurrent spectroscopy outlined above, by showing experimentally that in SNS junctions states at different energies carry supercurrent in opposite directions, which is the theoretically expected behavior if the Thouless energy of the N region $E_{Th} \ll \Delta$ [15, 14] (in those experiments $E_{Th} \simeq 140\mu$eV $\ll \Delta = 1.5$ meV, and the supercurrent was seen to vanish already when $V_{cnt} \simeq \Delta/e$, i.e., for $V_{cnt} > 2\Delta/e$ no supercurrent was measured).

5.2 Multi-terminal S/G/S JJ

For the realization of multi-terminal SNS devices, we use monolayer graphene as a normal conductor (see Fig. 5.1c; [2]). As compared to common metal films, graphene has a much smaller density of states and a much larger resistance, two factors that contribute to the elimination of undesired effects of non-equilibrium on the superconducting electrodes (such as inverse proximity effect and charge imbalance [20], which can strongly affect the gap in the superconducting electrodes). The sizable mean free path of electrons in graphene –typically of the order of 100 nm away from the charge neutrality point, for graphene on SiO_2– leads to larger values for the Thouless

[1] $J_s(E, \phi)$ is antisymmetric in E, and so perturbation to $f^*(E)$ that are symmetric in energy do not change the result.

[2] The Dirac nature of electrons in diffusive graphene does not affect much the phenomenology of the superconducting proximity effect, except under very specific circumstances that are not relevant in our devices

energy. This is ideal for our experiments, since we want $E_{Th} \simeq \Delta$ (or larger) to enhance the contribution to the supercurrent from states at $E > \Delta$. A long mean-free path also facilitates the device fabrication, since it results in a longer phase coherence length L_ϕ, which more readily can exceed the length of the control line (as it is needed to achieve a two-step distribution function). Finally, another advantage of graphene is that the carrier density can be gate tuned, which easily allows experiments to be performed and compared for different values of the Fermi energy.

We want to emphasize explicitly that, in order to perform supercurrent spectroscopy, the distribution function in the junction has to have (at least approximately) the "two-step" shape shown in Fig. 5.1b. To ensure that this is the case in our devices we intentionally design the length of the control line to be shorter than the phase coherence length in graphene L_ϕ, as discussed in detail below. To further confirm the energy relaxation processes do not play a dominant role, we also analyze our data in terms of both a "two-step" distribution and of a thermal distribution with an effective temperature (i.e., the distribution function expected for sufficiently strong energy relaxation), and show that only the two-step distribution reproduces the data satisfactorily, with realistic experimental parameters.

The devices (Fig. 5.1c) were fabricated by means of electron-beam lithography, metal evaporation, and lift-off, using exfoliated graphene deposited on a degenerately doped Si substrate (acting as gate) covered with 285 nm thick SiO_2. The superconducting electrodes consist of a Ti/V/Au trilayer ($3.5/11/3.5$ nm; $T_c = 2.2$ K and $\Delta = 340\mu$eV, see below) and the contacts to the control line are formed by a Ti/Au bilayer ($10/70$ nm). To define the junction and the control line, graphene was etched in an oxygen plasma; the separation between the two superconducting electrodes is $\simeq 200$ nm and the control line is $L \simeq 1.5\mu$m long. From the gate voltage dependence of the resistance of the the control line we estimate the elastic scattering time τ and the diffusion constant D of electrons in graphene (see supplementary information). We find that the electron mean-free path is $l \simeq 100$ nm, corresponding to half the separation between the two superconducting electrodes in our junction, and $E_{Th} \approx 300\mu$eV, comparable to Δ. With a mean-free path smaller than –but comparable to– the junction length and the Thouless energy $E_{Th} \simeq \Delta$, superconducting transport in our JJ, although diffusive, is not far from the ballistic limit. We note that this regime, half way between fully diffusive and ballistic, is rather different from that characteristically realized in conventional metallic SNS JJs studied in the past. There the mean-free path is typically much smaller than the separation between the superconducting electrodes, and the Thouless energy is between one and two orders of magnitude smaller than the superconducting gap. Finally, and importantly, with the value of the diffusion constant extracted from the device characterization,

we obtain $L_\phi = \sqrt{D\tau_\phi} \approx 2\mu m$, which is longer than the control line. This conclusion is reached by using $\tau_\phi \approx 100$ ps at $T = 250$ mK, as found in different literature reports [21, 22, 23], which is a conservative estimate for the temperature and gate voltage range in which our experiments are performed. All measurements presented here were performed in a Helium-3 system at $T = 250$ mK.

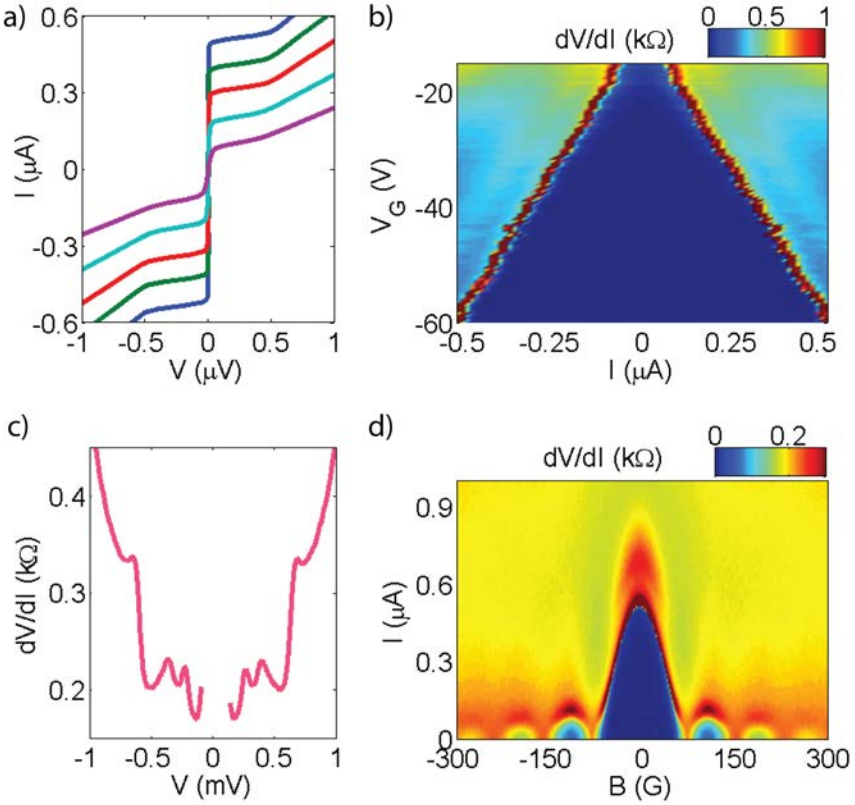

Figure 5.2: (a) I-V curves of the SNS junction at $V_{cnt} = 0$ V, measured for V_G between -60 V (blue) and -20 V (purple), in -10 V steps. (b) Color plot of the differential resistance dV/dI as a function of a current bias I and V_G (dark blue corresponds to $I < I_c$). (c) dV/dI as a function of bias voltage V across the junction, measured at $V_G = -60V$, exhibiting features due to multiple-Andreev reflections. (d) dV/dI as a function of current bias and perpendicular magnetic field, exhibiting a clear Fraunhofer pattern. All data were taken at $T = 250$ mK.

We start by characterizing the superconducting transport properties of our JJ at $V_{cnt} = 0$. Fig. 5.2a shows the $I - V$ curves measured for different gate

voltages V_G, ranging from -60 to -20 V. Supercurrent is observed throughout this range, with the critical current I_c decreasing as V_G approaches the charge neutrality point (at $V_G \approx 0$ V) [24]. At $V_G = -60$ V, $I_c R_n = 140\mu$V (R_n is the JJ normal state resistance), is comparable to what is expected from existing theory for diffusive SNS junctions which predicts $I_c R_n = \arctan(E_{Th}/2\Delta)\Delta/e$ [25, 26] (Δ is measured from the differential resistance of the JJ as explained here below), and only a factor of 3-4 different from what is predicted for a ballistic graphene junction ($R_n I_c = 2.44\Delta/e$) [27]. Finding a $R_n I_c$ product that is comparable to that expected for both the diffusive and the ballistic regimes is due to the fact that the separation between the superconducting electrodes is only slightly longer –a factor of 2, or even slightly less– than the electron mean-free path. This observation confirms the remark that we made just above, namely that transport from one superconductor to the other in our devices occur in a regime that differs from that of fully diffusive metal-based JJs studied in the past, in which $E_{Th} \ll \Delta$. For those JJs the mean free path is typically much smaller than the separation between the superconducting contacts, and the $I_c R_n$ product is correspondingly one-to-two orders of magnitude smaller than what is expected for ballistic transport. In those metal-based JJs –but not in our graphene JJs– there is therefore a net separation between the diffusive and the ballistic transport regime. We will refer to these considerations later on, when we choose the theoretical model to describe superconducting transport, that we use to analyze the data quantitatively.

Fig.5.2c further shows that the differential resistance dV/dI as a function of applied bias V measured at $V_G = -60$ V exhibits a sharp and large drop upon decreasing V across $2\Delta/e$, as well as clear subgap structure at $V = 2\Delta/N$ (with N an integer) due to multiple Andreev reflection processes. From these measurements we obtain the value of the superconducting gap in our devices ($\Delta = 340\mu$eV), as well as the transparency of the S/graphene interface, which we find to be $T_{int} \simeq 0.85$ (note that the electrodes used to contact the control line have the same quality, since also in that case –just like for the superconducting electrodes– the interface with graphene is made of Titanium). Finally, upon the application of a perpendicular magnetic field, I_c exhibits a clear Fraunhofer pattern (Fig. 5.2d) whose period agrees with the one expected from the device geometry, indicating a good uniformity of the supercurrent density across the junction [24, 26].

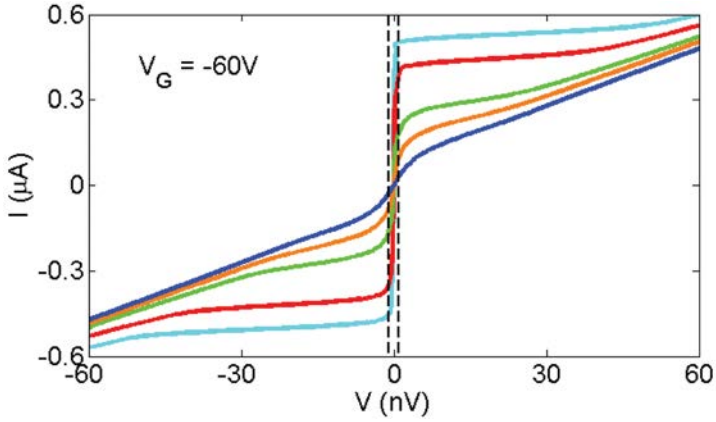

Figure 5.3: I-V curves measured at $V_G = -60V$ and $T = 250$ mK, for $V_{cnt} = 0$ (light blue), Δ/e (red), $2\Delta/e$ (green), $3\Delta/e$ (orange) and $5\Delta/e$ (dark blue). Upon increasing V_{cnt} the critical current is suppressed, but even at the largest value of V_c, a finite supercurrent continues to flow. The dashed lines indicate the 1 nV threshold used to determine I_c quantitatively (using a 2 nV threshold leads to conceptually identical results).

5.3 Controllable supercurrent: measurements and analysis

Having characterized the transport properties of our JJ, we now look at how the control voltage V_{cnt} affects the critical current for a fixed value of V_G. Fig. 5.3 shows the junction $I - V$ curves measured (at $V_G = -60$ V, $T = 250$ mK) for V_{cnt} ranging from 0 to $5\Delta/e$. A finite supercurrent is always present, albeit a small finite resistance appears on the superconducting branch of the $I - V$ curve at the largest V_{cnt} values (as commonly done, I_c is defined as the current for which a predefined threshold voltage is reached. We fix 1 nV as threshold, corresponding to the vertical lines in Fig. 5.3. We conclude directly from the data that the critical current remains finite even when V_{cnt} is (at least) as large as $5\Delta/e$, i.e. for values much larger than $2\Delta/e$ above which –for a two-step distribution function (Fig. 5.1b)– the contribution of subgap Andreev bound states is completely suppressed. An identical conclusion is reached if we analyze the evolution of the differential resistance as a function of current (dV/dI-vs-I) with increasing V_{cnt} (see the color plot in Fig. 5.4, and its "cuts" at individual values of V_{cnt}). A truly zero resistance state is observed for $V_{cnt} > 3\Delta/e$, and even at $V_{cnt} = 5\Delta/e$ the finite resistance (approximately 30Ω) that is observed at small currents corresponds to less than 10% of the normal state resistance measured at $V > 2\Delta/e$, $R_n \simeq 400\Omega$

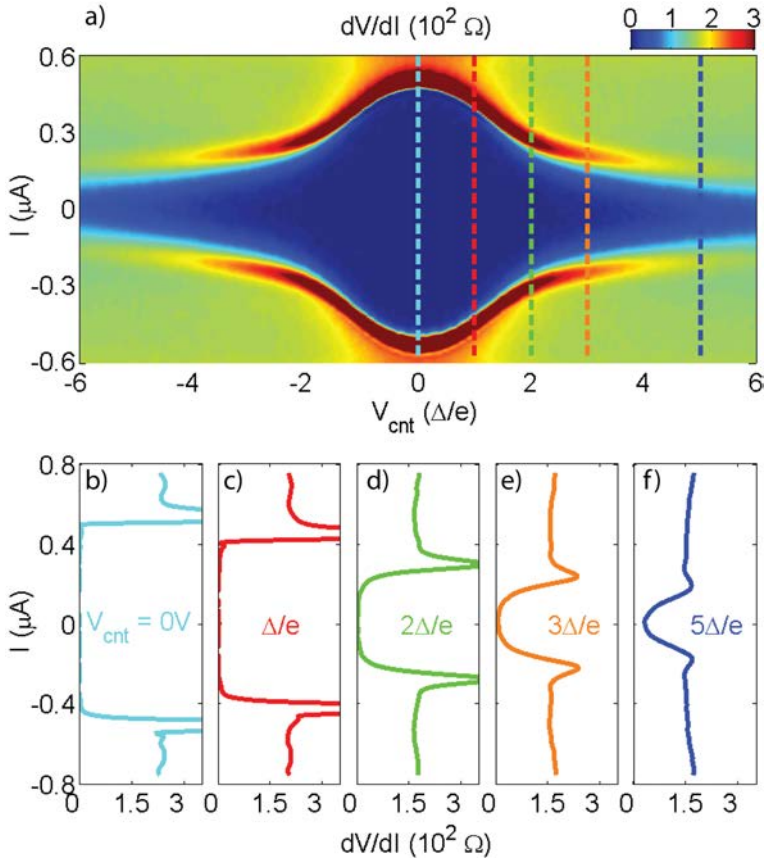

Figure 5.4: Differential resistance measured at $V_G = -60$ V and $250mK$, as a function of V_{cnt} and I. The dashed lines indicate the values of V_{cnt} for which the data in panels (b-f) are plotted. A finite critical current is visible throughout the V_{cnt} range explored, even for V_{cnt} significantly larger than $2\Delta/e$, i.e. the value of V_{cnt} needed to fully suppress the contribution of Andreev bound states at $E < \Delta$.

(see Fig. 5.2c). It is apparent from the color plot in Fig. 5.4a that a finite critical current remains visible up to the highest value of V_{cnt} shown, $6\Delta/e$.

The dependence of I_c on V_{cnt} for V_G between $-60V$ and $-30V$ is illustrated in Fig. 5.5, through the plot of $I_c(V_{cnt})/I_c(V_{cnt} = 0)$ (for values of V_G closer to the charge neutrality point, I_c becomes too small to perform accurate systematic measurements as a function of V_{cnt}). Once scaled to the critical current measured at $V_{cnt} = 0$, all data tend to fall on top of each other. $I_c(V_{cnt})/I_c(V_{cnt} = 0)$ decreases steeply for $|V_{cnt}| < 2\Delta/e$ and more slowly

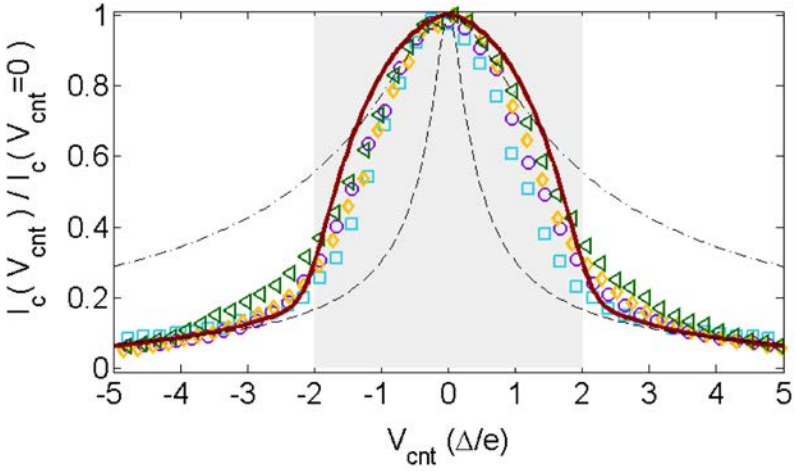

Figure 5.5: Normalized critical current at $T = 250$ mK, with different symbols representing measurements taken at different gate voltages: $V_G = -60$ V (triangles), -50 V (diamonds), -40 V (circles), -30 V (squares). I_c was determined using a 1 nV threshold for the voltage, but the key aspects of our results do not depend on the precise value of the threshold (see supplementary information). Two different regimes are visible: for $|V_{cnt}| < 2\Delta/e$, I_c decreases rapidly upon increasing V_{cnt}; for $|V_{cnt}| > 2\Delta/e$, I_c remains non-zero and decreases less rapidly, as expected when the continuum quasi-bound states contribute to the supercurrent. The thick red line represents a theoretical calculation obtained for the two-step distribution function, and reproduces the data rather satisfactorily (in the theoretical curve, the crossover between the two regimes occurs just above $|V_{cnt}| > 2\Delta/e$, because of the finite T). The thin black lines are theoretical curves calculated with the Fermi-Dirac distribution for different effective temperatures T^* obtained from the relation $T^* = \sqrt{T^2 + (aV_{cnt})^2}$ with $a = 3.2$ K/mV as expected for the case of strong electron-electron interactions (dashed-dotted line) and $a = 15$ K/mV (dashed line) as it is needed to reproduce the data at large V_{cnt}. The results show that irrespective of the value of a the assumption of an electronic distribution with an effective temperature described by T^* cannot reproduce the data well through the entire V_{cnt} range.

$|V_{cnt}| > 2\Delta/e$, which provides an indication of a crossover in the behavior of the supercurrent at an electron energy $E = eV_{cnt}/2 = \Delta$. The critical current remains finite for V_{cnt} well above $2\Delta/e$ for all values of V_G in the range between $-60V$ and $-30V$. Again, under the assumption that a two-step distribution function correctly describes the non-equilibrium electronic population at finite V_{cnt} values, this observation is a direct manifestation of the contribution of states with $E > \Delta$ to the supercurrent flow.

We now proceed to the analysis of the results. As discussed above, having the phase coherence length L_ϕ larger than the length of the control line L im-

plies that inelastic scattering processes are not sufficiently strong to cause thermalization of the non-equilibrium distribution induced by the control voltage. It follows that the shape of the electronic distribution in the junction is of the "two-step" type shown in Fig. 5.1b. Nevertheless, we also analyze the measured dependence of the critical current on V_{cnt} (or, more precisely of $I_c(V_{cnt})/I_c(V_{cnt} = 0)$), by considering the possibility that the electronic distribution is of the Fermi-Dirac type with an effective temperature $T^* > T$, which is what is expected in the presence of strong electron relaxation (i.e., what should be expected if the length of the control line $L \gg L_\phi$). As we will show, there is a significant difference between the theoretically predicted dependence of $I_c(V_{cnt})/I_c(V_{cnt} = 0)$ for a two-step distribution and a Fermi-Dirac distribution with an effective temperature, and only the "two-step" distribution function leads to a satisfactory agreement with the data.

To compute $I_c(V_{cnt})/I_c(V_{cnt} = 0)$ given a certain distribution function, we need to select an appropriate expression for the superconducting carrying density of states. This amounts to selecting the most appropriate theoretical model to describe the supercurrent flowing between the two superconudcting electrode, enabling actual calculations to be done. Since –as we discussed in detail above– our JJs are in between the ballistic and the fully diffusive regime, one should decide what limit is most appropriate for a quantitative description. The expression for the supercurrent carrying density of states of a diffusive SNS junction was given by Wilhelm, Schön, and Zaikin[14], who developed the theory using Keldish-Usadel formalism, having in mind metal-based JJs in which $E_{Th} \ll \Delta$. In that regime, theory shows that a "minigap" $E_g \simeq 3.2E_{Th}$ opens at the Fermi level, and that there are no states in that energy range that can contribute to the supercurrent flow. This implies that the fully diffusive regime is inappropriate for our graphene devices in which $E_{Th} = \Delta$, since –if taken at face value– theory would imply that the "minigap" is 3.2 times larger than Δ (and that there are no states throughout this energy range), which is obviously unphysical. The only other possibility to analyze quantitatively the data based on existing theoretical descriptions is to use a ballistic model for superconducting transport. Since the separation between the superconducting electrodes is (not even) two times longer than the mean-free path, and $E_{Th} = \Delta$, such a ballistic model, albeit not perfect, seems to be fully reasonable approximation (of course, how satisfactory this approximation really is should be judged a posteriori, by looking at the comparison between theory and experiments).

The one-dimensional ballistic model that we use corresponds to the case described in the paper of Bagwell [13], and includes the contribution to the supercurrent due to discrete Andreev bound states at $E < \Delta$, as well as that of the continuum of states at $E > \Delta$. We assume for simplicity transmission at the superconducting interfaces T_{int} to be perfect, since we have estimated

that $T_{int} \simeq 0.85$. We first discuss the case in which the electronic distribution in the JJ $f^*(E)$ is of the two-step type [28]. In practice, we insert $f^*(E)$ in Eqs. (10), (11), and (12) of Ref. [13], in place of the equilibrium Fermi-Dirac distribution (this is also how we obtained the curves shown in Fig. 5.1d). The result is shown by the continuous red line in Fig. 5.5, in which the finite critical current visible for $V_{cnt} > 2\Delta/e$ originates entirely from the continuum contribution at $E > \Delta$, i.e. from Andreev resonances. The theoretical curve reproduces the trends observed experimentally rather satisfactorily. In particular, the critical current is rapidly suppressed at small V_{cnt} and much more slowly for $V_{cnt} > 2\Delta/e$. The order of magnitude of the effect –i.e., of the critical current measured for $V_{cnt} > 2\Delta/e$– is also reproduced with meaningful values of the parameters (the curves are obtained by fixing the length L of the junction, the only parameter that can be varied in the model, to be $L = 300$ nm, somewhat larger than –but comparable to– the actual value). This overall agreement supports the validity of the physical scenario used to interpret our experiments, based on the presence of a two-step distribution function.

Using the same model, we analyze the case in which inelastic scattering between electrons in the control line is strong. In this case, relaxation processes turn the two-step distribution function into a Fermi-Dirac distribution with an effective temperature T^*. If electron-phonon interaction can be neglected (which is certainly the case in graphene on a length scale of many microns, at the temperature of our experiments) and relaxation is due to electron-electron interactions, the effective temperature T^* and the applied voltage V_{cnt} are related by a universal relation $T^* = \sqrt{T^2 + (aV_{cnt})^2}$ with $a = 3.2$ K/mV. Just like for the two-step case, it is straightforward to calculate $I_c(V_{cnt})/I_c(V_{cnt} = 0)$ by inserting the Fermi-Dirac distribution with this effective temperature in Eqs. (10), (11), and (12) of Ref. [13]. The result of the calculations is shown in Fig. 5.5 as a thin dashed-dotted line: it is apparent that the calculations deviate pronouncedly from the data for $V_{cnt} > \Delta/e$. In particular, the critical current does not decrease sufficiently fast at large V_{cnt} and no energy scale is clearly visible in the calculated curve (i.e., there is not a change in behavior of $I_c(V_{cnt})/I_c(V_{cnt} = 0)$ for $V_{cnt} = 2\Delta/e$ as it is visible in the data). It may be argued that for some reason the coefficient a does not have the value expected from theory and a different value needs to be used. To address this possibility, we have calculated $I_c(V_{cnt})/I_c(V_{cnt} = 0)$ using an Fermi-Dirac distribution in which T^* is related to V_{cnt} through different value of a. The results obtained for $a = 15$ K/mV, as it is needed to reproduce the data at large V_{cnt}, are plotted with a thin black dashed line in Fig. 5.5. The result shows that if a is chosen artificially large to make the calculations match the data at large V_{cnt}, the deviations for small V_{cnt} become substantial. This analysis, therefore, shows that a Fermi-Dirac distribution

with $T^* = \sqrt{T^2 + (aV_{cnt})^2}$ cannot reproduce satisfactorily the functional dependence of $I_c(V_{cnt})/I_c(V_{cnt} = 0)$, and even when the parameter a is varied "artificially", the theoretical expression does not reproduce the data, in contrast to the case of the two-step distribution function.

Finally, we note that the data in Fig. 5.5 can also be used to exclude other forms of heating, for the following reason. Specifically, we note that at a fixed value of V_{cnt}, $I_c(V_{cnt})/I_c(V_{cnt} = 0)$ is essentially independent of V_G. This observation is relevant, because when changing V_G from $-60V$ to $-30V$ the resistance of the control line, R_{cnt}, and therefore the dissipated power, $P = V_{cnt}^2/R_{cnt}$, change by a factor of 2 (see supplementary information). Now, if different forms of heating would play a role, the behavior of the critical current should be determined by the dissipated power, and I_c should decrease upon increasing P. It follows that, at any fixed value of V_{cnt}, $I_c(V_{cnt})/I_c(V_{cnt} = 0)$ should then be smallest at $V_G = -60V$, when P is largest. In contrast to this scenario, the data show virtually no dependence on V_G, and, if anything, $I_c(V_{cnt})/I_c(V_{cnt} = 0)$ is slightly larger at $V_G = -60$ V, and not smaller.

5.4 Summary and conclusion

In conclusion, we have performed an analysis of superconducting transport in graphene JJs with an experimentally tunable non-equilibrium distribution functions. This analysis relies on realistic assumptions, motivated directly by the device characterization and by established properties of graphene. We find that –in agreement with these assumptions– a scenario based on a two-step distribution function reproduces our observations (namely the functional dependence of $I_c(V_{cnt})/I_c(V_{cnt} = 0)$) satisfactorily, whereas the use of a thermal distribution with an effective temperature T^* does not. The consequence of this finding is that our results provide spectroscopic information about the contribution to the supercurrent given by states at different energy. In particular, our findings imply that when $V_{cnt} > 2\Delta/e$, the contribution given by subgap states to the supercurrent is essentially entirely suppressed, and that the remaining supercurrent that flows for $V_{cnt} > 2\Delta/e$ is due to states at energy $E > \Delta$, i.e. the Andreev resonances first discussed by Kulik[1]. We find that these JJs Andreev resonances at $E > \Delta$ contribute for approximately 20% to the critical current measured in equlibrium, corresponding to a non-negligible fraction of the total. These results further confirm how the use of graphene in place of conventional diffusive metals provide new opportunities to investigate aspects of superconducting proximity effect that have remained unexplored until now [6, 29, 30].

5.5 Appendix

Transparency of the superconductor/graphene contacts

Similarly to what we have shown in an early publication [30], we can estimate quantitatively the transparency of the graphene/superconductor interface in our devices, by looking either at the sub-gap structure originating from multiple Andreev refection in the differential resistance versus applied bias, or at the excess current. The data for the device discussed in the main text, measured at $V_G = -60$ V and 250 mK are shown on Fig. 5.6. The simplest

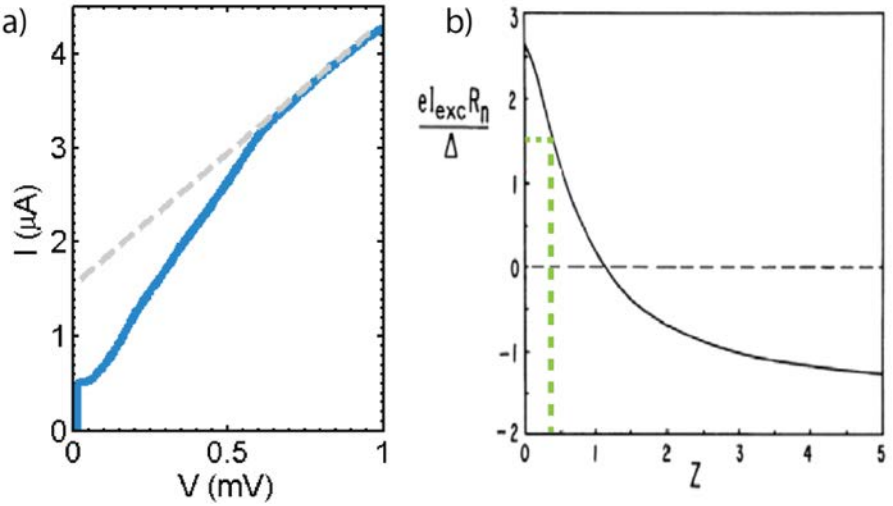

Figure 5.6: a) $I - V$ characteristic of the device measured at $T = 250mK$ and $V_G = -60V$. The dashed line extrapolates the linear behavior observed at large applied bias down to $V = 0$ V, to extract the excess current. b) Theoretical plot of the excess current of a SNS junction according to the OTBK model (figure adapted from [31]), from which we extract the value of the parameter Z, as indicated by the green dashed lines. We find $Z \simeq 0.4$ and $T_{int} = 1/(1 + Z^2) \simeq 0.86$. This value is typical, as it is comparable to the one that we found on similar graphene Josephson junctions realized in the past.

way to extract a quantitative estimate is by comparing the measured excess current to the calculations of the same quantity based on the so-called OTBK model [31] (see Fig. 5.6 b), and details in the figure captions). We find that the interface transmission is $T_{int} = 1/(1 + Z^2) \simeq 0.86$, with a scattering parameter $Z \simeq 0.4$.

Gate-voltage dependence of the control line resistance

As a further characterization of our devices, and to extract the diffusion constant D of electrons in graphene, we show the gate voltage dependence of the square resistance of graphene extracted from the measured resistance of the control line (see Fig. 5.7; measurement performed at $T = 250$ mK).

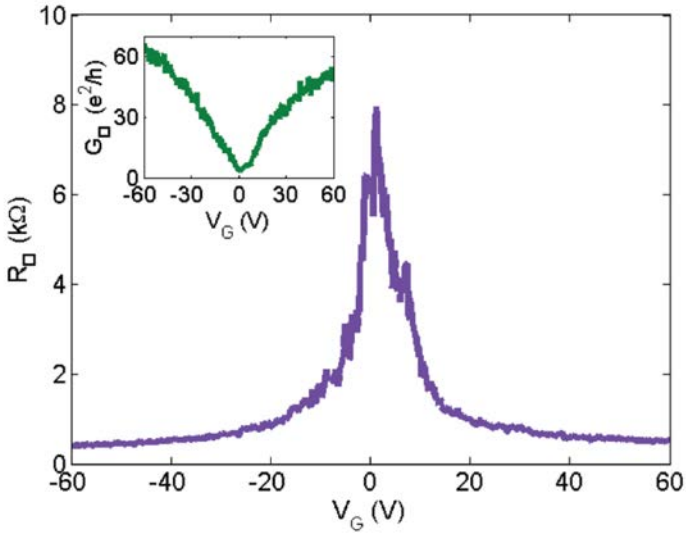

Figure 5.7: Gate voltage dependence of the square resistance of the control line measured at $250mK$. Inset: Gate voltage dependence of the square conductance of the control line.

From the gate dependence of the conductance per square $G_\square$ (shown in the inset of Fig. 5.7), we determine the charge carrier, using the charge carrier concentration obtained from $n = \epsilon_0\epsilon_r(V_G - V_D)/de$ ($V_D = 4$ V is the position of the charge neutrality point, i.e., the value of V_G where the measured resistance is maximum). We find that at high carrier densities $\mu \approx 3500$ cm$^2/Vs$. To estimate the diffusion constant D we use Einstein equation $\sigma = \nu e^2 D$ where σ is the measured conductivity and $\nu = 8\pi \mid \epsilon_F \mid /(hv_F)^2$ density of states for graphene at the Fermi level ϵ_F . In the gate voltage range where the experiments described in the main text are done we obtain $D \approx 420cm^2/s$. We estimate $L_\phi = \sqrt{D\tau_\phi}$ using the value of D just obtained and the phase coherence time τ_ϕ obtained from literature studies of weak localization. From many different papers, we find that at 250 mK and in the same carrier density range of our experiments, $\tau_\phi \sim 100$ ps or longer [21, 22, 23], which gives $L_\phi \sim 2\mu$ m or longer. We conclude that L_ϕ exceeds the length of the control

line, as it is needed to induce a two-step non-equilibrium distribution function in our superconducting junction.

Different criteria to determine the critical current

In practice, the critical current of a Josephson junction is defined as the current for which the voltage across the junction exceeds a fixed (arbitrary) threshold. In the main text we have used $1nV$ as threshold. Here, to show that our conclusion do not depend on the specific value chosen for the threshold, we show the curve $I_c(V_{cnt})/I_c(V_{cnt}=0)$ for a different value of the threshold ($2nV$; see Fig. 5.8). All the considerations made discussing Fig. 5.5 of the main text can be made equally well for the data shown in Fig. 5.8, which shows that our conclusions do not depend on the specific value chosen for the threshold voltage.

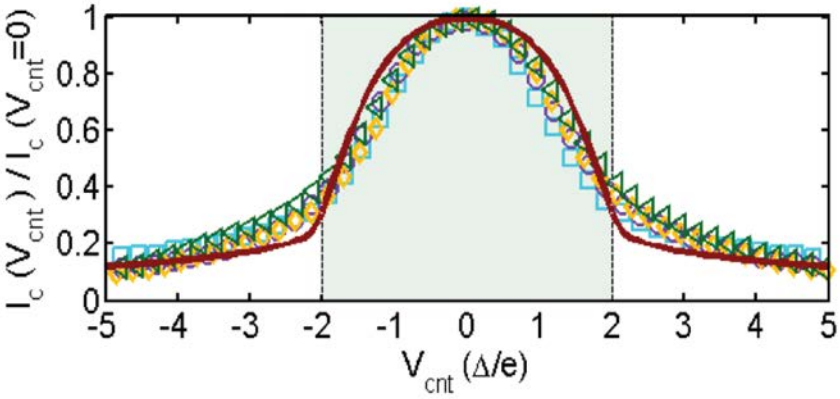

Figure 5.8: Normalized critical current at $T = 250$ mK obtained using a 2 nV threshold criterion. Different symbols representing measurements at different gate voltages: $V_G = -60$ V (triangles), -50 V (diamonds), -40 V (circles), -30 V (squares). The red line represents the result obtained with the same theoretical model referred to in the main text.

5.6 Bibliography

[1] I. O. Kulik. Macroscopic quantization and the proximity effect in s-n-s junctions. *Sov. Phys. JETP*, 30:944, 1970.

[2] John Bardeen and Jared L. Johnson. Josephson current flow in pure superconducting-normal-superconducting junctions. *Phys. Rev. B*, 5:72, 1972.

[3] A. Martín-Rodero and A. Levy Yeyati. Josephson and Andreev transport through quantum dots. *Adv. Phys.*, 60(6):899–958, 2011.

[4] A. F. Andreev. *Sov. Phys. JETP*, 19:1228, 1964.

[5] Pillet, C. H. L. Quay, P. Morfin, C. Bena, A. Levy Yeyati, and P. Joyez. Andreev bound states in supercurrent-carrying carbon nanotubes revealed. *Nat. Phys.*, 6:965–969, 2010.

[6] Travis Dirks, Taylor L. Hughes, Siddhartha Lal, Bruno Uchoa, Yung-Fu Chen, Cesar Chialvo, Paul M. Goldbart, and Nadya Mason. Transport through Andreev bound states in a graphene quantum dot. *Nat. Phys.*, 7(5):386–390, May 2011.

[7] L. Bretheau, C. O. Girit, H. Pothier, D. Esteve, and C. Urbina. Exciting Andreev pairs in a superconducting atomic contact. *Nature*, 499(7458):312–315, July 2013.

[8] J. Schindele, A. Baumgartner, R. Maurand, M. Weiss, and C. Schönenberger. Nonlocal spectroscopy of Andreev bound states. *Phys. Rev. B*, 89:045422, Jan 2014.

[9] A.F. Morpurgo, J.J.A. Baselmans, B.J. van Wees, and T.M. Klapwijk. Energy spectroscopy of Josephson supercurrent. *J. Low Temp. Phys.*, 118(5-6):637–651, 2000.

[10] B. J. van Wees, K.-M. H. Lenssen, and C. J. P. M. Harmans. Transmission formalism for supercurrent flow in multiprobe superconductor-semiconductor-superconductor devices. *Phys. Rev. B*, 44:470–473, Jul 1991.

[11] P. Samuelsson, J. Lantz, V. S. Shumeiko, and G. Wendin. Nonequilibrium Josephson effect in mesoscopic ballistic multiterminal sns junctions. *Phys. Rev. B*, 62:1319–1337, Jul 2000.

[12] A. F. Morpurgo, T. M. Klapwijk, and B. J. van Wees. Hot electron tunable supercurrent. *Appl. Phys. Lett.*, 72(8):966–968, 1998.

[13] Philip F. Bagwell. Suppression of the Josephson current through a narrow, mesoscopic, semiconductor channel by a single impurity. *Phys. Rev. B*, 46:12573–12586, Nov 1992.

[14] F. K. Wilhelm, Gerd Schön, and Andrei D. Zaikin. Mesoscopic superconducting-normal metal-superconducting transistor. *Phys. Rev. Lett.*, 81:1682, 1998.

[15] S.-K. Yip. Energy-resolved supercurrent between two superconductors. *Phys. Rev. B*, 58:5803–5807, Sep 1998.

[16] H. Pothier, S. Guéron, Norman O. Birge, D. Esteve, and M. H. Devoret. Energy distribution function of quasiparticles in mesoscopic wires. *Phys. Rev. Lett.*, 79:3490–3493, Nov 1997.

[17] F. Pierre, H. Pothier, D. Esteve, and M.H. Devoret. Energy redistribution between quasiparticles in mesoscopic silver wires. *J. Low Temp. Phys.*, 118(5-6):437–445, 2000.

[18] F. Pierre, A. B. Gougam, A. Anthore, H. Pothier, D. Esteve, and Norman O. Birge. Dephasing of electrons in mesoscopic metal wires. *Phys. Rev. B*, 68:085413, Aug 2003.

[19] J. J. A. Baselmans, A. F. Morpurgo, B. J. van Wees, and T. M. Klapwijk. Reversing the direction of the supercurrent in a controllable Josephson junction. *Nature*, 397(6714):43–45, January 1999.

[20] Michael Tinkham. *Introduction to superconductivity*, volume 1. Courier Dover Publications, 2004.

[21] Dong-Keun Ki, Dongchan Jeong, Jae-Hyun Choi, Hu-Jong Lee, and Kee-Su Park. Inelastic scattering in a monolayer graphene sheet: A weak-localization study. *Phys. Rev. B*, 78:125409, Sep 2008.

[22] M. B. Lundeberg, R. Yang, J. Renard, and J. A. Folk. Defect-mediated spin relaxation and dephasing in graphene. *Phys. Rev. Lett.*, 110:156601, Apr 2013.

[23] Nuno J.G. Couto, Davide Costanzo, Stephan Engels, Dong-Keun Ki, Kenji Watanabe, Takashi Taniguchi, Christoph Stampfer, Francisco Guinea, and Alberto F. Morpurgo. Random strain fluctuations as dominant disorder source for high-quality on-substrate graphene devices. *Phys. Rev. X*, 4:041019, Oct 2014.

[24] Hubert B. Heersche, Pablo Jarillo-Herrero, Jeroen B. Oostinga, Lieven M. K. Vandersypen, and Alberto F. Morpurgo. Bipolar supercurrent in graphene. *Nature*, 446(7131):56–59, March 2007.

[25] FrankK. Wilhelm, AndreiD. Zaikin, and Gerd Schön. Supercurrent in a mesoscopic proximity wire. *J. Low Temp. Phys.*, 106(3-4):305–310, 1997.

[26] Xu Du, Ivan Skachko, and Eva Y. Andrei. Josephson current and multiple Andreev reflections in graphene sns junctions. *Phys. Rev. B*, 77:184507, May 2008.

[27] M. Titov and C. W. J. Beenakker. Josephson effect in ballistic graphene. *Phys. Rev. B*, 74:041401, Jul 2006.

[28] F. Giazotto, T.T. Heikkilä, F. Taddei, R. Fazio, J.P. Pekola, and F. Beltram. Mesoscopic supercurrent transistor controlled by nonequilibrium cooling. *J. Low Temp. Phys.*, 136(5-6):435–452, 2004.

[29] Adrien Allain, Zheng Han, and Vincent Bouchiat. Electrical control of the superconducting-to-insulating transition in graphene-metal hybrids. *Nat. Mater.*, 11(7):590–594, July 2012.

[30] Fabio Deon, Sandra Šopić, and Alberto F. Morpurgo. Tuning the influence of microscopic decoherence on the superconducting proximity effect in a graphene Andreev interferometer. *Phys. Rev. Lett.*, 112:126803, Mar 2014.

[31] G. E. Blonder, M. Tinkham, and T. M. Klapwijk. Transition from metallic to tunneling regimes in superconducting microconstrictions: Excess current, charge imbalance, and supercurrent conversion. *Phys. Rev. B*, 25:4515–4532, 1982.

Acknowledgements

Looking back, doing PhD in quantum electronics was enriching and challenging experience for me, both professionally and personally. Professionally, as I worked on something that demanded considerable commitment in order to make results happen, and was at the same time interesting due to many different aspects of work that needed to be mastered. Personally, as I feel fortunate to have built life-long friendships with people I met in Geneva and that I have extended my circle of peers who significantly impacted the way I perceive the world. It is my pleasure to take this opportunity to thank all the people who contributed to my work and my friends and family who were there for me to provide incredible support throughout these years.

First, I would like to thank Alberto F. Morpurgo for offering me a position in his group where I had a chance to work in a very stimulating environment and to learn from great researchers who gave me continuous feedback and challenged me to progress towards my goals. Your dedication to work, scientific knowledge, and critical approach to your work and work of your students are indeed remarkable. Within these more than five years I have witnessed how the research dynamics and activities within the group changed and were brought to an impressive level under your lead. My gratitude also goes to Sergey Kubatkin (Chalmers) and Christoph Renner (Geneva) for finding time to read my thesis, their constructive comments and being part of my thesis committee. Here, I would also like to thank Christophe Berthod for giving clear and interesting lectures on the many-body physics, his help regarding my exam on superconductivity, and for translating the abstract of my thesis to French.

Without any doubt, what made my PhD days enjoyable and fun is working with inspiring and smart people with whom I became more than just colleagues. Fabio, we worked closely together for not such a long time, anyhow, you are the person from whom I learned the most. Thank you for sharing your scientific knowledge and lab experience on induced superconductivity with me which helped me to push my projects forward. I am glad I had a chance to meet you and to enjoy your neat sense of humor, especially dur-

ing those long and tiring measurement days. Anya, some of the best laughs happened with you. Thank you for organizing the fabulous trip to Puglia, your friendly care, insightful comments and opinions, and for all other great things you did for me (not talking only about the hot quantum matter calendar). Ki, with your all-mighty-powerful-postdoc arrival, the group gained a lot and so did I. Thank you for your patience and help in all those moments starting with "Ki, can I bother you again?". Jeroen, though we overlapped in Geneva shortly, I am glad to have met you and that I had a pleasure of having your guidance around the lab. Thanks for that touching thumbs-up email you sent to me before the big day. Marta, I admire your endless enthusiasm, your ability to always lighten the mood and to see the positive side in no matter what situation. I am happy for having you as a friend (seriously, you should befriend yourself!). Thanks for finding time in your busy schedule to be there for me, for supporting me in your unique and creative ways and for being one of my role models whose opinion I trust and value. Anci (zenska), hvala na tvom veselom stavu, iskrenim savetima i "gotivnim" uspomenama. Nacho (papasito lindo y ermoso), you said "Don't worry Sandrita, the most handsome one is not going to leave", and, I am very glad that it did turn out to be the truth as your presence did bring a lot of fun. Sanghyun, thanks for your scientific help and, though you are careful and reserved, sharing your experiences and views with me which were indeed eye-opening. Alex, the group benefits a lot from having you as a technician. Thanks for always being willing to help in the lab, staying calm even when I made a big big mess, and beyond of being pleasent while doing your work, thanks for being respectful colleaugue and a great friend. Nuno, remeber how it would immediately get hot when you would enter the office? How fortunate I was to be your desk neighbor so I could appreciate the heat your presence brought and enjoyed your jokes! Young Woo, it was a pleasure to share the office with you and enjoy your nice company. Evgeniy, Diego, and Aditya, I am happy to have met you, and I wish you all very successful PhDs. Zhe and Lin, with so many compliments from your side (very grateful), delicious food you made and the excellent selection of Chinese restaurants you brought us to, I can't wait to visit China. Renan, it was great having somebody as interesting and easygoing around, who would always be in for action and fun! Anna-Maria, thanks for all the friendly talks we exchanged, many of ours girls nights out, and all the other beautiful time we spent together.

Especially, I would like to thank people who made my time in Geneva wonderful and memorable, and whose presence helped me to surpass many personal and professional heights. Lucie, you are one of the members of my Geneva family, and I am very happy that we were housemates where I had a chance to met you. Love all our trips Madrid, Singapore, Zermatt, Amsterdam, skiing in France, food trips. It has been quite enriching -more than

just having somebody to cook delicious meals- and great friendship that we built during our PhD days. Rinad, meeting you when I just came to Geneva was a pure gift. Having somebody as amazing as you are made my moving to Geneva much more welcoming, particularly in those moments when I needed a break from a judgmental surrounding. Stephanie, I'm honored to be somebody you have chosen for a friend. Your love and care are so genuine that even in hard times when I was trying to fake feeling good you could just see through me, and be a support that I could only wish for. More than having somebody to rely on, you were a great company for swimming on the lakeside -or just putting the feet in the water, in-line skating, dancing, girls shopping and, the list could go on and on as you became a big part of my life. Elisabeth, bien que je ne reçois pas une chance de te voir aussi souvent depuis que tu as démenagé à Grenoble, à chaque fois que nous rencontrons le sentiment d'être très proche ami avec toi me rend vraiment heureuse. Je te remercie pour de touts girlish beers que nous avions au bord de la rivière pendant les heures de travail et, ainsi pour le temps que tu a trouvé toujours pour nous, malgré que te es locale et entourée de tes amis de Genève. Zoki, presrećna sam što si došao u Ženevu i sto sam, iako nekada na silu ("Jesi normalna, vidi koliko je sati?!"), imala prilike da uživam u tvom sjajnom smislu za humor i presmešnim interpretacijama bogatog umetnickog opusa žene-zmije. Hvala na mnogobrojnim momentima kad si mi smehom do suza ulepšao dan! Diki (dušo), trenutak "niko da me zagrli vec mesecima" je bio preokret i za mene. Mnogo mi je drago što nas je ovo vreme zbližilo i što delimo puno divnih uspomena iz Švajcarske. Davide (Guapo), the bonds we created with each other feel like some of my most valuable long-lasting friendships (my social spas). Thank you for the happiness your friendship gives, mingling together with complete strangers, appreciating my choice of movies (minus transgender&similar stories), for parties and other fantastic time we had together. Flavia, thank you for your attentive care and insights which made me question what I want. Charles and Woei Ling, knowing that you don't surround yourself with many friends, and still being close to someone as special as you two is flattering. Thank you for being part of my Geneva family.

Na kraju, želim da se zahvalim svojim najbližima koji su bili moja najveća podrška svih ovih godina. Baki, obožavam tvoju pronicljivost i tvoje ne-tako-očigledne načine da učiniš i nemoguće za ljude koje voliš i o kojima brineš. Pravo je bogastvo što imam tebe za primer u životu! Suki, divim se tvojoj veseloj pripodi koja mi je toliko puta razveselila dana. Ogromna je sreća što znam da uvek mogu da računam na tebe. Mama, iako je moj odlazak tebi najteže pao, uvek si dala sve od sebe da se to ne vidi i ne odrazi na mene i moje životne odluke. Hvala na beskrajnom razumevanju "tvoje" ćerke (nažalost, i njenih neprimerenih reakcija), nesebicnoj podršci i neizmernoj ljubavi. Gordane (Srce), bezobzira na našu razdvojenost i (pre)zauzetost svih ovih god-

ina, uvek si bio moja najveća podrška i oslonac, pogotovo u periodima usamljenosti, punih unutrašnjih i ličnih preispitivanja; osoba sa kojom najpre podelim i dobro i loše, i koja me uvek podseti ko sam i čemu treba da stremim. Divim se tvom pozitivnom stavu i energiji, tvojoj ambiciji i posvećenosti poslu (pre desetak godina mom neprijatelju br.1.), i tvojoj nesalomivoj veri u mene i u nas (jedna od retkih konstanti u našem odnosu). Hvala na mnogobrojnim dolascima u Ženevu i prelepim uspomenama koje smo napravili kojekuda po svetu.